Piezo- and Ferroelectric $A^{+}B^{5+}O_3$ Thin Films

Series of dissertations submitted to the
Faculty of Mathematics and Natural Sciences, University of Oslo
No. 1838

ISSN 1501-7710

Cover: Hanne Baadsgaard Utigard.
Print production: Reprosentralen, University of Oslo.

Thanks and Dedication

This thesis is submitted in partial fulfilment of the requirements for the degree of *Philosophiae Doctor* at the Department of Chemistry, Faculty of Mathematics and Natural Sciences, University of Oslo. The experimental work was carried out at the group for Nanostructures and Functional Materials (NAFUMA) under the supervision of Professor Helmer Fjellvåg and Professor Ola Nilsen between August 2012 and December 2016. I sincerely thank my supervisors for the possibility to work in their group, and for essential support along the way.

I would like to thank all the members of the NAFUMA-group for fruitful discussion and rewarding collaboration over the course of my work here. I would also like to thank my co-authors, Erik Østreng, Michael Norderhaug Getz, Sigurd Øien-Ødegaard, Dmitry Chernyshov and Timo Sajavaara for invaluable collaboration and discussion.

A most sincere gratitude is directed towards my good friend and office-mate Jon Einar Bratvold for fantastic years of science, quiz, music, chess and general procrastination. Office life will never be the same.

I would also like to specifically thank the other prominent members of our science and procrastination team; Amund Ruud, Øystein Slagtern Fjellvåg, Kristian Weibye, Magnus Mortén, Ingvild Wiik and Ina Grosås Eikjeland for the great years we have spent together.

Gratitude is directed towards all my teachers throughout the years, giving me space to dive into the natural sciences at my own pace. In this regards, I would specifically like to thank Vigdis Rødset, Nina Sveen, Reidun Torp, Trygve Roaas and Oddvar Stubø.

I would like to thank my mother and father for endless love and support, and for giving me the chance to become who I am. A special thanks to Svein Bråten for taking me to Vemork Power Station a summer in the early 2000's; this really triggered my interest in the natural sciences. I would also like to thank all my other friends and family-members.

Finally, the most important thank-you is directed to my teenage sweetheart (now wife) and love-of-my-life, Marit, for love and understanding through 12 years. Living with a scientist is not always a bed of roses.

This thesis is dedicated to my children; Hedda, and the little one we are expecting come summer 2017.

You have made me recognize what is really important in life.

Abstract

This thesis summarizes atomic layer deposition (ALD) of thin films of a set of alkali metal niobates and tantalates with technologically important physical properties.

ALD of $LiNbO_3$ is presented first, where we showcase the possibility of epitaxial integration of complex oxide thin films containing alkali metals. $LiNbO_3$ is a high performance ferroelectric, and these properties are studied to show that ALD can be utilized to obtain highly oriented films with piezo- and ferroelectric activity.

The thesis continues with investigating the feasibility of growing sodium- and potassium containing materials with ALD. Prior to the work leading to this thesis, no reports of Na/K-deposition by ALD have been available. Several precursors are screened for self-limiting growth under typical ALD-conditions, and two optimal precursors are used to carry out deposition of sodium- and potassium aluminate. These precursors, both alkali metal *t*-butoxides, offer the possibility to grow sodium- and potassium containing materials, with water as the co-reactant, at temperatures between 250 and 300 °C.

Using the results from general deposition of Na/K-containing materials and the experience from $LiNbO_3$-deposition, four alkali metal niobates and tantalates; $NaNbO_3$, $NaTaO_3$, $KNbO_3$ and $KTaO_3$, were deposited. These materials have interesting intrinsic properties, such as ferroelectricity ($KNbO_3$) and photocatalytic activity ($NaNbO_3$). More technologically interesting, however, are the solid solutions $K_xNa_{1-x}NbO_3$ and $KTa_xNb_{1-x}O_3$, which are desirable for their strong ferroelectric and electrooptical responses, respectively.

Proof-of-concept on the intermixing of these solid solutions by ALD is presented, displaying remarkable compositional control and reproducibility. $K_xNa_{1-x}NbO_3$ thin films are deposited for investigation of its electric properties, and piezoelectric activity is studied using piezoelectric force microscopy. The films are epitaxially integrated on a range of substrates, thereby controlling the orientation and direction of the polarity.

Finally, some general notes on atomic layer deposition of alkali metal containing complex oxides are made, in light of what has been achieved in this work.

Three main papers form the basis for this thesis. One on deposition of $LiNbO_3$, a second on Na/K-deposition and a third on alkali metal niobate/tantalate-deposition.

Table of Contents

Glossary

AFM	atomic force microscopy
ALD	atomic layer deposition
BFO	bismuth ferrite ($BiFeO_3$)
CVD	chemical vapour deposition
FT-IR	Fourier transform infrared spectroscopy
GIXRD	gracing incidence x-ray diffraction
GPC	growth per cycle
HMDS	hexamethyl disilazane ($[(CH_3)_3Si]_2NH$)
KNN	sodium potassium niobate ($K_xNa_{1-x}NbO_3$)
KNO	potassium niobate ($KNbO_3$)
KTN	potassium tantalate niobate ($KNb_{1-x}Ta_xO_3$)
KTO	potassium tantalite ($KTaO_3$)
LAO	lanthanum aluminate ($LaAlO_3$)
LNO	lithium niobate ($LiNbO_3$)
MBE	molecular beam epitaxy
NNO	sodium niobate ($NaNbO_3$)
NTO	sodium tantalite ($NaTaO_3$)
PFM	piezoelectric force microscopy
PLD	pulsed laser deposition
PZT	lead zirconate titanate ($PbZr_{1-x}Ti_zO_3$)
SAW	surface acoustic wave
STO	strontium titanate ($SrTiO_3$)
TEM	transmission electron microscopy
TGA	thermogravimetric analysis
thd	2,2,6,6-tetramethyl-3,5-heptanedionato ($[(CH_3)_3CO]_2CH_2$)
TMA	trimethyl aluminium ($Al(CH)_3$)
TMSO	trimethyl silanolate ($Si(CH)_3O$)
TOF-ERDA	time-of-flight elastic recoil detection analysis
XPS	x-ray photoelectron spectroscopy
XRD	x-ray diffraction
XRF	x-ray fluorescence

List of Papers

Paper 1:

Atomic Layer Deposition of ferroelectric $LiNbO_3$

Østreng, E., Sønsteby, H.H., Sajavaara, T., Nilsen, O., Fjellvåg, H., Journal of Materials Chemistry C **1 (27)**, 4283-4290, **2013**

Paper 2:

Atomic Layer Deposition of Sodium- and Potassium Oxides: Evaluation of Precursors and Deposition of Thin Films

Østreng, E., Sønsteby, H. H., Øien, S., Nilsen, O., Fjellvåg, H., Dalton Transactions **43**, 16666-72, **2014**

Paper 3:

Atomic Layer Deposition of $(K,Na)(Nb,Ta)O_3$ Thin Films

Sønsteby, H. H., Fjellvåg, H., Nilsen O., Journal of Vacuum Science and Technology, **34(4)**, 041508, **2016**

I have also authored the following papers that contain additional information on ALD of functional oxides and measurement techniques. These papers are not directly relevant to the thesis subject, and are thus not included in the thesis.

Functional Perovskites by Atomic Layer Deposition – an Overview

Sønsteby, H.H., Fjellvåg, H., Nilsen, O., Advanced Materials Interfaces, **2016**, DOI: 10.1002/admi.201600903

Deposition and X-ray Characterization of Epitaxial Thin Films of $LaAlO_3$

Sønsteby, H., Østreng, E., Nilsen, O., Fjellvåg, H., Thin Solid Films **550**, 90-94, **2014**

On the Application of a Single-crystal κ-diffractometer and a CCD Area Detector for Studies of Thin Films

Sønsteby, H., Chernyshov, D., Getz, M., Nilsen, O., Fjellvåg, H., Journal of Synchrotron Radiation, **20**, 644, **2013**

1. Introduction

Carrying out the work that led to this thesis, I have come to recognize how nearly everything we do in day-to-day life is connected to progress in materials science. Contemplate, for example, on the fantastic technological advances that have made it possible for me to pick up my phone to check my e-mail. Billions of bits of information are sent and received in a complex array of microelectronics, allowing me to stay up to date on the events of the world by a simple touch on a screen.

Or, what about the pages on which this thesis is written? A collection of a million ink dots per page accurately placed on a sheet of paper by tiny nozzles that are moved around by incredibly accurate stepper motors. It's easy to forget the brilliance of an ink jet printer when you buy one for $50 at the local electronics dealer.

At the university, I use instrumentation like the atomic force microscope, which has been an important part of this work. This lets me study nanometre size features on a sample surface, all made possible by piezoelectric actuators and oscillators that are precise down to fractions of a micrometre.

Microelectronics has become an integral part of everyday life and modern science alike. The nearly infinitely accelerating progress in materials technology is hard to fathom, and has given us means of communication, transport and energy harnessing that were unimaginable just ten years ago.

This progression does not come without cost. We are all aware of the growing environmental concerns, both on local and global scale. In the world of electronics, for example, local pollution by disposal of devices containing high amounts of toxic heavy metals is a challenge. One of the key perpetrators is the element *lead*, found in almost all electronic devices. The society is very aware of and knowledgeable about lead pollution, but slow progress in finding replacement materials has caused billions of devices containing hazardous amounts of lead to be produced; and they are still in production. There are different uses of lead in modern electronic devices, and one of the most common culprits is in the form of *lead zirconate titanate (PZT).* This is *a perovskite piezo- and ferroelectric* material with outstanding performance that is found in transducers, capacitors and actuators.

The functionality of PZT is perfect. High Curie temperature, very high dielectric constant, extreme tunability and straightforward preparation renders it ideal for industrial use. Containing more than 60 wt% lead, however, it is a true environmental monster. Millions of tons of electronic waste around the globe see lead leaking to the surroundings, and getting rid of it when the damage is done is far from easy.

The only logical conclusion to be drawn from this is that lead containing materials must be outright removed from electronic devices. This, however, is not done in an instant. Society is not interested in letting go of comforts it has become used to. Simply removing dangerous materials will not be accepted by the public if replacements with the same or better function do not already exist. In other words, we are in high need of replacement materials that are cheap and easy to process, with just as good performance as its lead counterparts.

Obtaining these materials is not a farfetched goal, and viable candidates already exist. Alkali metal niobates are one group of materials that is proposed to challenge the PZT-hegemony. It is specifically two compounds; *lithium niobate* ($LiNbO_3$) and *potassium sodium niobate* ($K_xNa_{1-x}NbO_3$) that have electric properties in the same order of magnitude as PZT, and are believed to be true contenders.

For many of the presented applications, it is crucial that the material can be made as a *thin film*. These are nanometre thick, pinhole free and conformal layers with controlled domain morphology and crystal structures. Producing alkali metal containing thin films has proven to be quite challenging, and this is one of the reasons as to why these materials are not already in widespread use.

This thesis is a part of materials science rising to the challenge. Thin films of $LiNbO_3$ and $K_xNa_{1-x}NbO_3$ are here grown by the *atomic layer deposition* (ALD) technique, yielding high performance ferroelectric materials with high conformality and thickness control. A viable route to replacing lead in electronic devices is the ultimate impact of this work.

On the way to this result, several lesser obstacles and challenges have been overcome. This often carries with it some positive side-effects, with impact on a more scientific level. A relevant example is the lack of any reported ALD-processes involving sodium or potassium before this work was initialized. Building on knowledge from lithium processes a pathway was found, and by now, several other research groups around the world are using these results to make other alkali metal containing thin films. In other words, the work has impact on *the thin film community* by enabling deposition of two elements that was previously not possible.

Some sidesteps on the way have also produced results, among them deposition of other materials in the same class. Examples are *sodium tantalate* ($NaTaO_3$) and *sodium niobate* ($NaNbO_3$), which are investigated as high efficiency photocatalysts, and potassium tantalate niobate ($KTa_xNb_{1-x}O_3$), which has brilliant electrooptical properties. In addition to this, ALD can be used to create multilayer heterostructures with new exotic effects that is believed to revolutionize materials science.

This work is a small step towards a more environmentally friendly world, a step towards better understanding of alkali metal containing thin films in general, and a big step in the world of complex oxide deposition by ALD.

2. $A^{+}B^{5+}O_3$ Perovskite and Perovskite-like Materials

Perovskite is originally the name of a specific mineral, *calcium titanate*, discovered in 1839 in the Ural mountain range and named after the Russian mineralogist Lev Perovski in 1839. The crystallographic structure was described for a similar mineral, *barium titanate*, in 1945, revealing how the barium cation is 12-fold- and titanium is 6-fold coordinated to the oxygen anions.[1] A large group of minerals with ABX_3 composition, where A is a large cation, B is a small cation and X is a small anion, has subsequently been found to adopt the same structure. Because of these structural similarities, the word *perovskite* is now most commonly used to describe the whole range of materials with identical or similar structures, including the new organic- inorganic hybrid materials that have come to challenge the silicon solar cell hegemony.

Perovskites and perovskite-like structures have been widely studied over the years, as the versatility of the structure permits a wide range of electric and magnetic effects. Examples are multiferroic bismuth ferrite (antiferromagnetic and ferroelectric at room temperature) and colossal magnetoresistance in lanthanum strontium manganite.[2-5] High structural tolerance for substitution on the A- and B-sites also allows for engineering of these effects. As an example; STO is an *incipient ferroelectric*, a material where the ferroelectric phase transition is suppressed by some effect (in this case ionic quantum fluctuations).[6] Gradual doping of bismuth on the A-site induces three separate electric modes, turning the structure first into a relaxor dielectric, then a mixed relaxor dielectric and ferroelectric, before finally reaching a pure relaxor ferroelectric state.[7] In addition, interfaces *between* different perovskites may exhibit exotic effects on their own, such as the superconducting 2D-electron gas created at the LAO||STO-interface.[8, 9] The possibilities of intelligent functional design are close to limitless.

The ideal cubic perovskite structure exists in minerals such as STO and calcium rubidium fluoride ($CaRbF_3$), but is relatively uncommon. The perovskite group of structures typically also include slightly distorted versions of the structure, lowering the symmetry and altering the coordination of the cations. The distortion can be triggered by size effects, stoichiometric variations or electronic effects such as the *Jahn-Teller* effect.[10, 11] An indication on the possibility for an ABO_3-compound to form a perovskite structure can be found by assuming pure ionic bonding and looking at the size of the cations. To form a perfect cubic cell with a 12-fold coordinated A-site, also assuming identical ionic radii of A and X, it can be shown that the length of an X-A-X line ($2R_X + 2R_A$) must equal $\sqrt{2}(2R_X + 2R_B)$, which corresponds to the cubic cell edge. Using this, we can introduce the *Goldschmidt tolerance factor*:

$$t = \frac{(R_X + R_A)}{\sqrt{2}(R_X + R_B)} \qquad \textbf{Eq. 1}$$

where R_X, R_A and R_B are the ionic radii of X, A and B respectively.[12] The typical cubic perovskites have tolerance factors close to unity, whereas high or low tolerance factors indicate that the structure tends to be distorted. As an example; $SrTiO_3$ have a tolerance factor of 1.002 and adopts a perfect cubic perovskite structure (space group *Pm-3m*).[13]

The classification of perovskite structures is not in the scope of this thesis, but the tolerance factor can be used as a tool to understand the structures that are important in this work. Simple alkali and group V perovskites are the main focus, with limitations to lithium, sodium and potassium on the A-site and niobium and tantalum on the B-site. Figure 1 summarizes the tolerance factors of the six relevant structures at room temperature. Note that no compounds with 12-coordinated Li^+ have been reported. The lithium ionic radius used for calculation on $LiNbO_3$ and $LiTaO_3$ is estimated by using trends in ionic radii for different sodium- and potassium coordination (Figure 1, right).

Compound	Tolerance factor	Structure type
$LiNbO_3$	*0.83 – 0.89*	*Rhombohedral (R3c, SG# 161)*
$LiTaO_3$	*0.83 – 0.89*	*Rhombohedral (R3c, SG# 161)*
$NaNbO_3$	0.97	Orthorombic (Pbcm, SG# 57)
$NaTaO_3$	0.97	Orthorombic (Pnma, SG# 62)
$KNbO_3$	1.06	Monoclinic (C2/m, SG# 12)
$KTaO_3$	1.06	Cubic (Pm-3m, SG# 221)

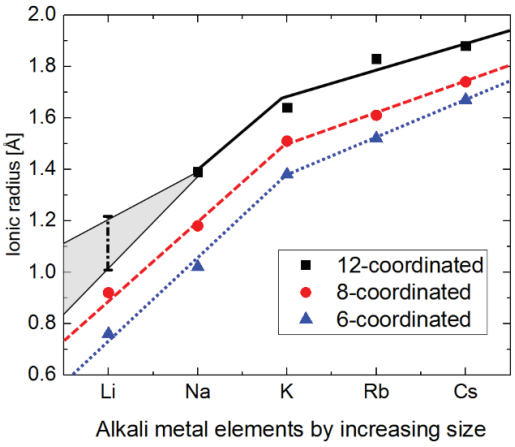

Figure 1, left: Table summarizing the tolerance factor and structure types for the alkali metal niobates and tantalates. Right: Estimating the size of a theoretical 12-coordinated lithium cation.

The small size of the lithium ion does not favour the formation of a perovskite-like structure, but rather formation of an ilmenite related structure. The sodium counterparts both take orthorombically distorted perovskite structures, whereas the potassium versions are cubic and monoclinic. The monoclinic

potassium niobate is in reality very close to a tetragonal structure, which is what was reported in literature when the phase transitions were first described.[14]

Understanding the basis of these structures is important to relate structure to functional properties, and a more detailed venture into the world of these structures follows below.

Functional Properties of $A^{+}B^{5+}O_3$ Compounds

A major goal in this work has been to investigate and tailor functionality in the six $A^{+}B^{5+}O_3$ compounds of interest. Functionality in this sense is typically represented by magnetic or electric response of some kind, originating from breaking *time-reversal* or *inversion* symmetry respectively. Materials can exhibit spontaneous magnetization or polarization (*ferro*-behaviour), or temporarily respond to an external permutation such as a magnetic- or electric field. In this thesis, it is the spontaneous or permanent (but switchable) behaviour that is of highest interest.

Ferromagnetism is collective spontaneous alignment of spins that adds up to a net magnetization. It is found in a handful of d- and f-metals, and in some oxides and alloys. Ferromagnetic complex oxides, however, are rare. This is due to the *super-exchange* phenomena that results in anti-parallel ordering of spins, rendering the materials *anti*-ferromagnetic (Figure 2).[15-17] Exceptions exist. Net magnetization can either arise through mixed-valence states, such as in (Ca,La)MnO_3 or through compounds with itinerant metallic magnetic character, such as $SrRuO_3$.[18, 19] These phenomena are discussed in detail in a recent review paper discussing functional perovskites deposited by ALD.[20] In the $A^{+}B^{5+}O_3$ compounds specifically, magnetic interactions are not feasible, as neither the A- or B-site ion have partially filled *d*- or *f*-orbitals.

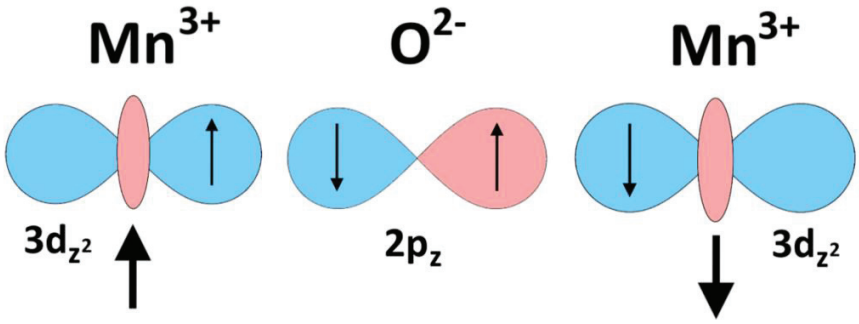

Figure 2: Example of the super-exchange phenomena, here in $AMnO_3$, leading to antiferromagnetic ordering of spins and no net magnetic moment.

Ferro- and piezoelectric compounds, as opposed to ferromagnetic perovskites, are among the most widely applied perovskite structures. The first ferroelectric perovskite, $BaTiO_3$, was described in 1949 and adopts a tetragonal structure (*P4mm*).[21] Perhaps the most technologically important perovskite ferroelectric was described only a few years later; the infamous lead zirconate titanate (PZT). PZT has, in different forms, has been the go-to material for transducers, capacitors and actuators for many years.[22-26] It is important to note, however, that the high lead content of PZT renders its use environmentally malignant. Because of this, finding environmentally friendly alternatives to PZT, while maintaining function, is one of the major goals of materials science today.

Polarization is strictly related to breaking inversion symmetry in the crystal structure, and this is achieved by a translation of one of the metal ions away from its central position. In terms of energy, this is often a result of a *double-well* potential where an off-center position is slightly more energetically favourable than the center position (Figure 3). This is the case for a major share of the perovskite-like and ilmenite-like ABO_3 ferro- and piezoelectrics. Among the $A^+B^{5+}O_3$ compounds, we find this behaviour for $LiNbO_3$ and $LiTaO_3$ in their polar *R3c* structure, in addition to monoclinic (close to tetragonal) $KNbO_3$.[14, 27, 28] There is renewed interest in these materials, as they are environmentally benign and consist of relatively common elements. Doped variants or A_IBO_3:$A_{II}BO_3$ solid solutions can be used to tailor the polarizability of these materials like in PZT, making them viable options in many applications.[29]

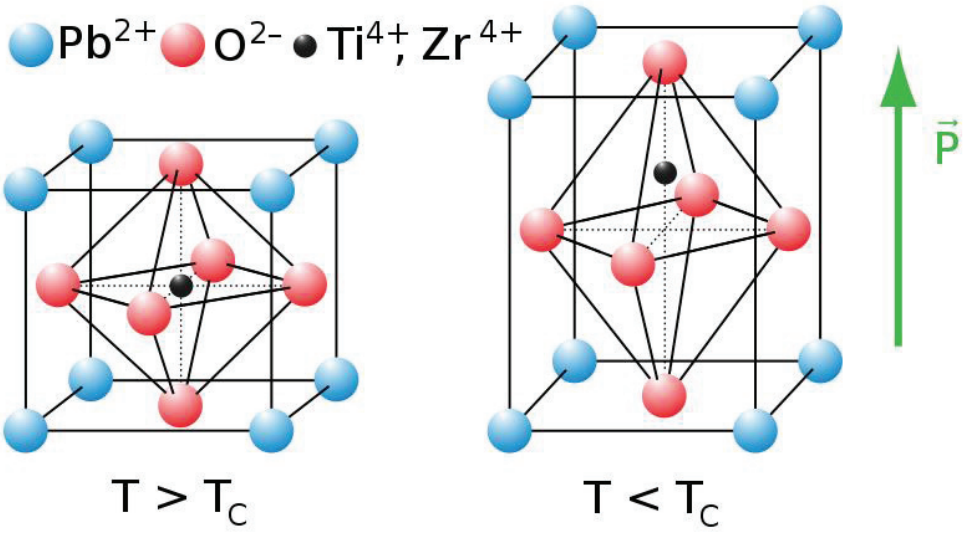

Figure 3: Unit cell of the $Pb(Ti,Zr)O_3$ structure, showing the non-polar structure above the Curie temperature (left) and the polar structure below the Curie temperature (right).

Many uses of polar materials in modern applications require that the materials can be deposited as *thin films*. This is especially true for RF-devices and non-volatile memory, where ferroelectric thin films have been in use for some years. Thin films are also preferable in designing very small sensors and actuators, and for integrated SAW-devices in microwave electronics.[30] These possible applications for thin polar films have resulted in increased interest in the field, and a variety of deposition techniques have been used to achieve as thin and conformal films as possible without sacrificing functionality.

The following text details the structure and properties of the six compounds that have been investigated in this work. Special features of thin films of these structures are introduced, including the techniques that have previously been used to deposit them.

$LiNbO_3$ and $LiTaO_3$

In 1949, Matthias and Remeika reported dielectric hysteresis loops for two materials thought to take the ilmenite structure: lithium niobate and lithium tantalate.[31] The saturation polarization was found to be among the highest in any system reported. This sparked a lot of interest in these compounds, and substantial work has been invested in describing the origin of the polarization that causes the ferroelectric response.

Both $LiNbO_3$ and $LiTaO_3$ exhibit only one phase transformation, paraelectric trigonal (*R-3c, SG #167*) to ferroelectric trigonal (*R3c, SG # 161*) at 1140 and 610 °C, respectively (Figure 4).[27, 32, 33] The phase transformation is caused by hybridization between the b-site atom and surrounding oxygen atoms. This effectively produces a double-well potential for the Li-atom at ±0.37 Å away from the centrosymmetric position, giving rise to its spontaneous polarization. The response is oriented along the *c*-axis. The wells are energetically quite deep, resulting in a very high coercive field in these structures. The theoretical intrinsic coercive field for $LiNbO_3$ is as high as 5420 kV/cm^{-1}, while typical experimental values are ~210 kV/cm^{-1} due to polarization gradients at the 180 °C domain walls.[34, 35]

The high value ferroelectric properties of $LiNbO_3$ and $LiTaO_3$ in addition to the high Curie temperature have increased the attention of these materials. This is especially true for applications in temporary or permanent data storage, in which they can be used to make rapidly switchable and stable states. $LiNbO_3$ has already been used for ferroelectric random access memory devices.[36, 37]

For several of the mentioned applications, it is crucial that $LiNbO_3$ and $LiTaO_3$ can be prepared as a thin film. This offers the possibility to make step-index profiles for surface acoustic wave devices, and allows

for more straightforward dopant introduction. It is also easier to achieve higher electric fields at lower voltage over thin films compared to bulk crystals. As will be introduced in chapter 3, chemical deposition of lithium containing compounds is often difficult due to the volatility and temperature stability of the precursors. The mobility of lithium ions in the structure also creates some challenges that have to be overcome. In addition to this, the thin films have to exhibit c-axis orientation so that the polar axis points out from the surface of the film.

At present, $LiNbO_3$ has been deposited using pulsed laser deposition, molecular beam epitaxy and sol-gel-routes.[38-40] For some of these routes *c*-axis orientation has not been achieved, and others struggle with the conformality of the films. In main paper 1 of this thesis, we introduce a viable route for deposition of c-axis oriented $LiNbO_3$ thin films using atomic layer deposition.

$LiTaO_3$ thin films have been deposited using pulsed laser deposition, RF-sputtering, molecular beam epitaxy and sol-gel routes, in addition to a recent report using atomic layer deposition[41-44].

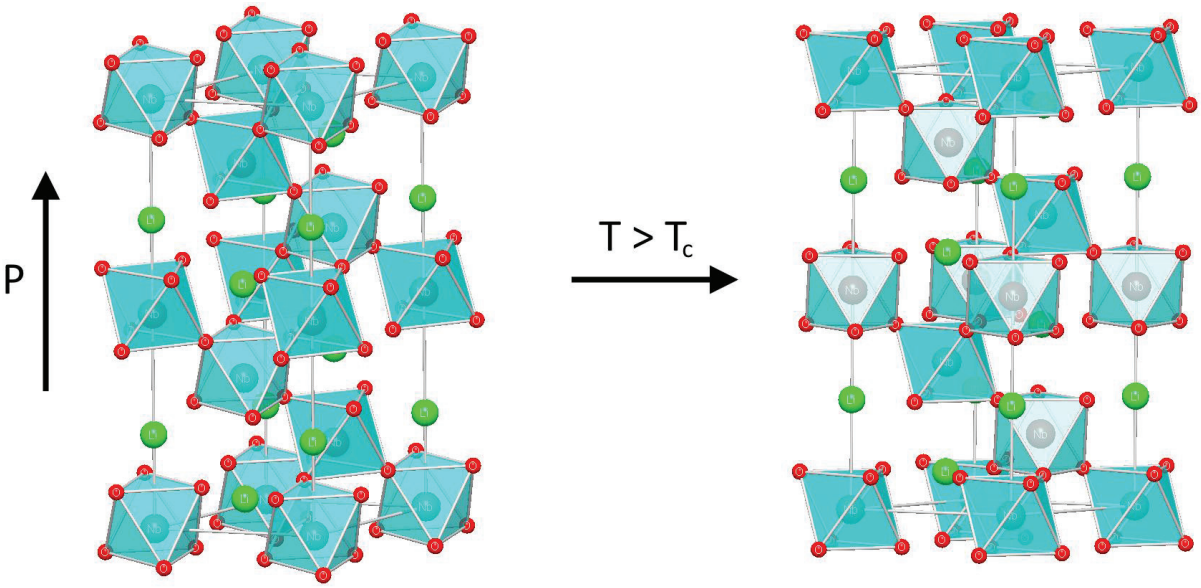

Figure 4: Phase transition in $LiNbO_3$ from the rhombohedral ferroelectric (left, SG #161) to the rhombohedral paraelectric (*right, SG # 167*) structure, at the Curie temperature. The same phase transition is found for $LiTaO_3$.

$NaNbO_3$

Sodium niobate, $NaNbO_3$, is a well-known anti-ferroelectric at room temperature, with an orthorhombic perovskite structure (*Pbcm, SG: #57*). Unlike lithium niobate, $NaNbO_3$ undergoes a large set of phase transitions until it finally reaches the cubic perovskite structure at 913 K.[45] Upon heating at 753 K it transforms from the antiferroelectric *Pmnm* structure to the paraelectric *Pnmm* structure. Cooling to below liquid nitrogen temperatures has been reported to yield the $LiNbO_3$ structure (*R3c*), but the exact temperature where this happens is heavily debated.[46] At least six polymorphic phase transitions are found for the $NaNbO_3$ system, and the driving force for all these is not clearly understood. The complex set of transformations that $NaNbO_3$ undergoes, and the lack of polar states at room temperature, has rendered it more or less useless in modern applications. It is, however, heavily studied in solid solution with $KNbO_3$, where the morphotropic phase boundary between the ferroelectric and antiferroelectric states at room temperature is used to tune the piezoresponse.

Thin films of $NaNbO_3$ have been deposited using pulsed laser deposition, CVD, RF-sputtering and sol-gel routes.[47-50] Studies of the unstrained congruent compound have mainly focused on photocatalytic activity, where the orientation of the films is not crucial.[51] Although bulk $NaNbO_3$ is not spontaneously polarized at room temperature, thin films can be designed to become ferroelectric through strain or doping. As an example, polar films of $NaNbO_3$ have been reported on (110)-oriented rare earth scandate substrates.[52] This creates a compressive in-plane strain of the $NaNbO_3$ lattice that facilitates spontaneous polarization.

In main paper 3 of this thesis, an ALD route producing oriented $NaNbO_3$ thin films is reported.

$NaTaO_3$

Sodium tantalate, $NaTaO_3$, is an incipient ferroelectric; a material that never reaches its polar structure even if such a structure is expected.[53] It undergoes three phase transitions between 903 and 720 K, but all are paraelectric cubic, tetragonal or orthorhombic structures (Figure 5). Quantum fluctuations inhibit the transformation to a polar phase at lower temperatures. This does not, however, make it an unimportant material, as it is investigated as an effective photocatalyst for water splitting.[54] Especially lanthanide-doped variants are found to exhibit a remarkable splitting rate.

Thin films of stoichiometric $NaTaO_3$ have gained very little interest from the community due to its incipient ferroelectric nature. Doped variants, especially lanthanum-substituted, has on the other hand

been thoroughly studied due to their photocatalytic activity. High surface area structures with La:$NaTaO_3$ coating have been shown to exhibit a much higher water splitting rate than its bulk counterpart. Deposition of $NaTaO_3$ thin films has currently been achieved by sol-gel, CVD, hydrothermal and sputtering routes.[55-57]

In main paper 3 of this thesis, an ALD route producing oriented $NaTaO_3$ thin films is reported. Conformal coating on high aspect ratio substrates is really the sweet spot of ALD, so this is believed to be of high interest to the community.

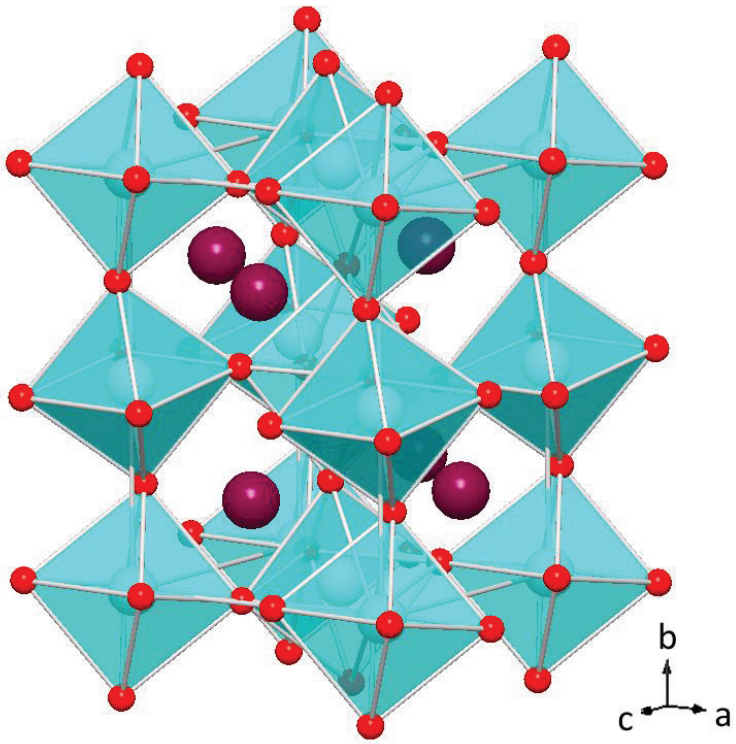

Figure 5: The orthorombic room temperature structure of $NaTaO_3$. Quantum fluctuations hinder the transition to an expected ferroelectric state.

$KNbO_3$

Potassium niobate, $KNbO_3$, is a room temperature ferroelectric, exhibiting a phase transition between the cubic paraelectric (*Pm-3m*) phase to the tetragonal ferroelectric (*Amm2*) phase at 708 K.[14] The relatively high Curie temperature makes it a lead free alternative in many applications. Low tunability in the undoped congruent system is one of the key limitations, but this can be overcome by using it in solid solution with $NaNbO_3$ along the morphotropic phase boundary.

Another important solid-solution is the combination of $KNbO_3$ and $KTaO_3$, providing ferroelectric character and excellent electrooptical response. As an example, $K(Ta_{0.65}Nb_{0.35})O_3$ has a very high quadratic electrooptical coefficient, and is used in high accuracy band filters, IR detectors and electrooptic modulators.[58]

Growing congruent $KNbO_3$ bulk crystals with high structural quality and low defect concentration has been a goal for material scientists for many years.[59] This is due to the order of magnitude higher electromechanical coupling coefficient as compared to $LiNbO_3$, which is the most widely applied lead free material in SAW-devices. Obtaining these bulk crystals have proven to be intrinsically difficult and currently most work is put into growing thin films where the structural quality is often easier to control.

Thin films of $KNbO_3$ has been deposited using pulsed laser deposition, chemical vapour deposition, ion beam sputtering and through sol-gel routes.[60-63] These techniques require high temperatures, and the films are thus prone to interfacial reactions towards the substrate and to substrate cracking upon cooling due to residual thermal stress. In addition, potassium ions are volatile and very mobile at high temperatures. A hydrothermal epitaxy route has been reported for deposition of films down to 200 °C.[64] This route led to tower-like structures with different out-of-plane orientations through nucleation and island growth, making ferroelectric functioning difficult.

In main paper 3 of this thesis, ALD is used to deposit oriented $KNbO_3$ thin films at temperatures down to 250 °C. This maintains ferroelectric functionality while avoiding cracking, while still preserving the possibility to tune the composition.

$KTaO_3$

Potassium tantalate, $KTaO_3$, is the only compound of the six to take the perfect cubic perovskite structure at room temperature.[65, 66] It is, as the sodium counterpart and $SrTiO_3$, an incipient ferroelectric where the onset of a ferroelectric phase is inhibited by quantum fluctuations. The nature of this inhibition is interesting from a fundamental point of view, but limits the usefulness of the material on its own, as the cubic symmetry does not allow polarization. As mentioned, however, $KTaO_3$ in solid solution with $KNbO_3$ has attracted a lot of interest for its electrooptical properties.

Thin films of $KTaO_3$ have not been widely studied, as it does not intrinsically possess very interesting functional properties and deposition routes are few. Reports have been made of thin films deposited by pulsed laser deposition and hydrothermal epitaxy.[65, 67] In the latter case, $KTaO_3$ was studied as a buffer

layer towards superconductors, as it has a dielectric non-linearity close to the critical temperature of many high T_c superconductors. It also has a very close lattice match to $KNbO_3$, making it a viable buffer layer for growth of oriented ferroelectric films of $KNbO_3$.

In main paper 3 of this thesis, ALD is used to deposit oriented $KTaO_3$ thin films.

Important Solid Solutions

Two very important solid solutions have already been briefly mentioned, but are of so great importance for modern applications that they deserve a more thorough introduction.

The solid solution between ferroelectric $KNbO_3$ and the *anti*ferroelectric $NaNbO_3$ (KNN) is one of these. This system exhibits three morphotropic phase boundaries, at 52.5, 67.5 and 82.5 mole % $NaNbO_3$ at 25 °C respectively, all of them separating different orthorhombic structures.[68] Piezoelectric performance is typically reported by the piezoelectric coefficient (d_{33}) and the electromechanical coupling coefficient (k_p), and these values are always found to be highest near a morphotropic phase boundary. Out of the three boundaries in KNN, the one at 52.5 mole % $NaNbO_3$ is found to exhibit the highest piezoelectric coefficients and tunability around the boundary composition. Although the coefficients are high for the KNN system, they still cannot compete with the values around boundaries in the PZT system. To find a viable lead free alternative to PZT, efforts have been made to increase performance by doping the KNN matrix. State-of-the art alkali niobates are today close to PZT in performance, with one of the highest performing examples being $(1-x)(K_{1-y}Na_y)-(Nb_{1-z}Sb_z)O_3 - xBi_{0.5}(Na_{1-w}K_w)_{0.5}ZrO_3$, where x = 0.04, y = 0.52, z = 0.05 and w = 0.18.[29]

Thin films of KNN have also gained much attention over the last decades. The challenges reported for deposition of congruent $KNbO_3$ and $NaNbO_3$ is of course also true for KNN, with further complexification due to the mixing of two hard-to-deposit systems. Current deposition techniques include RF-sputtering, pulsed laser deposition, aerosol deposition and chemical solution deposition, all resulting in (100)-oriented films on most substrates.[69-74] Alkali metal loss resulting in oxygen vacancies is often reported, leading to large unwanted leakage currents. In addition, complex domain wall structures in the thin films are often detrimental to the piezoelectric properties. Nonetheless, reports have been made of KNN thin films outperforming its bulk counterpart, underlining the need of robust deposition routes for these structures.

In main paper 3 of this thesis, ALD is used to deposit oriented KNN thin films at low temperatures, minimizing the challenges of alkali metal loss.

The second very important solid solution is the combination of $KTaO_3$ with $KNbO_3$ (KTN). Phases in this solid solution cannot compete with the piezoelectric properties of KNN, but have striking electrooptical properties for selected compositions. The most studied is $KNb_{0.35}Ta_{0.65}O_3$, a paraelectric cubic structure with a very high electrooptical coefficient and photorefractive effect.[58, 75, 76] This large change in refractive index as a response to permutation by an external field can be used to make high performance optical modulators, where phase or intensity of light is modulated by an electric signal.[77] In KTN, the electrooptical effect is quadratic, giving rise to much larger variations than in the current workhorse of electrooptics, $LiNbO_3$, where the response is linear. Theoretically, the electrooptical effect in KTN is orders of magnitude larger than in $LiNbO_3$, but challenges in synthesis of perfect crystals results in diminishing coupling. This has delayed the onset of KTN employed in modern applications.

Deposition of KTN thin films faces the same challenges as that of KNN. Current techniques include pulsed laser deposition and sol-gel routes, but again performance is inhibited by high temperature treatment causing cracking and alkali metal loss.[78, 79]

In main paper 3 of this thesis, ALD is used to deposit oriented KTN thin films at low temperatures.

Interfaces with Exotic Functionality

A very recent addition to the world of alkali metal niobates and tantalates is investigating the properties of interfaces towards other materials. This had its onset in 2004 when Ohmoto and Hwang reported superconductivity at the interface between the two insulators $LaAlO_3$ and $SrTiO_3$.[8] This system is thoroughly described in supporting paper 1, where this interface was prepared by ALD.[80] The $LaAlO_3||SrTiO_3$ interface has later been shown to exhibit a range of exotic properties, including interfacial ferromagnetism and conductivity created by a 2D electron gas.[9, 81, 82] Although this system is not yet fully understood, the properties arise from the polar discontinuity at the interface between neutral TiO_2^0-layers and LaO^+-layers. This type of effect is of course not limited solely to $LaAlO_3||SrTiO_3$, and a lot of effort is now put into finding other systems exhibiting similar effects.

One set of systems that is theoretically predicted to exhibit such effects utilizes the polar KO^--, NbO_2^+-, and TaO_2^+-layers of $KNbO_3$ and $KTaO_3$ to obtain the same type of discontinuity towards other perovskites (Figure 6).[83, 84] Examples include $KTaO_3||CaSnO_3$, $KNbO_3||ZnSnO_3$, $KTaO_3||PbTiO_3$ and

$KTaO_3$||$LaTiO_3$, the latter being the only experimentally verified system.[84-86] $KTaO_3$ and $LaTiO_3$ are both insulators (band and Mott, respectively), but the interface exhibit metallic conductivity from 2 K to room temperature.

The lack of experimental verification is mainly due to difficulties in preparation of alkali niobate and tantalate structures. In the case of the reported $KTaO_3$||$LaTiO_3$-system, a thin film of $LaTiO_3$ was deposited on a substrate of $KTaO_3$. By using a thin film technique that can facilitate deposition of both components, multilayer systems with more explicit functional properties can be obtained. Relatively straightforward multilayer deposition is one of the other advantages of the atomic layer deposition technique.

With the onset of low temperature deposition of $KTaO_3$ and $KNbO_3$ thin films with good orientation and low alkali loss, many more systems should be possible to investigate.

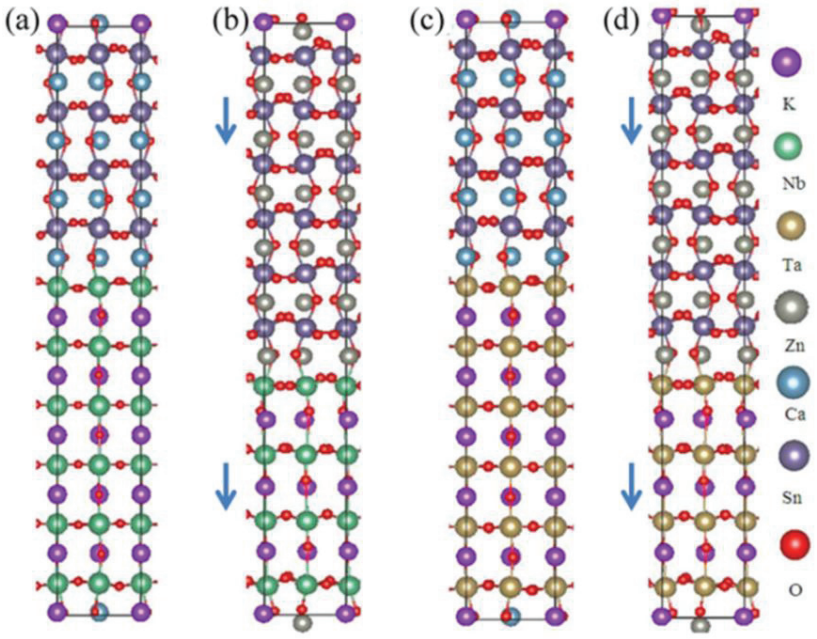

Figure 6: 2-dimensional electron gas at perovskite interfaces between $KTaO_3$ or $KNbO_3$ and stannates.[85] Reused with permission from PLOS One, under a CCA license.

In main paper 3 of this thesis, proof of concept of deposition of epitaxial films of $KNbO_3$ and $KTaO_3$ on $SrTiO_3$ and $LaAlO_3$ substrates is reported.

3. Atomic Layer Deposition

Atomic layer deposition is a chemical vapour deposition technique for synthesis of thin films on the nanometer scale. The idea was conceived by Kol'tsov in 1952, but was first properly formalized 25 years later by Suntola *et al.* with a working reactor to deposit zinc sulphide thin films for flat panel displays.[87] Interest in the technique has grown massively over the last 25 years, and today processes for several hundred compounds have been reported. The instrumentation, chemistry and history of the ALD technique have seen many reviews, and will only briefly be discussed here to give the work some perspective.[88-91]

ALD instrumentation comes in many flavours, and the geometry, size, type of precursor delivery *etc.* vary. The basic idea is, however, always the same: Layer-by-layer, self-limiting growth of thin layers by alternately pulsing precursors and purging the excess, before pulsing a second precursor with another subsequent purging step. This is repeated until the desired thickness of the resulting film is reached. The amount of different precursors, and the pulsed ratio between the precursors, varies depending on what composition that is wanted in the product.

Precursors that can be used in ALD growth need to have some important traits. They must have a sufficient vapour pressure below the reaction temperature, they must adsorb to or react with the surface without condensing and they cannot react with themselves or decompose under the working conditions applied. As a result of this, every precursor has an *ALD-window*, a temperature region in which growth is self-limited and linear. A traditional ALD-window is shown in Figure 7.

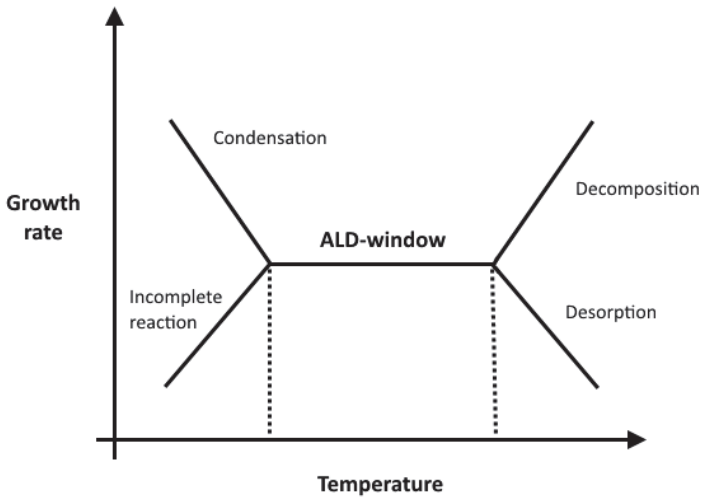

Figure 7: A typical ALD-window with uncontrolled growth regimes for low and high temperatures.

Precursors working as cation sources are typically one of two types:

- Metal-organic compounds. Simple molecules like trimethyl aluminium ($Al(CH_3)_3$) or diethyl zinc ($Zn(CH_2CH_3)_2$), or molecules with larger ligands like *thd* (2,2,6,6-tetramethyl-3,5-heptanedionato) or *hfac* (hexafluoroacetylacetonate).
- Metal-halide compounds. $TiCl_4$ or $AlCl_3$ are typical examples.

Precursors working as anion sources are often simple inorganic molecules such as H_2O or O_3 (for oxide deposition), or NH_3 (for nitride deposition). Pure organic precursors, such as amino acids or dicarboxylic acids for depositing hybrid inorganic-organic films, can also be used.

The purging step typically involves an inert gas (N_2 or Ar), that helps remove any excess precursor. Failure to remove any unreacted precursor will lead to uncontrolled growth when the next precursor is introduced to the reaction chamber. Figure 8 shows a simple sketch of the ALD growth principle, exemplified by growth of Al_2O_3 by TMA and water.

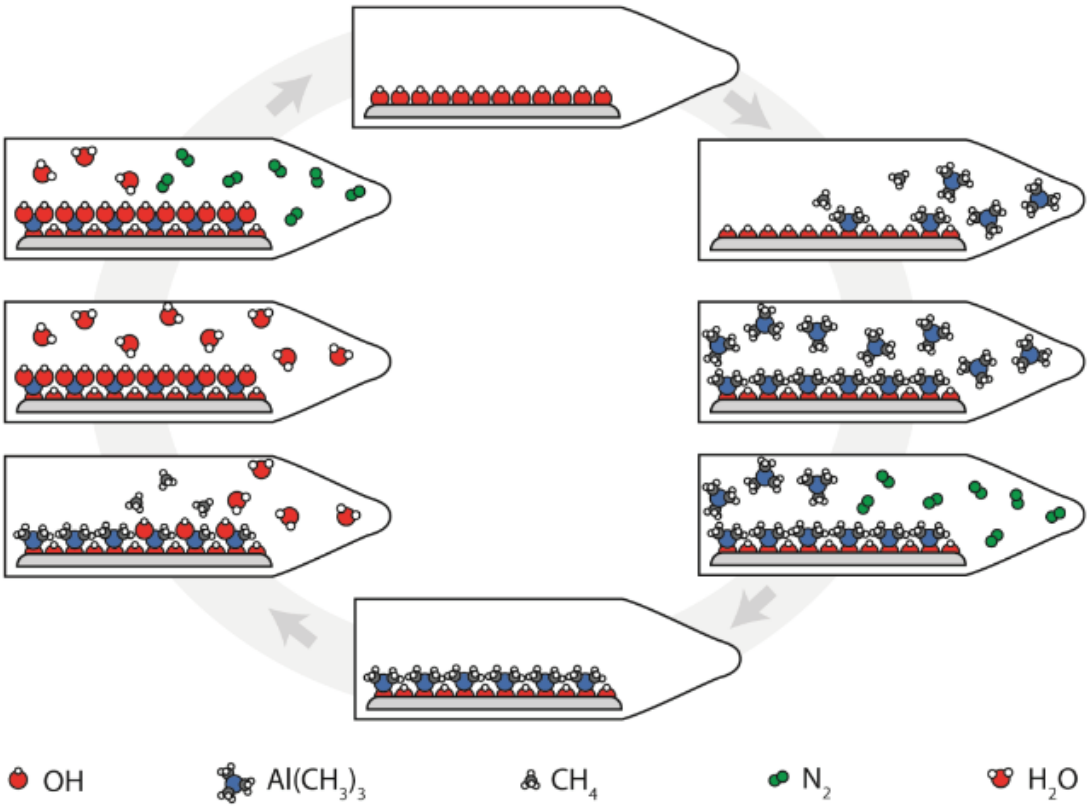

Figure 8: Simple sketch of ALD Al_2O_3 growth by TMA and water. The figure is reused from Ingrid Vee's master thesis.[92]

In addition to traditional molecular precursors, assisted growth by some perturbation is also more and more common. This can, among other things, be plasma-assisted growth, radical-enhanced growth or photo-assisted growth.[93-95]

The self-limiting nature of ALD gives rise to a set of advantages and drawbacks that are important to consider. Primarily, a working process allows the user to deposit extremely conformal films, even on substrates with complex morphology and on high aspect ratio surfaces. As long as the precursors have enough time to reach all active sites before the purging step, they will uniformly cover the substrate surface. An ideal process with true layer-by-layer growth will also facilitate a sub-nanometer thickness control of film growth, only limited by the growth rate (growth per cycle). As an example, for growth of alumina by TMA and water, the growth rate is 1.3 Å/cycle and the thickness can be controlled thereafter.

A third advantage is the chemical versatility that the ALD technique claims. Oxides of more than 50 metallic elements have been grown, and pure elemental films are reported for more than 20. Routes for depositing nitrides, sulphides, fluorides and hybrid films for many of these elements also exist.

Finally, the low deposition temperature in an ALD-system compared to *e.g.* MBE or PLD, allows for deposition of compounds that are not available by physical techniques.

The layer-by-layer growth that facilitates the important advantages of the technique also creates some disadvantages that are important to consider. First of all: ALD is relatively slow. A single deposition is rarely performed in less than an hour, and often several hours are needed to deposit a film in the 10 – 100 nm thickness range. Furthermore, the chemistry governing the reaction mechanisms leave little room for control of oxidation state. The metal in a metal oxide will very often be in its highest possible oxidation state, and finding feasible routes for depositing reduced variants is non-trivial.

For industrial applications, it is also important to note that ALD is an expensive technique. This is due to the rate of growth, but often also high costs of the precursor. The purge step ensuring self-limiting growth means that some of the precursor will go to waste when flushed out of the system. This challenge can often be overcome, or its implications reduced, as pulsing parameters can be tuned to minimize the precursor loss.

ALD of complex oxides

The simple reaction mechanisms described in the introduction to ALD is often limited to a two-precursor process, in which a metal precursor and an oxidizing agent lead to a film with binary composition. These mechanisms are typically only limited by the ALD-window of the metal precursor. In the 1990's, attempts were made to widen the possibilities of ALD growth by adding a second metal precursor to form ternary oxides. This opened up for deposition of a wide range of functional materials with *e.g.* perovskite or spinel structure that are important for modern applications.

The basic idea is to combine two processes for binary oxides to form a ternary oxide. An early example of this was ALD of $LaNiO_3$ thin films by combining processes for La_2O_3 and NiO.[96] As introduced for the general case, both metal-precursors exhibit an ALD-window, in which the growth rate is constant over a certain temperature range. When combining the two metal precursors, the ALD-window for the whole system will be more complex as temperature stability will be a superposition of the two binary systems. Some systems will in fact be impossible to combine, if there is no overlap in temperature between the two binary windows. The mechanisms governing the growth may, however, drastically change in a ternary system, facilitating growth even if there is no overlap in the ALD-windows. The growth of $LaMnO_3$ is an example of this.[97] Going back to the early example of $LaNiO_3$, Figure 9 shows the ALD-windows of the binary processes as compared to what is reported for the combined system. $Ni(thd)_2$ is known to not have a well-defined window, however, the growth rate is relatively constant between 225 and 250 °C. $La(thd)_3$ on the other hand has a proper ALD-window in the 225 to 275 °C temperature range.

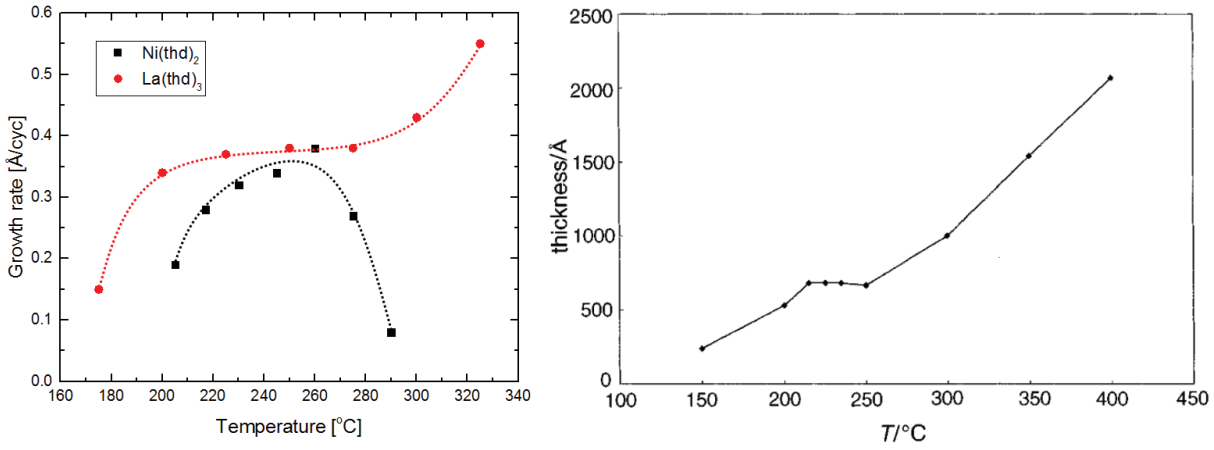

Figure 9, Left: Growth rates for the binary oxides NiO (black) and La_2O_3 (red). Right: Thickness (after 100 supercyles) as a function of reactor temperature for thin films in the combined La-Ni-O-system. Reused with permission from Royal Society of Chemistry.[96]

For the combined growth of the two binary systems to form $LaNiO_3$, constant growth rate is observed between approximately 220 and 250 °C. This coincides very well with an effective narrowing of the ALD-window by choosing a temperature region where both metal precursors show constant growth rate. This simple approach can be an effective guideline when choosing precursors for a working complex system. For many systems, life is not this simple. Several side-effects can occur when combining two mechanisms, and this can be either a curse or a blessing. Increased or decreased growth of one or more of the precursors is common, seen for example in the growth of $LaPO_4$.[98] Stabilization of an increased temperature range expanding the ALD-window of the complex oxide is also observed, for example in the $CaMnO_3$-system.[99] True non-compatibility leading to uncontrolled growth when combining two precursors is known to happen, even inside their binary ALD-windows. An example of this is deposition of ZnO/Al_2O_3 alloy films, where high ZnO-ratios lead to Zn-etching.[100] This ultimately means that even if two binary processes have a matching ALD-window this is not a guarantee for success.

Upon finding two precursors that can be used together for ALD of ternary or higher compounds, other challenges also emerge. Obtaining films with some arbitrary amount of the desired metals is not sufficient, the *ratio* between the two metals is essential to form the wanted composition. If one of the binary systems grows much faster than the other, more of the element comprising that binary structure will be incorporated in the film. To obtain the correct stoichiometry, the pulsed ratio between the metal precursors often has to be tuned.

A straightforward approach for doing this was proposed by Lie *et al.*[101] Since the concentration of an element in a thin film is directly proportional to the growth rate, the pulsed ratio between the metal precursors should be the same as the ratio between the growth rates of the binary systems. This approach is found to work well for many systems, especially when the metal-precursors of the different binary systems have similar chemistry, *e.g.* in Lie's case where all metal-precursors have thd-ligands.

In more intricate ALD mechanisms, comprising precursors with very different ligands exhibiting complex growth behaviour, the method can only be used as a first guess for the pulsed ratio. An example of this is discussed for growth of $LaAlO_3$ by $La(thd)_3$, TMA and ozone (Figure 10).[80]

The red dotted line shows the theoretical ratio between La and Al as calculated by Lie's method. The goal in this work was to deposit films of the perovskite $LaAlO_3$, obviously having a 1:1 ratio between the metals. By following the dotted line this should correspond to a pulsed ratio of about 9:4, La:Al. What is observed, however, is that the pulsed and stoichiometric ratios follow an almost linear relationship. Work was done to determine the reason behind this growth, but strictly solving the growth rate equations was not possible. It was evident that Al-O-terminated surfaces has a higher number of active sites and offer

better growth conditions for further growth than La-O-terminated surfaces. This is not surprising, as the thd-ligands are larger than the methyl groups. This observation was not enough to explain the growth, as it seemed that also the second and third preceding layer influenced the growth. A more detailed explanation can be found in supporting paper 1, but this goes to show that reaction mechanisms in complex oxide growth are often difficult to fully understand.

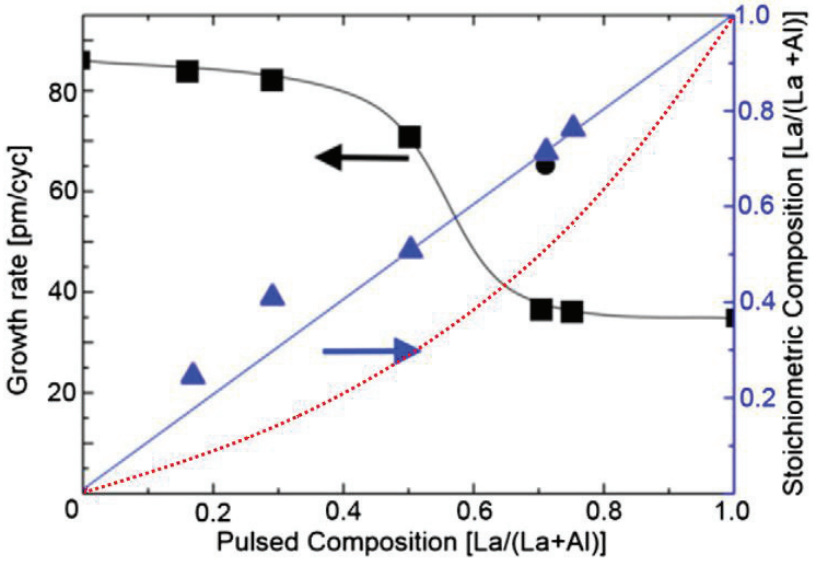

Figure 10: The growth rate (black) and stoichiometric composition (blue) of the La-Al-O-system. The red dotted line shows the expected composition as calculated by Lie's method.[101]

A final issue that should be raised in conjunction with this thesis is the crystallinity of ALD thin films. Growth of complex oxide systems very rarely lead to films that are epitaxial as deposited, this is related to the varying size of precursors.[102] Even if the substrate to film lattice match is very good, the steric hindrance from the precursors does not allow proper layer-by-layer single crystal growth. As a result of this, post-deposition annealing is usually applied to crystallize the films. There has been a productive debate in the community whether this leads to a film crystal quality and substrate-film interface quality that can facilitate the desired functional properties.

Several reports have been made, especially over the last 10 years, on functional perovskites by ALD. This research is summarized in the review paper that is referred to in the beginning of this thesis, and a more detailed discussion can be found there.[20] What is important to note is that most, if not all, complex oxide systems are either amorphous or polycrystalline to some degree as deposited. With a post-deposition annealing step, however, typically 600 – 800 °C, it is possible to obtain samples with proper epitaxy with

a near perfect interface region. The structural integrity will depend on many parameters, including annealing temperature and ramp rate, cooling rate, chemical quality of the film, structural quality of the substrate surface and substrate to film lattice mismatch.

Two very illustrating examples are shown in Figure 11. One is taken from the $LaAlO_3||SrTiO_3$-system reported in supporting paper 1, the other on $BiFeO_3$-deposition by Akbashev *et al.* In the $BiFeO_3$-system a near perfect epitaxy is observed.[103] Akbashev *et al.* studied the epitaxial relationship in detail and determined the quality to be close to, if not as good, as that observed for films grown by PLD or MBE. The lattice match is very good, and the substrate quality is impeccable. In the $LaAlO_3$-system, an evident interfacial region with structural defects can be observed near steps on the substrate surface. This leads to incommensurate growth of a structure with severe defects, which relaxes and turns into the proper $LaAlO_3$-structure further away from the interface. At interface regions where the substrate is smoother, this effect is much less pronounced.

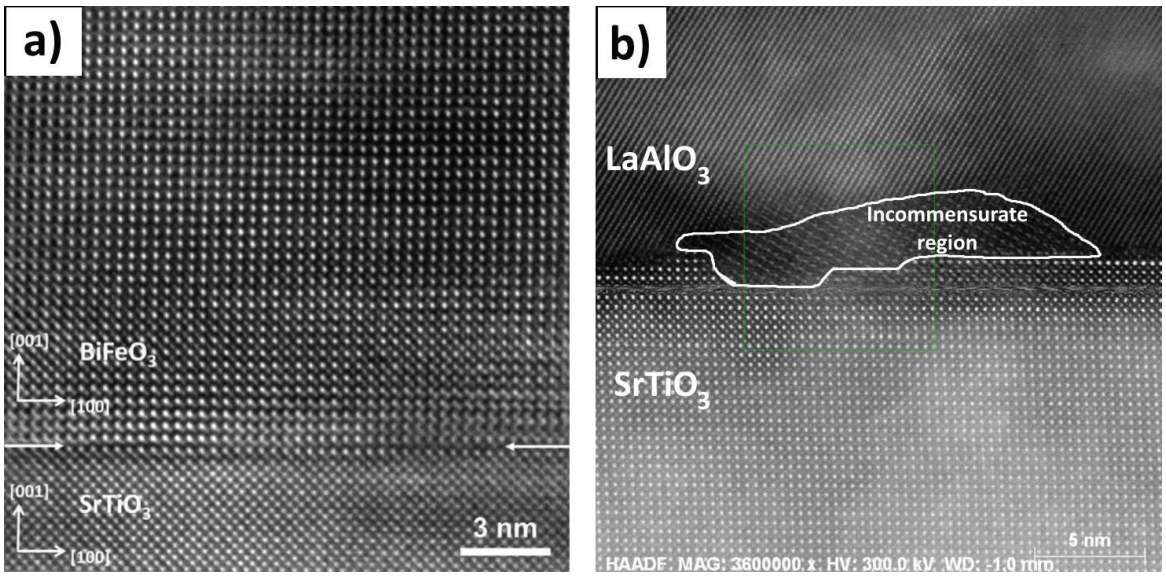

Figure 11, Left: Near perfect epitaxy of a $BiFeO_3$ thin film grown by ALD on a $SrTiO_3$-substrate. Reused with permission from the American Chemical Society. [103] Right: $LaAlO_3$ thin film grown by ALD on a stepped $SrTiO_3$-substrate leading to incommensurate crystal domain growth.

These recent reports underlines that ALD is not a technique limited to high-k materials and films where crystal structure is not of high importance. It can most definitely be used to deposit conformal films of functional materials with magnetic and electric properties that are highly sought after.

ALD of thin films containing alkali metals

The final part of this introduction to ALD will briefly introduce current research on deposition of alkali metal containing thin films. This is a very new field of ALD-research and first reports of lithium deposition were published as late as in 2009, in Putkonen *et al.*'s pioneering paper.[104] Several precursors were tested for ALD growth in this report, and self-limiting growth of Li_2CO_3 was observed for Li(thd) and Li(O^tBu). This research led to several reports on lithium containing materials in the following years, all focused on materials used for solid-state lithium batteries. This research was summarized in a recent review by Nilsen *et al.*[105]

Alkali metal deposition involves some challenges that are not found for most other metals. Ions of alkali metal elements are small and often very mobile in a solid matrix. They have a large affinity towards water and CO_2, which makes investigation of pure binary systems very difficult. Testing alkali metal precursors are often done by depositing aluminates or similar compounds to overcome this challenge. The affinity for reaction with CO_2 can lead to carbon contamination that may quench desired functional properties. Affinity for water is detrimental in ALD-processes, as water is often used as an oxygen source. This can lead to formation of hydroxides and storage of crystal water, which again can influence further growth. This is known as the "reservoir effect" and was discussed at length in Erik Østreng's Ph.D.-thesis, and will not be discussed further here.[106]

Furthermore, characterization is often difficult. This is especially the case for lithium, as its interaction with x-rays is very small. Traditional methods for determining metal-to-metal ratios in thin films, like XRF, are not sensitive to lithium. XPS is sensitive, but depth resolution is limited without ion-etching. Ion etching is not applicable as this will see lithium migrating towards the interface between the film and the substrate, and the concentration will subsequently be misinterpreted. Time of flight elastic recoil detection analysis (TOF-ERDA) is routinely used, but infrastructure is expensive making instrumentation hard to come by.

Before the work leading to this thesis was commenced, no route for depositing sodium- and potassium containing films existed. All the challenges related to lithium deposition are also found for sodium- and potassium, and without the driving force of battery research, this has been left unexplored by the ALD community. Developing new processes for these elements was needed to be able to deposit important functional compounds containing sodium and potassium.

With all these challenges, why care about ALD of alkali metal containing compounds? Many of the proposed applications for these thin films require conformal structures on high-aspect ratio systems, and

other techniques cannot match ALD in this context. Examples are 3D solid-state batteries and devices utilizing surface acoustic waves. Thermal stability of many alkali metal compounds is also an issue, as many physical techniques require temperatures these structures cannot withstand. ALD processes work at much lower temperatures, opening for thin film deposition of structures that are not readily available by PLD, MBE or other technqiues. ALD of alkali metal compounds is in other words highly anticipated, and the challenges related to it must be overcome.

4. Methods of Characterization

An integral part of materials science is characterisation of the intrinsic properties of materials. These can be structural, mechanical, chemical, physical or functional properties. Without surveying the inherent traits of the materials made, the value of the research is reduced to superficial significance. This chapter covers briefly the essential characterization tools that have been employed in this work, with some more elaborate discussion on selected critical techniques that are not treated as well in literature.

X-ray Based Techniques to Study Thin Films

X-ray radiation has been the most widely applied probe for characterizing materials since their discovery by Röntgen in the late 19th century.[107] Like all light, x-rays interact with matter in one of two manners; through *scattering* or *absorption*. Scattering is an *elastic* event, in which the energy of the incoming photon, and thus the wavelength of the light, is unchanged. Absorption, on the other hand, is an *inelastic* event, in which some or all of the photon energy is transferred. X-rays are typically defined to have an energy of 0.1 – 100 keV, corresponding to a wavelength of 0.01 – 10 nm. This coincides well with both electron binding energies and atomic distances in solids, giving rise to a large variety of characterization techniques that utilizes x-rays as the probe. Studying *thin films* with these techniques involves some special considerations and constraints that should be introduced.

X-ray diffraction (XRD), x-ray reflectivity (XRR), x-ray photoelectron spectroscopy (XPS) and x-ray fluorescence (XRF) have routinely been used to study thin films in this work.

X-ray Scattering Techniques

X-rays are scattered from matter, either through elastic interactions with the regular array of atoms found in crystals, or through reflection from surfaces and interfaces. This is the basis of the two main scattering techniques in hard thin film materials science; XRD and XRR respectively.

XRR has been routinely applied to study the thickness, density and roughness of thin films and buried layers throughout the work leading to this thesis. This gives invaluable information on the structure of surfaces, interfaces and buried layers that are crucial for understanding the material properties of the thin films and multilayers.

XRR is a thin layer specific technique. The propagation of light in a medium, and the way it behaves on the interface is directly related to the refractive index *n*, which for x-rays is given as:

$$n = 1 - \delta + i\beta \qquad \textbf{Eq. 2}$$

$$\delta = \frac{\lambda^2}{2\pi} r_e \rho_e \quad , \quad \beta = \frac{\lambda}{4\pi} \mu_x \qquad \textbf{Eq. 3}$$

where r_e = 2.82 x 10^{-15} m is the classical electron radius, ρ_e is the electron density of the material and μ_x is the absorption length of the system. Since δ must be larger than 0, the refractive index of x-rays is slightly less than unity. This gives rise to *total reflection* of x-rays below a critical angle, $\alpha_c = \sqrt{2\delta}$, which is often in the vicinity of 0.2°-0.5°. Also note that β is a very small value, and is often ignored. Higher electron density in the thin film leads to higher critical angle for total reflection.

Traditional utilization of x-ray reflectivity deals with *specular* reflection, where the incident (α_i) and reflected angle (α_f) are the same.

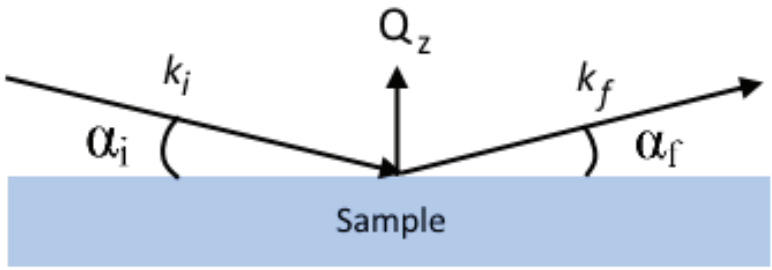

Figure 12: Reflection geometry of x-rays on a flat sample, showing the equal incident and outgoing angles.

The momentum transfer in Q-space along the surface normal *z*, is found to be:

$$\overrightarrow{Q_z} = \overrightarrow{k_f} - \overrightarrow{k_i} = \frac{4\pi}{\lambda} \sin\alpha_i \, \overrightarrow{e_z} \qquad \textbf{Eq. 4}$$

Where $\overrightarrow{e_z}$ is the standard basis vector in *z*-direction. For a perfect sharp surface, the reflection coefficient was described by Fresnel and reads:

$$r = \frac{k_z - k'_z}{k_z + k'_z} \qquad \textbf{Eq. 5}$$

Where k_z and k'_z are the vertical components of the incident and transmitted waves. The intensity of the reflected wave is found by taking the square of the reflection coefficient. Now, close to the critical angle of total reflection, k'_z is governed by reflection as:

$$k'_z = k\sqrt{\alpha_i - \alpha_c} \qquad \textbf{Eq. 6}$$

giving a purely imaginary component at angles below the critical angle. Above the critical angle the intensity of the reflected beam will drop drastically, proportional to α_i^4. Roughness is also detrimental to reflection, and for any real sample this will play a role. This can be taken into account by a roughness coefficient given as:

$$R = e^{-2k_z k'_z \sigma^2} \qquad \textbf{Eq. 7}$$

where σ is the surface roughness. The reflection can now be described in full by $r = r_{ideal}R$.

A thin film on a substrate does not consist of a perfect surface, but rather of at least one additional interface in addition to the surface. When this is the case, scattering from all of the interfaces must be taken into account, increasing the complexity of the reflection. This was formalized by Parratt, when he related the reflected and transmitted amplitude as:

$$\boldsymbol{X}_j = \frac{\boldsymbol{R}_j}{\boldsymbol{T}_j} = e^{-2ik_{z,j}z_j}\frac{r_{j,j+1} + \boldsymbol{X}_{j+1}e^{2ik_{z,j}z_j}}{1 + r_{j,j+1}\boldsymbol{X}_{j+1}e^{2ik_{z,j}z_j}} \qquad \textbf{Eq. 8}$$

where r_j is the Fresnel coefficient of interface j. Note that this formalism can handle an unlimited amount of interfaces. This is a recursion formula which can be solved by taking $T_1 = 1$ and $R_{N+1} = 0$, which translates into normalizing the incident wave to unity and disregarding reflection from the substrate itself respectively.

The reflected waves will now interfere, giving rise to what is known as Kiessig fringes with periodicity $2\pi/d$, where d is the thickness of the thin film. Again, roughness can be taken into account with the same roughness coefficient as for a single surface, as long as the roughness is small compared to the thickness of the layer.

Using Parratt's formalism to solve the reflection from a real system is near impossible. The way around this is to use what has been called the *Master-formula*, which by a kinematical approximation is given by:

$$R(Q_z) = R_F \left| \frac{1}{\rho_e(z \to \infty)} \int \frac{d\rho_e}{dz} e^{iQ_z z} dz \right|^2 \qquad \textbf{Eq. 9}$$

Where R_F is the reflected intensity and ρ_e is the electron density profile of the system. The Master-formula is rarely applied to solve systems directly, but is used together with software algorithms to fit a theoretical curve to real data. Fitting parameters are typically layer thickness, density and roughness, related to the period of fringes, critical angle for total reflection and intensity drop-off, respectively. Figure 13 shows how a typical XRR-dataset may look, and how fringes are formed as the thickness of the film increases.

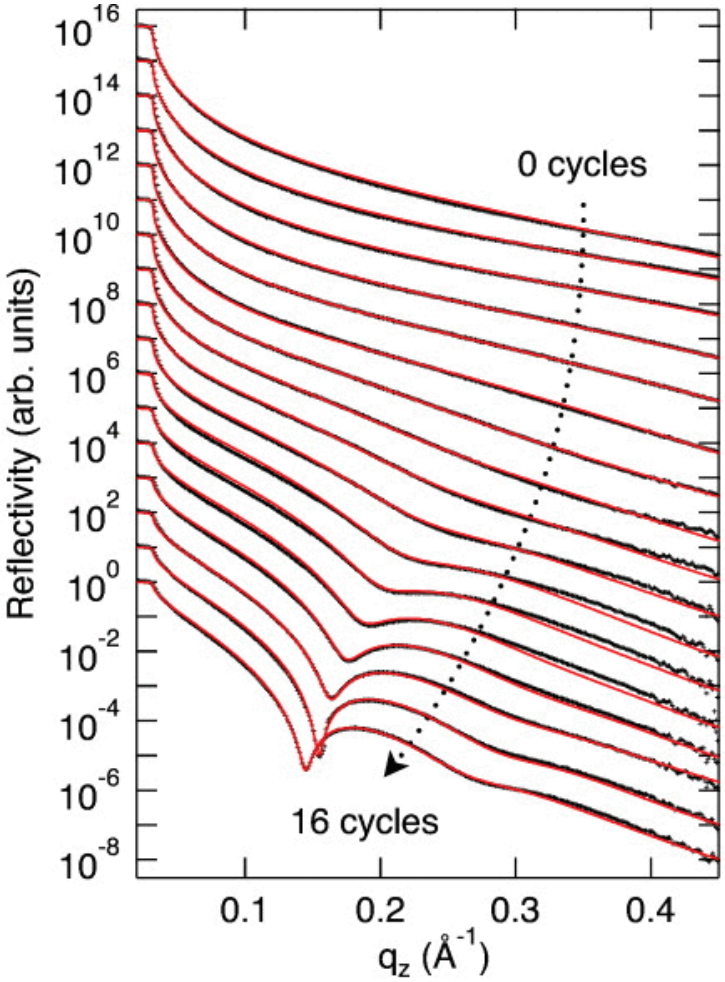

Figure 13: In situ XRR data collected during ALD growth of a ZnO thin film. Reused with permission from AIP Publishing LLC.[108]

XRD is one of the most widespread characterization tools to study atomic arrangements in solid samples. It differs from XRR in that it does not look at reflection from interfaces, but constructively interfering waves scattered events from planes in the crystal lattice itself. Discussion of the mathematical formalism behind x-ray crystallography is left to the literature, but it is important to understand the results of this formalism.

When the path length of incident and scattered waves differ by a multiple of the wavelength, the waves add up in phase and result in constructive interference. For scattering in a crystal, this means that the extra path length the wave travels between two lattice planes is proportional to the distance between the planes and the incident and diffracted angle of the x-ray wave. This can be summarized simply by Bragg's law:

$$n\lambda = 2dsin\theta \qquad \textbf{Eq. 10}$$

where λ is the wavelength, θ is the incident angle and d is the plane distance. By varying the incident angle of x-ray light on a crystal, and recording the intensity of the scattered light, planes in the crystal structure can be identified. Depending on the crystal lattice, the intensity of the scattering can be determined by the *structure factor*:

$$F_{hkl} = \sum_{i=1}^{N} f_i e^{2\pi i(hu_i + kv_i + lw_i)} \qquad \textbf{Eq. 11}$$

which uses symmetry arguments set forth by the atomic positions (u,v,w) and the Miller indices of the lattice planes *(hkl)* to describe the scattering from the crystal. The intensity of the diffracted wave is taken as the square of the structure factor. By using collected data and the structure factor in reverse, a lattice and its atomic positions can be uniquely identified.

In addition to the peak position in a diffractogram, corresponding to the incident angle of the x-rays, information can be gathered from the *shape* of the peaks coming from the scattered intensity. Features such as crystal strain, particle size and shape, disorder, mosaicity and concentration gradients affect the shape of the intensities, typically by *broadening*. The *broadening* may in other words be used to derivate properties of the samples at hand.

The above results are general and apply to all crystalline systems. Diffraction from thin films follow the same rules, but some limitations and constrains applies that are not found for bulk single crystals or powders. Studying powders in a thin capillary will for example allow for transmission geometry, where

the x-ray beam travels through the sample. This is very rare for thin films, which are typically deposited on substrates that are too thick to allow transmission. In this case, reflection geometry (θ-2θ) is used, where the sum of the incident and outgoing angle forms the scattering angle.

Reflection geometry constrains the part of the reciprocal space that can be reached by diffraction, as the sample cannot be rotated freely around all axes. For a polycrystalline sample, this will usually be unproblematic, as the crystallites are randomly arranged in all directions and will scatter the incoming x-rays as a powder sample. The random orientation of planes in a powder leads to formation of scattered *rings* in reciprocal space, where the radius of the ring corresponds to plane distances in the sample. By coupling the source and detector arm angles, performing a *symmetric* scan, a slice through these rings in reciprocal space is measured and the respective plane distances can be identified.

Very thin films often have very low scattered intensity, making it hard to identify reflections from the sample. This can be overcome by locking the x-ray source to a low incident angle, and only scanning the detector arm. This makes the path length of the x-rays in the sample longer, increasing the scattered intensity, as well as decreasing the scattering from the substrate. This type of geometry is called grazing incidence (GIXRD), and is routinely applied to thin polycrystalline films without any preferred orientation.

Oriented or single crystalline films provide a different challenge. The scattering from a single crystal does not come about as rings in reciprocal space, but as points. A symmetric scan will only slice through points along the surface normal, corresponding to scattering from planes that are parallel to the sample surface. This does indeed lead to information about orientation perpendicular to the surface, and may be used to identify the crystal structure of the film, but does not yield any information about the orientation *in plane*. This information can be obtained by tilting and rotating the sample to slice through a part of the reciprocal space in which *asymmetric* reflections are found. This is often termed a *reciprocal space map*, and by investigating the position and broadening of these peaks, a proper determination of the epitaxial relationship between the thin film and the substrate can be carried out. A *phi*-scan, rotating the sample 360° around an asymmetric peak can also be performed to confirm the epitaxial relationship.

Figure 14 shows the various types of important data that can be obtained by the different modes of x-ray diffraction measurements, exemplified by the $LiNbO_3$-system. A more rigorous and detailed explanation of the geometry and measurement modes of x-ray diffraction that have been utilized in this work can be found in supporting paper 2.[109]

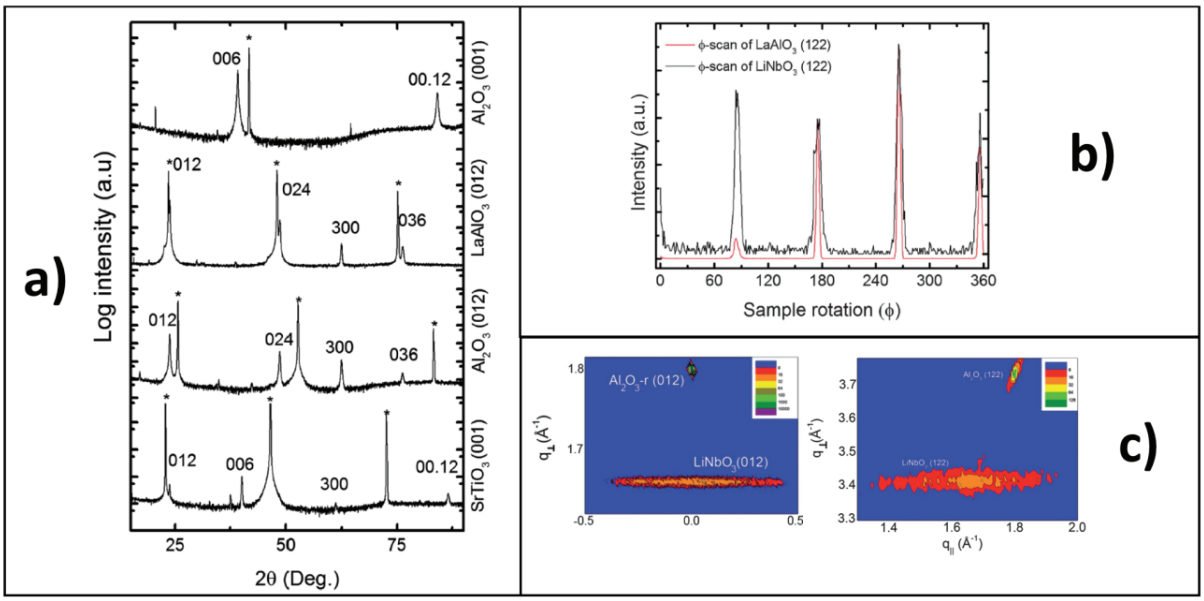

Figure 14, a): Traditional symmetric θ-2θ-scan of $LiNbO_3$ thin films on a range of substrates. This shows how an epitaxial film can have different orientation on different substrates. b) A *phi*-scan of an asymmetric reflection showing the four-fold rotational symmetry of this plane. c) Reciprocal space maps of two $LiNbO_3$ reflections (one symmetric and one asymmetric), showing how the film orientation is related to the substrate.

X-ray Absorption Techniques

Atoms can absorb electromagnetic radiation in a variety of ways, depending on the energy of the radiation. This has been used to construct a broad range of characterization techniques utilizing absorption of light, such as IR-spectroscopy, UV-VIS-spectroscopy and microwave rotational spectroscopy to name a few.

X-rays have energies that correspond well with electron binding energies in solid systems. If the x-ray energy is higher than the ionization potential of an electron, excitation to vacuum may occur and the atom is ionized. Such an event will lead to an unfilled electron position in the atom, immediately causing de-excitation of an electron of higher energy. The excess energy of the de-excited energy must be distributed somewhere, often in the form of a photon.

Two techniques that have been important in this work both use x-rays to ionize the sample, but are different in terms of what is detected.

X-ray photoelectron spectroscopy (XPS) directly measures the number and kinetic energy of the electrons that are ejected from the sample. A monochromatic x-ray source (typically Al K_α, E = 1486.7

eV) is directed onto the sample surface. This causes ejection of electrons from the top-most layer of the sample. Note that this constrains XPS to being a surface sensitive technique, as the mean free path length of electrons in a solid sample is limited to a nanometre length scale. An energy dispersive detector is scanned over discrete energies, and records the number of electrons with these discrete energies. The concentration of an atom in a specific chemical state is proportional to the relative intensity of ejected electrons at unique binding energies. The binding energy of the electrons is found by:

$$E_{binding} = E_{photon} - (E_{kinetic} + \Phi) \qquad \textbf{Eq. 12}$$

where Φ is the work function determined by the sample and instrument. By using known photon energy and measuring the kinetic energy of the electrons, the binding energy can be determined.

The binding energy is not only unique for every element, but also unique to different oxidation states and binding states of the atoms. This means that XPS can be used not only to determine the relative composition of elements in a sample in the top 10 nm, but also to qualitatively describe chemical and electronic states in the system. By using ion etching, it is also possible to obtain depth profiles, but extra care needs to be taken when doing this, as many samples are prone to change upon ion etching. Also, note that ion etching cause changes in chemical state, so information about bonding is always lost after etching. XPS is in theory sensitive to all elements. In practice, however, laboratory instruments cannot detect hydrogen and helium, and is limited to lithium or heavier elements.

X-ray fluorescence (XRF) does not detect the ejected electrons themselves, but rather the photons that are emitted upon de-excitation of an electron from a higher energy level when a core electron is excited. X-rays travels much easier through solid samples, thus XRF can be used also for bulk samples. XRF is theoretically limited to elements with electrons in two shells ($Z \geq$ Li), but due to low fluorescent yield for elements in the second period, most laboratory instruments are not sensitive to second period elements.

Composition is determined by collection of the x-rays over a broad range of energies corresponding to unique de-excitation energies for the different elements. The relative concentration of an element is proportional to the emitted intensity of its unique spectral line. Care must be taken to avoid overlapping spectral energies if the sample consist of elements where this may be a challenge.

XPS and XRF have been routinely used throughout this work to study the composition and chemical state of thin films. The techniques have often been used in conjunction to confirm data from each source, or to study difference in top layer *versus* bulk composition.

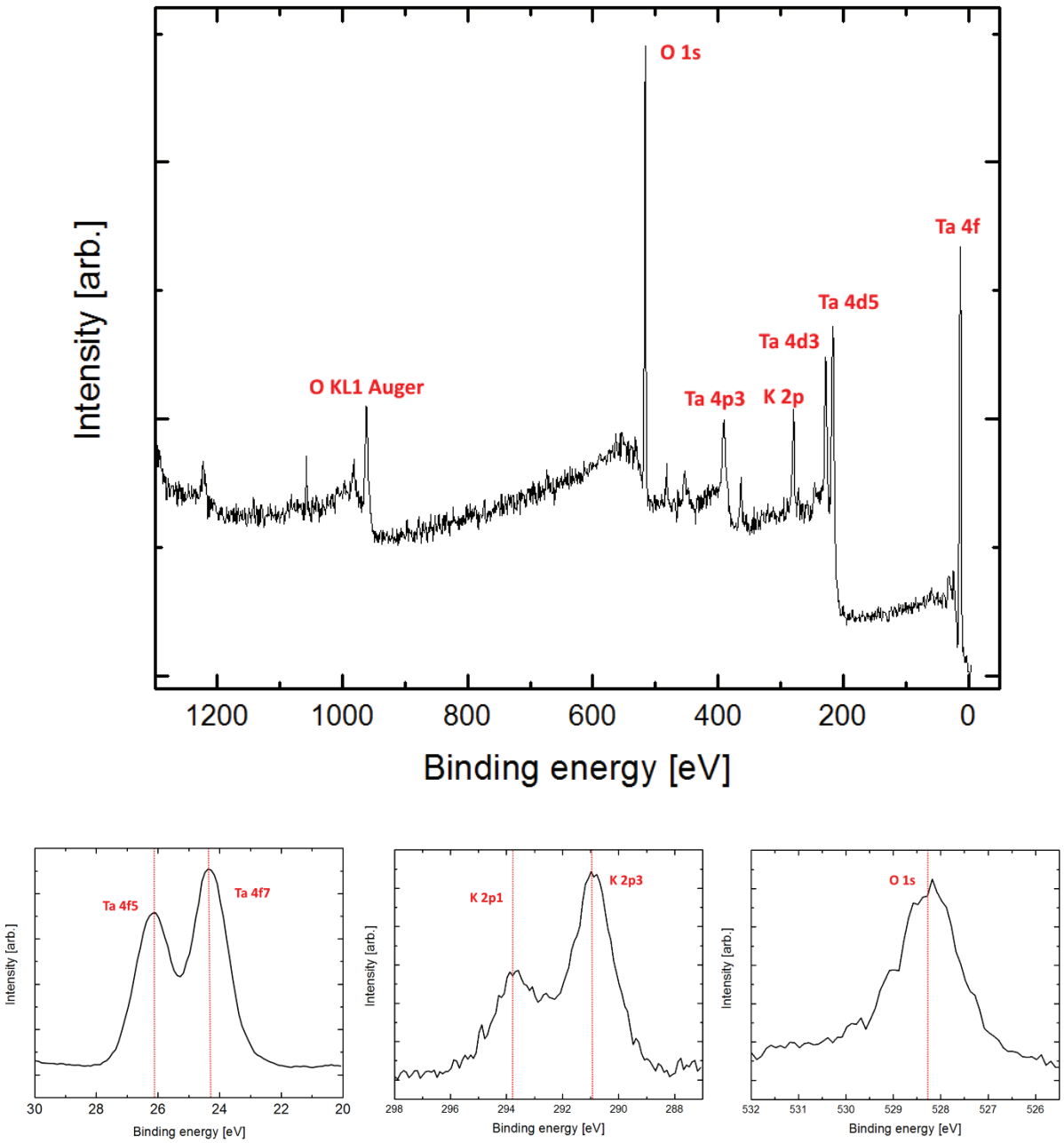

Figure 15: Example data that can be collected by XPS, exemplified by a $KTaO_3$ thin film sample. The survey spectrum (top) gives an indication on what elements are present in the sample, whereas the high resolution single peaks can be used to obtain chemical and stoichiometric information.

Atomic Force Microscopy

An important feature of any thin film system is the surface morphology and topography, both for the underlying substrate and for the thin film itself. The shape of the substrate is a key factor for controlling the structure of the thin film that is grown on top. The shape and surface area of the thin film itself have direct impact on the activity of the sample.

Atomic force microscopy (AFM) is a method for direct imaging of surface topography of solid samples. It was invented by IBM physicists Binnig, Quate and Gerber as a complimentary technique to the *scanning tunnelling microscope* (STM).[110] While STM is limited to conducting samples through electron tunnelling between a tip and the surface, AFM has no such constraints. The sample is placed on a table controlled by piezoelectric actuators that move it parallel to the sample surface with sub-micrometre precision. A cantilever with a nanometre size tip mounted on it is lowered onto the sample, with z-control on the sub-nanometre level. A laser beam is pointed towards the top of the cantilever where it is reflected towards a detector. The sample is now scanned in x- and y-direction, and the tip follows the topography of the sample surface. When the cantilever moves in response to the sample surface contours, the laser spot moves on the detector and this is recorded and used to reconstruct an image of the surface.

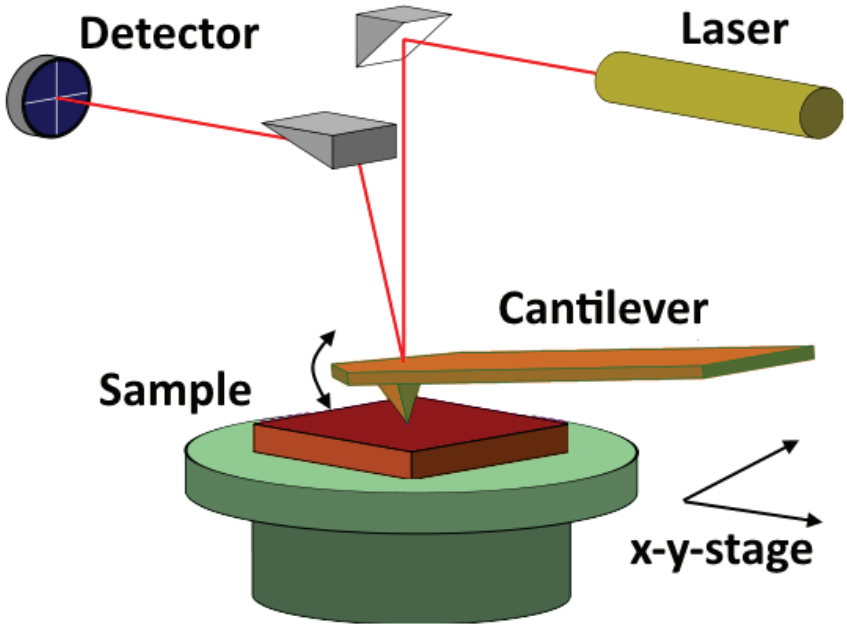

Figure 16: Schematic of an AFM instrument showing the how a laser beam is deflected off a cantilever that traces the sample, and subsequently hits a photodetector. Adapted version of AFM schematic created by GregorioW and distributed via Wikimedia Commons.

Different modes of recording and scanning the tip exist. Flat, hard samples are often imaged by direct contact between the tip and the sample, termed *contact* mode. Here, the tip is "dragged" across the surface and the surface morphology is imaged by recording the deflection of the cantilever. The lifetime of the tip is often short when applying contact mode, and softer samples can be damaged. To conserve the tip and make sure the surface is not altered, the tip is often set to vibrate with a constant amplitude and oscillation just below or at its resonance frequency. When the tip is scanned over the sample surface, the amplitude changes and its value is fed back to tip motor which in turn drives it back to the set amplitude. This indirectly measures the tip-to-sample forces in play, and is used to reconstruct the sample surface. Note that changes in sample hardness and polarity will affect this interplay, making it possible to map domains in the sample. This mode is termed *tapping*, and causes less damage to the tip and surface compared to true contact AFM while maintaining the quality of the imaging. Softer samples, such as hybrid materials, may be damaged by tapping as well. This calls for use of *true non-contact* mode, where the cantilever is set to vibrate at its resonant frequency or just above. When the tip gets close to the surface (1 – 10 nm away), van der Waals forces come into play and decrease the resonant frequency of the cantilever. This change is fed back into the system and the average distance from the tip to the surface is shifted to get back to the set resonance frequency. The z-value is recorded, and the surface morphology can be reconstructed.

Choosing what AFM mode to use for a specific sample is important, as the best imaging is achieved with the hard modes if the samples are not altered by the forces involved. It is harder to obtain a good image with non-contact mode, but using this one can make sure that the sample surface is not changed. Tapping mode is typically a good trade-off between the two, and has become the most used mode in later years. If not otherwise specified, all AFM-images presented in this thesis have been recorded in tapping mode.

Piezoelectric Force Microscopy

By altering the standard AFM imaging technique, other parameters can be imaged indirectly. This includes imaging of magnetically and electrically active domains. One such alteration, important for electrically active thin films such as in this thesis, is applying a bias over the tip to study piezo- and ferroelectric activity. This is called *piezoelectric force microscopy* (PFM).

This technique was pioneered by Güthner and Dransfeld in 1992, and has become a standard technique to map piezoelectric domains.[111] PFM makes use of the *converse piezoelectric effect*, in which an applied electric field will result in a change in the lattice parameters of a piezoelectric material through strain.

Mathematically, the coupling can be described via the piezoelectric tensor, d_{ki}, which is unique to the different crystal systems. As an example, the coupling in the common piezoelectric tetragonal space group (*P4mm*) is given as:

$$\begin{bmatrix} S_1 \\ S_2 \\ S_3 \\ S_4 \\ S_5 \\ S_6 \end{bmatrix} = \begin{bmatrix} 0 & 0 & d_{31} \\ 0 & 0 & d_{32} \\ 0 & 0 & d_{33} \\ 0 & d_{24} & 0 \\ d_{15} & 0 & 0 \\ 0 & 0 & 0 \end{bmatrix} \begin{bmatrix} E_x \\ E_y \\ E_z \end{bmatrix} \qquad \textbf{Eq. 13}$$

where S_i is the strain tensor, d_{ki} is the piezoelectric tensor and E_k is the electric field in direction k.

In PFM, a sharp conductive probe is lowered onto the sample surface in the same manner as for traditional AFM. By applying an electric field through an alternating current bias to the tip, a piezoelectric material will be deformed as a result of the converse piezoelectric effect. The field is only applied in one direction (z), which will result in three strain components: $d_{31}E_z$, $d_{32}E_z$ and $d_{33}E_z$. The strain causes deformation that will deflect or attract the cantilever, and this is subsequently recorded as a morphology change at the detector. Typically, a high frequency AC-bias is applied for fast scanning, and the signal must be demodulated by a lock-in amplifier on the detector side.

In theory, the change in lattice parameter can be quantified and used to find the elements of the piezoelectric tensor. This requires samples with a known number of unit cells out-of-plane, and is not feasible for thin films with the thicknesses investigated in this thesis.

More directly, however, PFM makes it possible to image piezo- and ferroelectric domains in the sample, generating information about domain size and morphology, which are important parameters considering the performance of a piezo- or ferroelectric. The technique has been used throughout this thesis to investigate piezoelectric activity and domain shape. An example of a typical map is shown in Figure 17.

Also notable is the possibility to use a magnetized tip to record magnetic domain structures in the sample. This is termed *magnetic force microscopy* (MFM), but has not been utilized in this work as the samples do not exhibit any interesting magnetic phenomena.

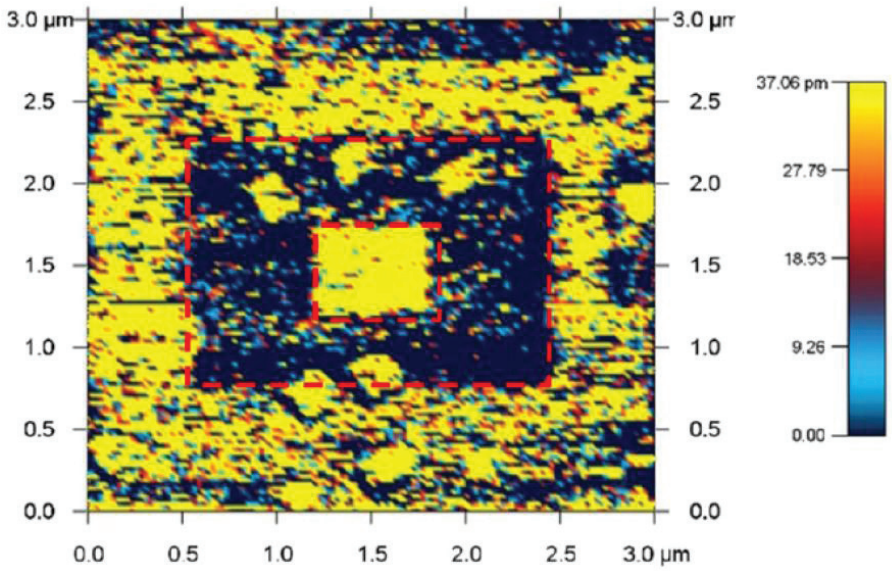

Figure 17: PFM amplitude contrast image of an ALD $BiFeO_3$ thin film on a Nb:$SrTiO_3$-substrate exhibiting patterned domains following successive writing of two square shaped regions. Reused with permission from the American Chemical Society.[103]

Other Techniques

A range of other characterization techniques have been used to a lesser degree or by a third-party, and will not be introduced in detail. A review paper discussing the technique and its use in thin film characterization is listed for all techniques.

- **Spectroscopic Ellipsometry:**[112] Measures change of polarization upon reflection from a thin film and its substrate. Used for determination of thin film thickness and refractive index. Films are considered transparent for the wavelengths used in this work, enabling use of simpler characterisation models such as the Cauchy function. The transparency approximation can be applied without concerns for all thin films in this work.

- **Time-of-flight Elastic Recoil Detection Analysis (TOF-ERDA):**[113] A directed ion beam bombards the surface and is scattered due to an elastic nuclear interaction between the probing ions and the atoms of the sample. The sample ions recoil towards a detector that collects and measures the relative concentration in the sample. The recoil of sample atoms from the surface causes ion etching, so TOF-ERDA will automatically give a high resolution depth profile. The

technique is sensitive to all elements, including hydrogen. In this work it was used to study lithium content and distribution in the films. Carbon and hydrogen sensitivity also allowed depth profiling of unwanted contamination. TOF-ERDA measurements in this thesis were performed by Timo Sajavaara at the University of Jyväskylä.

- **Thermogravimetric Analysis (TGA):**[114] A small amount of a powder sample is placed in a crucible. The sample is heated while continuously measuring the mass of the sample in the crucible. The mass will decrease upon vaporization or gaseous decomposition of the sample. This has been used to study the thermal properties of the possible precursors in ALD-systems.

- **Fourier Transform Infrared Spectroscopy (FT-IR):**[115] Infrared light has energy that corresponds to molecular vibrations through stretching, rocking or twisting of covalent bonds. These vibrations have discrete energies that are unique for different kinds of bonds. In infrared spectroscopy the absorption of infrared light over a broad spectrum is measured. Absorption at different energies can be attributed to existence of certain types of bonding in the material, such as O-H-bonds, C-O bonds or C=O-bonds. In this work, this has been used to identify possible contaminants, especially in the form of carbonates in the sodium- and potassium aluminate samples.

- **Transmission Electron Microscopy (TEM):**[116] Transmission electron microscopy uses the wave-properties of electrons to image electron density in the sample. An electron beam is focused onto a thin slice of a sample where it interacts and is collected on a detector on the other side, directly imaging the sample. The short wavelength of high energy electrons allows imaging on the angstrom level, meaning that it is possible to image single rows of atoms and their arrangement in a solid sample. Some of the electrons will inelastically scatter form the sample, losing energy in the process. The energy loss can be recorded and used to identify elements in the sample, which has given rise to the electron energy loss spectroscopy (EELS) technique. Variations of TEM exist, most notably the scanning TEM (STEM) where the focusing takes place before the electron beam hits the sample, and the beam is raster scanned to provide a full image. TEM and subsidiary techniques are crucial tools in thin film- and interface studies, as it allows direct imaging of the epitaxial relationship between a thin film and its substrate. TEM has been used to investigate interface structure in selected thin film-substrate systems in this work. TEM imaging was performed by the Structure Physics group at the University of Oslo.

5. Atomic Layer Deposition of $A^{+}B^{5+}O_3$ Perovskite-like Thin Films

In this, the central chapter of the thesis, results dealing with the most important findings of the work are discussed in a holistic manner. Experimental details and minor results are therefore mostly left to the selected papers. The results are presented chronologically, starting with the deposition of $LiNbO_3$ as the first epitaxial alkali metal complex oxide deposited by ALD. This was summarized and published in main paper 1. The second part deals with finding working precursors for the deposition of sodium- and potassium containing thin films. The work was based upon results from work with lithium precursors, and lead to the first ever reports of Na- and K-processes for ALD. This was summarized and published in main paper 2. The third, final and quintessential part of this chapter summarizes the work done on sodium- and potassium niobates and tantalates. Deposition of the four corner-systems ($NaNbO_3$, $KNbO_3$, $NaTaO_3$ and $KTaO_3$) and of the two important solid solutions ($K_xNa_{1-x}NbO_3$ and $KTa_xNb_{1-x}O_3$) is presented in detail, based on the summarized and published results in main paper 3.

Atomic Layer Deposition of $LiNbO_3$

ALD of lithium containing thin films was pioneered by Putkonen *et al.* in the 2009 paper introducing two working precursors (Li(thd) and LiO^tBu).[104] One of the concerns raised here is the monovalency of the alkali ions, challenging the conventional way of thinking self-limited growth mechanisms in ALD. Experimental results do, however, point towards self-limitation. This received notable attention, and in the following years, processes for deposition of *e.g.* lithium titanate, lithium aluminate, lithium manganite and lithium tantalate were reported.[117-120] Other precursors were also investigated, among these *lithium silylamide* ($LiN(SiMe_3)_2$), which exhibit excellent growth for lithium carbonate, lithium silicate and lithium nitride to name a few. All the systems currently mentioned had a common denominator in that they were primarily focused on applications in *battery technology*, where orientation of growth and crystal quality is not necessarily as crucial as for complex oxides with properties originating solely from structural relation.

As a result of this, four major challenges were identified for the growth of $LiNbO_3$:

- Precursor compatibility with well-known niobium precursors
- Control of lithium loss upon heat treatment
- Control of carbon contamination, possibly detrimental to electric properties

- Control of growth orientation and epitaxy

Growth of niobium oxide was reported by Kukli *et al.* back in 1998.[121] $Nb(OEt)_5$ was used as niobium source and reported to exhibit ALD-growth at temperatures between 150 and 350 °C, with water as the co-ractant. To limit the complexity of the mechanism, it was decided to use a Li-process that does not need introduction of ozone. In addition, Li-growth using Li(thd) and ozone is reported to result in what is believed to be detrimental amounts of carbon for some systems, especially at low temperatures.[122]

The two remaining viable precursors, LiO^tBu and $LiN(SiMe_3)_2$, could possibly both have been used. With prior knowledge of the silyl amide in the research group, it was decided to use this for the first investigation of $LiNbO_3$ growth. This precursor was also shown to exhibit self-limiting growth from 150 up to around 250 °C, which corresponds fairly well with the $Nb(OEt)_5/H_2O$ ALD-window. In an effort to limit the amount of carbon contamination a temperature in the upper regime of the window was chosen, and all films in the $LiNbO_3$-investigation were deposited at 235 °C.

The traditional way of depositing a ternary system is by investigating the binary systems and then combing them. The binary lithium oxide is not possible to deposit due to the air- and humidity sensitivity of the films after breaking vacuum. Because of this, principal investigation was carried out directly on the ternary system. Pulsing water-sensitive niobium ethoxide was also believed to limit the water reservoir effect that had been described for many lithium processes, possibly avoiding any misinterpretation of the lithium growth.

From previous use of the niobium and lithium precursors a 1 s pulse and purge duration for all precursors were deemed sufficient. The first investigation confirmed this, as controlled and gradient free films were obtained for a pulsed Nb:Li-ratio > 1. At the 1:1 limit severe non-uniformity was observed, and for higher lithium concentration powder-like films pointed towards uncontrolled growth. Figure 18 (left) shows the correlation between the pulsed ratio of Li:Nb and the resulting concentration in the film as measured by TOF-ERDA. This confirms that problems arise when approaching the 1:1 limit. Figure 18 (right) shows the depth profile of a film with 2:1 Nb:Li pulsing ratio. Three important characteristics are important to note:

1. Lithium tends to slightly migrate towards the surface of the films, but the net amount of Nb:Li incorporated in the films is relatively equal for this pulsed composition.
2. Carbon contamination in the film is very low, with amounts in the 0.1 % regime. Sodium contamination, most probably from the precursor, is around 2 %. The sodium contamination is thought to be relatively unproblematic in terms of electric performance.

3. The amount of silicon in the films is negligible, confirming that cleavage of the precursor during growth is at the Li-Si bond.

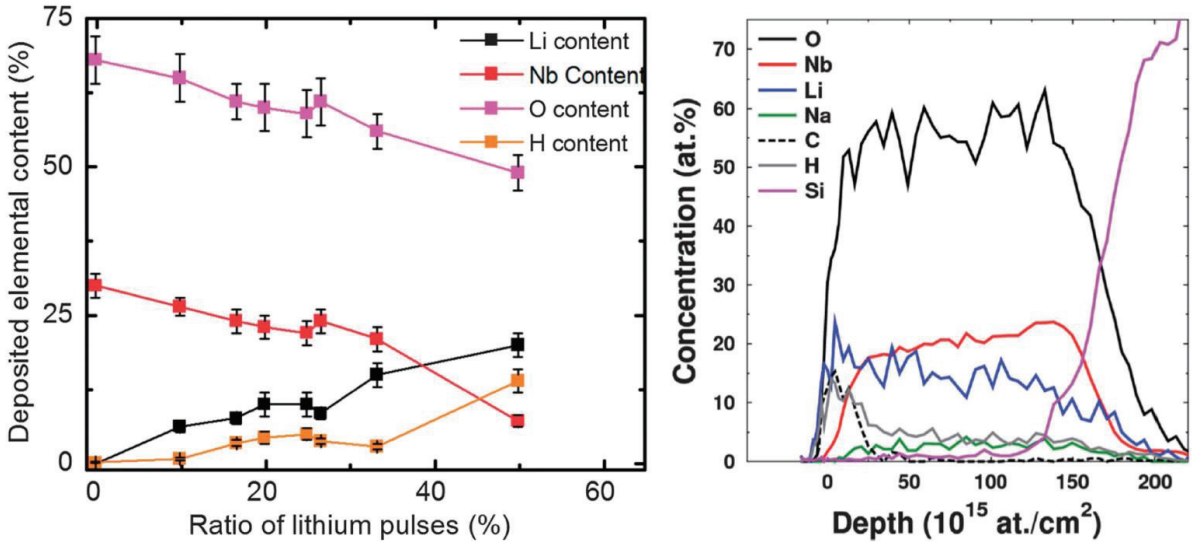

Figure 18, left: Correlation between the pulsed Li:Nb-ratio and the deposited elemental content as measured by TOF-ERDA. Right: TOF-ERDA depth profile of a $LiNbO_3$ thin film deposited with a 2:1 Nb:Li ratio.

As the net Nb:Li ratio was very close to 1:1 for the 2:1 pulsing ratio, this was used to deposit films for evaluation of piezo- and ferroelectric performance. The slight non-uniformity as a function of film depth was not considered a big problem as it was believed that post-deposition annealing and high mobility of the Li-ions would result in proper mixing.

The first diffraction experiments confirmed this assumption, as shown in Figure 19. At 2:1 pulsed ratio, films on Si(100)-substrates annealed at 650 °C for 10 minutes in oxygen atmosphere only show reflections from $LiNbO_3$, no signs of Nb_2O_5 as for the films with Nb:Li-pulsing ratio higher than 2. Also note the lack of any reflections from the 1:1 pulsed ratio system.

A thorough investigation of controlled orientation was performed, showing that different substrates could be used to achieve different orientations. Reciprocal space mapping and φ-scans were performed to show orientation both in and out of plane. As an example, $LiNbO_3$ on $LaAlO_3$(012) had a preferred (012)-orientation, whereas on Al_2O_3(001) a near perfect $Al_2O_3(001)|Al_2O_3[100]||LiNbO_3(001)|LiNbO_3[100]$ epitaxial relationship was seen. This control of orientation is important as *c*-axis orientation of the pseudo-cube normal to the film plane is necessary for out-of-plane piezo-response. Interesting is also the lack of preferred orientation on $SrTiO_3$(100)-substrates, which is believed to stem from lattice mismatch

on the (100)-plane. It is possible that different heat treatment would result in other results for some of the systems.

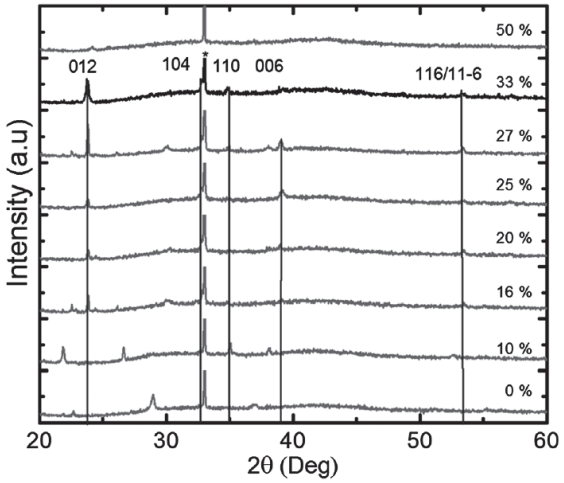

Figure 19: XRD patterns of Li-Nb-O thin films with different pulsed ratio after annealing at 650 °C. The %-value indicates the Li:(Li+Nb) ratio. Vertical lines indicate theoretical reflections of the rhombohedral $LiNbO_3$ phase.

Finally, investigation of the piezo- and ferroelectric properties of $LiNbO_3$ thin films on Si with silver contacts was performed. Piezoelectric force microscopy images show a 180° polar response domain regime, with complex domain structure. Silicon is not the ideal substrate for oriented growth, and the complex polar domain structure could be a result of this. However, even with some small domains exhibiting no polarity, most of the film is piezo-active upon perturbation from the PFM-tip.

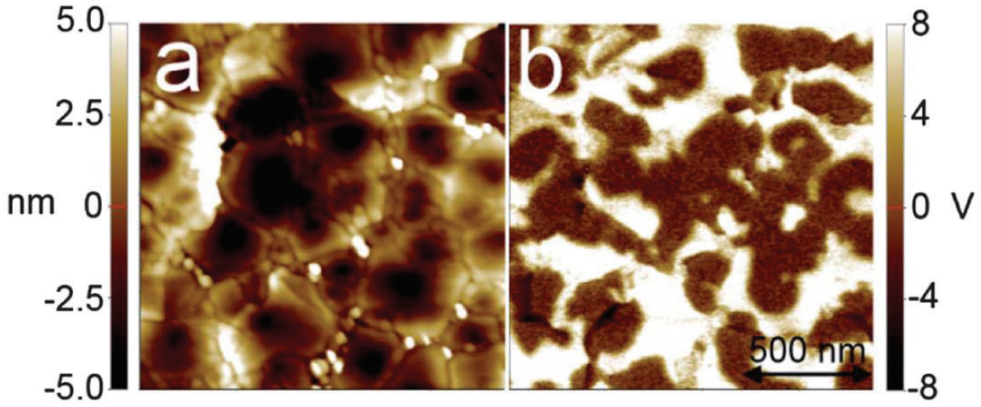

Figure 20, left: Tapping mode AFM image showing $LiNbO_3$-crystallites with some inclusions of smaller grains thought to be Nb_2O_5. Right: PFM image showing the pizeoelectric activity of the film. The piezoelectric domains have a complex shape, which may cause issues with domain wall pinning.

Ferroelectric activity was confirmed by measuring a coercive field of approximately 220 kV/cm (Figure 21), which is very consistent with experimental values from bulk $LiNbO_3$.[123] Also note that this is almost a factor two higher than previous reports of $LiNbO_3$ on Si-substrates. The high coercive field could be a feature of the complex domain structure, as the remanent polarization of ~0.4 $\mu C/cm^2$ is consistent with other reports of congruent $LiNbO_3$ thin films.

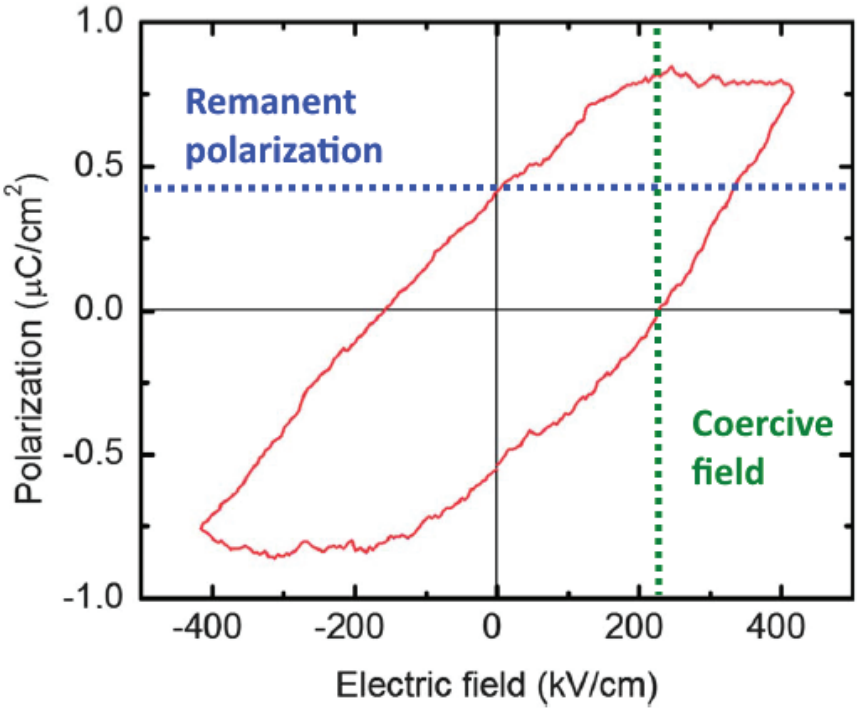

Figure 21: Polarization as a function of applied electric field, with a remanent polarization of ~0.4 $\mu C/cm^2$ and a coercive field of ~220 kV/cm.

This was the first report of $LiNbO_3$ thin films by ALD. It paved the way for more research, as it also proved that excellent crystallinity and controlled orientation is possible for complex alkali oxides by ALD. To be viable for replacing PZT in all applications, however, a high degree of tailoring the electric activity is needed. This is not feasible for $LiNbO_3$, but is possible for the related $K_xNa_{1-x}NbO_3$ (KNN). With the alkali niobate ALD mechanism proof-of-concept for$LiNbO_3$, depositing KNN was thought to be possible. To achieve this, however, a venture into Na- and K-containing thin films by ALD had to be carried out.

Atomic Layer Deposition of Na- and K-containing thin films

When the work with this thesis started, no reports of processes for Na- or K-containing thin films existed. This was somewhat a "hole" in the periodic table of ALD, as most other non-radioactive metals had seen deposition routes for either the pure metal or for oxides.[102] The absence of routes for other alkali metals than lithium can probably be attributed to two factors; *difficulty* and *lack of interest*, or perhaps a combination of the two. Sodium compounds have received new interest as a result of trying to find novel battery systems, as these can be used to make new and inexpensive alternatives to lithium batteries. Sodium is also found in some thermoelectric and superconductive materials, but these are fields where ALD is not typically applied. Potassium compounds of interest for functional materials are scarce, with a few exceptions for piezo- and ferroelectric materials, such as $KNbO_3$.

Equipped with the experience from complex oxide lithium compounds with ALD, the search for viable precursors naturally began with the known and tested lithium precursor ligands. Many precursors were preliminarily screened, including *β*-diketonates, *tert*-butoxides, silylamides and silanolates. As the goal was to find a *water-only* reaction pathway to be combined with niobium growth, the *β*-diketonates were abandoned after initial screening. Three types of precursors (Figure 22) were believed to be suitable, and were tested for thermal properties through thermogravimetric analysis (TGA). This analysis showed promising results for all sodium variants, but only the *tert*-butoxide for potassium (Figure 23). Potasssium trimethyl silanolate (KTMSO) and potassium hexamethyl disilazane (KHMDS) decomposed in several steps, and do not evaporate as a molecule. This can probably be attributed to the more ionic type bonding in KTMSO and KHMDS in comparison to the more covalent character of NaHMDS and NaTMSO.

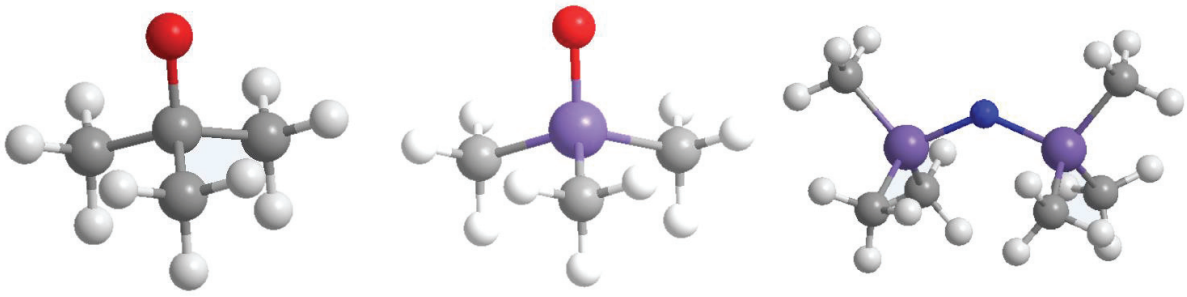

Figure 22: Structure of the organic ligand for AO^{t}Bu (left), ATMSO (center) and AHMDS (right). Carbon atoms are coloured grey, oxygen atoms are red, silicon atoms are purple and nitrogen atoms are blue.

NaHMDS also seemed to have a strange linear loss of mass up to 225 °C, and was not deemed ideal as an ALD precursor. It was tested in the reactor with both water and ozone as oxidizing agents, both for deposition of Na_2CO_3 but did not give reproducible results. At this stage both silylamides had to be abandoned, which was surprising given that this was the ligand of choice for deposition of $LiNbO_3$.

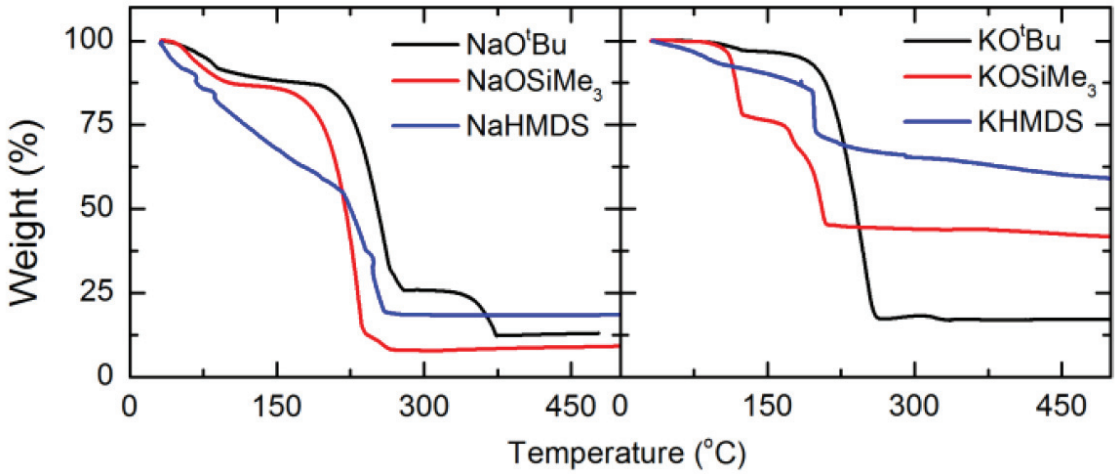

Figure 23: Thermogravimetric analysis of the six precursors that were believed to facilitate self-limiting growth at typical ALD-temperatures.

The precursor screening process resulted in three viable precursors, two for sodium and one for potassium. The TMSO-type ligand was previously unexplored, and was investigated using both ozone and water as oxidizing agents. The initial thought was that using ozone would lead to sodium silicate growth, whereas water combined with a second metal subcycle would lead to deposition of sodium metalates. Thin films grown with either of the two oxidants produced relatively large gradients in both thickness and refractive index over a large span of temperatures and pulse lengths. Gradients were not instrument specific, as they were reproduced in two reactors with different geometry. Investigation of composition over the gradient showed that the differences of thickness and refractive index most likely were a result of varying silicon inclusion along the flow direction. Post-annealing x-ray analysis showed signs of sodium silicate in films deposited with both water and ozone. Even though deposition of NaTMSO could possibly be used to deposit controlled layers of sodium silicate after more stringent fine-tuning, it was abandoned as silicon contamination cannot be accepted in the tantalate and niobate films.

The toolbox of sodium- and potassium precursors were now reduced to only two compounds; the *tert*-butoxides. Given the TG-analysis and former success of deposition of lithium compounds using lithium *tert*-butoxide, there were high hopes for these precursors. Due to the air-sensitivity of a theoretical sodium- or potassium oxide film, both systems were investigated together with the TMA + water process, thereby depositing *aluminates*.

Initial deposition using sodium *tert*-butoxide was performed at 250 °C with 0.5 and 0.15 second pulses of the sodium precursor. A 1:1 pulsed ratio between sodium and aluminium with 200 super cycles were used to investigate the working temperature of the precursor. Surface saturation was reached at a precursor temperature of 140 °C under these conditions. At lower temperatures, severe thickness gradients and an increase in refractive index was observed (Figure 24). As a result of this, all subsequent depositions with sodium *tert*-butoxide were carried out using a precursor temperature of 140 °C.

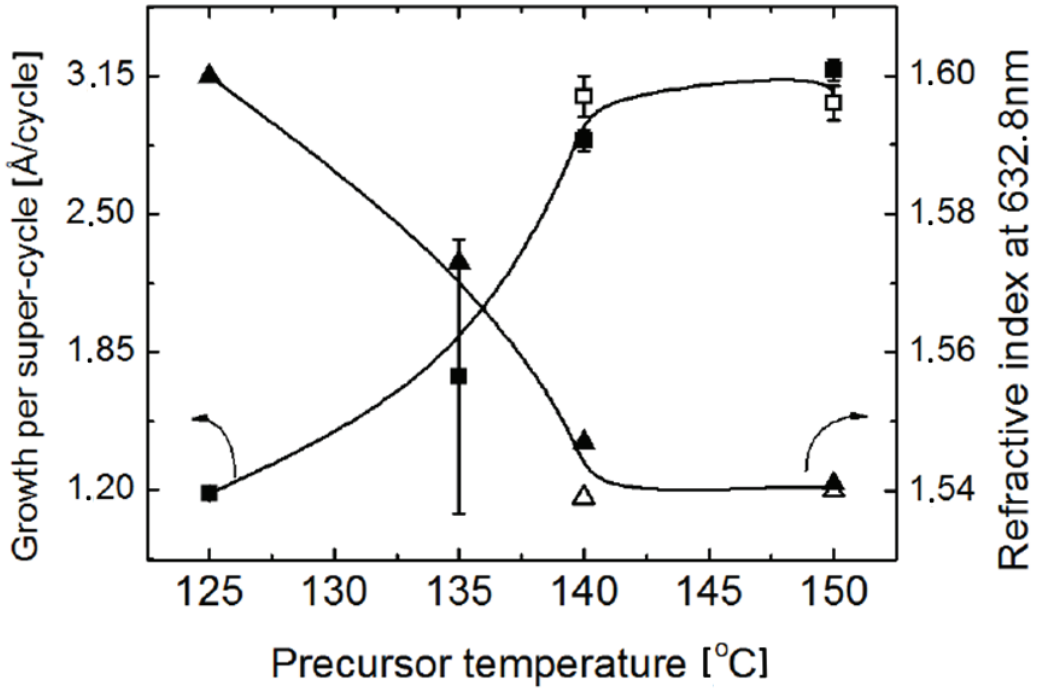

Figure 24: Growth per supercycle and refractive index as a function of the precursor temperature. The reactor temperature was maintained at 250 °C for all these depositions.

To identify an ALD-window for the process, depositions were performed in the 225 to 375 °C temperature range (Figure 25). A traditional ALD-window was difficult to determine, but a relatively constant GPC, Na:Al-ratio and refractive index was found for temperatures between 250 and 300 °C.

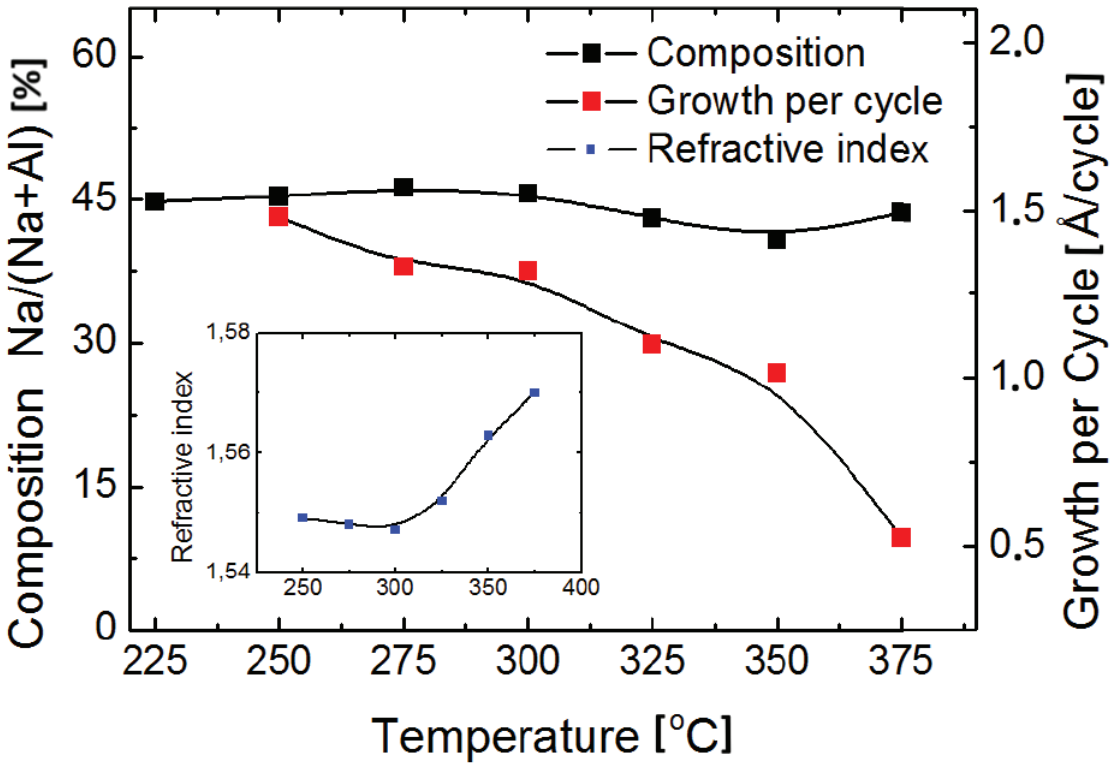

Figure 25: Growth per cycle and sodium composition as a function of the reactor temperature. The sodium content is relatively constant over the whole temperature regime, but the growth decreases rapidly at temperatures above 300 °C. Inset: Refractive index as a function of reactor temperature.

It was concluded that sodium *tert*-butoxide is a favourable precursor for ALD of sodium containing thin films, with a working temperature range from 250 to 300 °C, a precursor temperature of 140 °C and down to 0.15 s pulse duration in the reactor used. The working temperature range overlaps sufficiently with that of the niobium- and tantalum ethoxides, and low pulse duration facilitates relatively fast film growth. Investigation of composition also showed low carbon contamination for the $NaO^tBu + H_2O + TMA + H_2O$ process, making it ideal for use in deposition of thin films with functional electric properties.

The *potassium tert*-butoxide exhibits very similar temperature stability as its sodium counterpart. It was found, however, that a slightly higher precursor temperature (170 °C) and longer pulse duration (0.5 s minimum) had to be applied to achieve saturated growth. In addition, a 1:1 pulsing ratio for K:Al resulted in films with high gradients because of a high potassium surplus. To overcome this, a 1:4 pulsed ratio was applied for initial tests. With these parameters, growth of potassium aluminium oxide was very similar to that of sodium aluminium oxide. GPC and K:Al-ratio have a plateau between 250 and 300 °C (Figure 26).

At these temperatures the gradient over an 8" silicon wafer was as low as ~1%. Low carbon contamination was also found for the $KO^tBu + H_2O + TMA + H_2O$ process, and the composition could be tuned to about 30 % potassium. At higher potassium concentration severe gradients were seen, and this was attributed to formation of surplus KOH that reacts with air after breaking of vacuum or through reservoir effects. This was not considered a problem in the formation of niobates or tantalates, in which 1:1 potassium to metal is easier to achieve than in the aluminium oxide matrix.

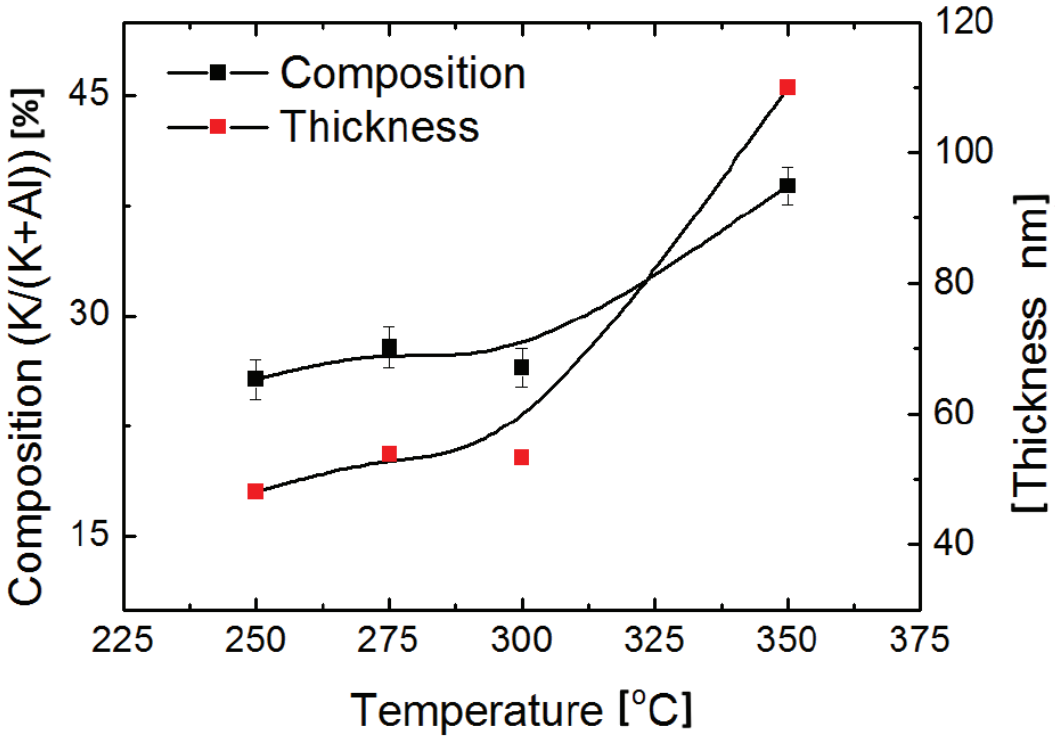

Figure 26: Film thickness and composition as a function of reactor temperature. The growth and composition is relatively constant in the same temperature regime as for the sodium counterpart. At higher temperatures, however, the growth rate and potassium content increases dramatically.

In conclusion, out of the screened precursors only sodium and potassium *tert*-butoxide were deemed to be viable precursors for deposition of complex oxides. They can be used to deposit conformal films in a very compatible temperature regime, and it is possible to easily tune the composition by changing the pulsed precursor ratios. Growth is achieved with water as the oxygen reactant, and relatively fast growth parameters can be used.

Atomic Layer Deposition of $(K_xNa_{1-x})(Nb_yTa_{1-y})O_3$

With the discovery of precursors for ALD of sodium and potassium containing compounds, and existing routes for niobium and tantalum oxides, realization of the $(K_xNa_{1-x})(Nb_yTa_{1-y})O_3$, $0 \leq x,y \leq 1$ was thought to be feasible. Bear in mind that the ultimate goal was stoichiometric control of the ferroelectric solid solution $K_xNa_{1-x}NbO_3$, and that the congruent corner-systems and the solid solution $KNb_yTa_{1-y}O_3$ is studied in parallel as they have interesting inherent properties of their own.

The first step in depositing a quaternary system is to control the ternary processes and then combining them. In the KNNT-system this means that four ternary systems; $NaNbO_3$, $NaTaO_3$, $KNbO_3$ and $KTaO_3$ had to be investigated first. K, Na and Nb processes had all been utilized in the earlier stages of this work, whereas deposition of Ta_2O_5 using $Ta(OEt)_5$ was reported in 1999.[124] The tantalum ethoxide + water system is very similar to the niobium ethoxide + water system, both in regards to growth rate and temperature stability. To minimize the number of variables, all depositions that are presented here are carried out with many coinciding parameters, which are presented in the table below (Table 1).

Table 1

Parameter	Abb.	Value
Reaction chamber temperature	T_R	250 °C
NaO^tBu source temperature	T_{Na}	140 °C
KO^tBu source temperature	T_K	150 °C
$Nb(O\text{-}Et)_5$ source temperature	T_{Nb}	68 °C
$Ta(O\text{-}Et)_5$ source temperature	T_{Ta}	70 °C
Working pressure	P	3 mbar
Water pulse duration	t_{H2O}	250 ms
$(Na/K)O^tBu$ pulse duration	$t_{Na/K}$	3000 ms
$(Nb/Ta)(O\text{-}Et)_5$ pulse duration	$t_{Nb/Ta}$	2000 ms
Purge duration	t_p	1000 ms
Substrate	-	Si (100)

T_R was chosen to be in the working area of all precursors, and had shown to be a temperature that facilitated self-limiting growth of all precursors. The potassium bubbler temperature had to be decreased

with 20 °C compared to what was reported in main paper 2, to avoid gradients. This may have slightly affected the amount of K that is incorporated in the film per pulse, as a lower potassium inclusion rate is seen in this system. The pulse durations also had to be increased compared to deposition of the binary compounds, which is a common feature when increasing the complexity of the deposited system.

The four corner-systems exhibit remarkably similar growth characteristics (Figure 27). This is of course expected and due to the similarity of the precursors and metal ions incorporated in the film. Note, for example, that the ionic radii of Nb^{5+} and Ta^{5+} are almost identical (both reported as 0.64 Å in 6-fold coordination). All deposited films in the Na/K:Nb/Ta < 1 pulsed ratio regime were nearly gradient free (less than 5 % thickness and/or refractive index difference over the chamber), and they were all x-ray amorphous as deposited on silicon. They were atomically flat (roughness average less than 0.5 nm as measured by AFM). An effort was made to increase the pulsed sodium or potassium ratio, but this resulted in large gradients after breaking vacuum. This is most probably again a result of a reservoir effect causing post-deposition reactions with air.

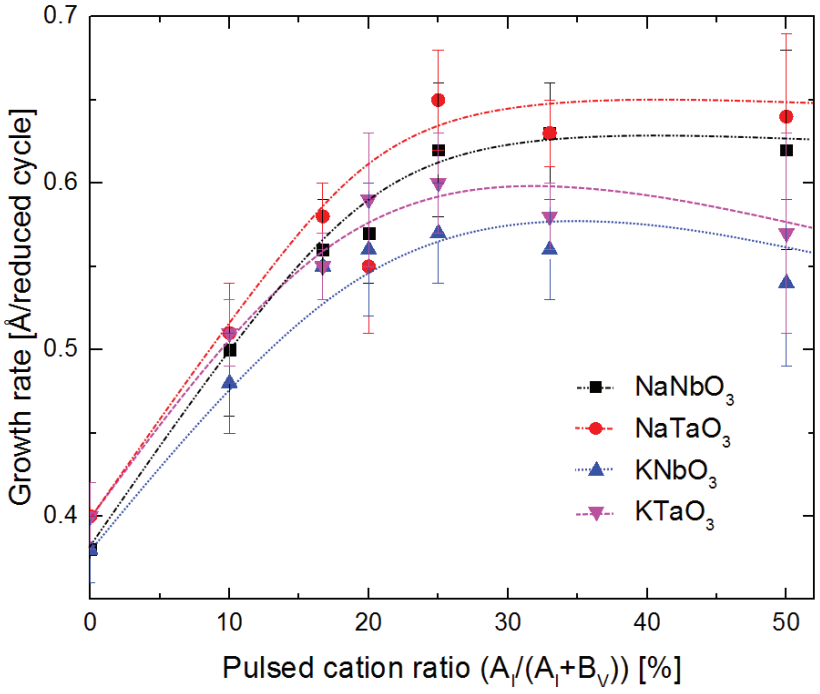

Figure 27: Growth rate as a function of the pulsed cation ratio. All films deposited at 250 °C.

The growth rates of the potassium-containing films were slightly higher than for sodium in the low alkali metal content regime, but increased more slowly and in the end, the growth rate goes down with increasing pulsed ratio of potassium. This is seen both for the niobate and tantalate system. The

composition as a function of the pulsed ratio between the metal precursors were studied and also found to be very similar for the four systems (Figure 28).

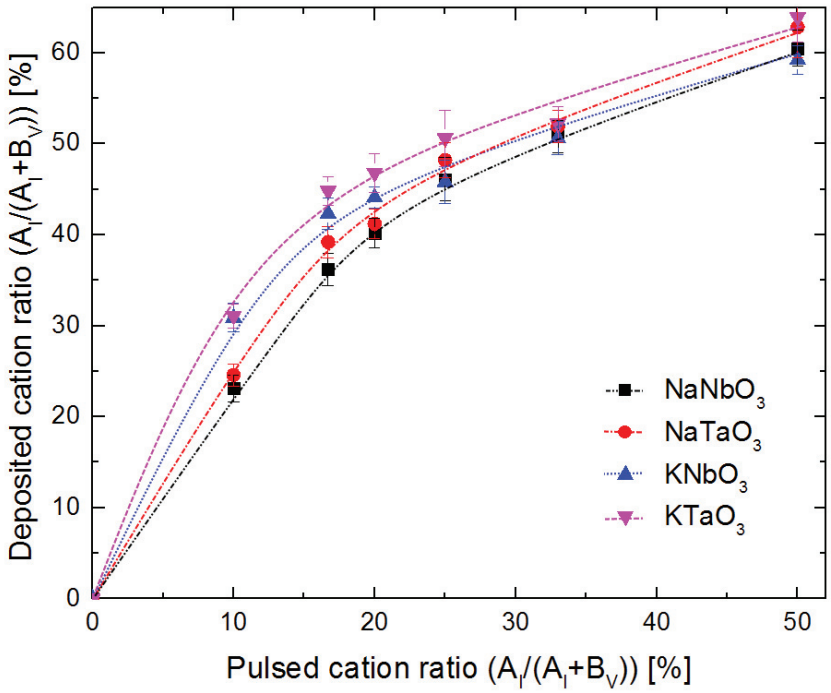

Figure 28: Cation ratio in the $NaNbO_3$, $NaTaO_3$, $KNbO_3$ and $KTaO_3$ thin films as a function of the pulsed cation ratio. All films deposited at 250 °C.

An important feature to note here is the very rapid increase in alkali metal content for low pulsing ratios. For a 1:9 alkali metal to group V metal pulsed ratio, a deposited ratio of between 1:3 and 1:4 was found. This probably means that the small alkali metal does not only saturate the top layer, but migrates into the bulk part of the film to some extent during deposition.

This is very similar to the growth characteristics of $LiNbO_3$. Also note that the 1:1 congruent stoichiometry in the films is found very close to 1:2 pulsed ratio for all systems.

Growth rate for the congruent compositions were found to be 0.63 ± 0.03, 0.62 ± 0.02, 0.56 ± 0.03 and 0.58 ± 0.02 Å/binary cycle for $NaNbO_3$, $NaTaO_3$, $KNbO_3$ and $KTaO_3$, respectively. With the deposition parameters used this corresponds to 100 nm per hour, which should be acceptable for many possible applications of these films. The rate of growth as a function of time could be increased even further if precursor temperature and pulse and purge duration are optimized.

To investigate the temperature stability of the systems, the chamber temperature was varied between 200 and 350 °C for a set of depositions (Figure 29). All systems were found to have stable self-limited growth between 225 and 275 °C, with a possible extension to 200 and 300 °C. At these limits, however, uniformity and composition start to change drastically. A notable difference between the potassium and sodium systems is found in the high T_R region. The growth rate for the sodium systems drop drastically, while it increases for the potassium system. This feature was also observed for growth of sodium- and potassium aluminates. A possible explanation for this can be found in the differences in iconicity for the two precursors. KO^tBu is found to be predominantly ionic, whereas NaO^tBu has a more covalent character. As a result of this it is thought that NaO^tBu will desorb as a molecule at higher temperatures (yielding lower growth rate), while KO^tBu will be more strongly bond and eventually decompose on the surface (yielding higher growth rate). The potassium containing films deposited at high temperatures exhibit severe carbon contamination, believed to be a result of the described decomposition.

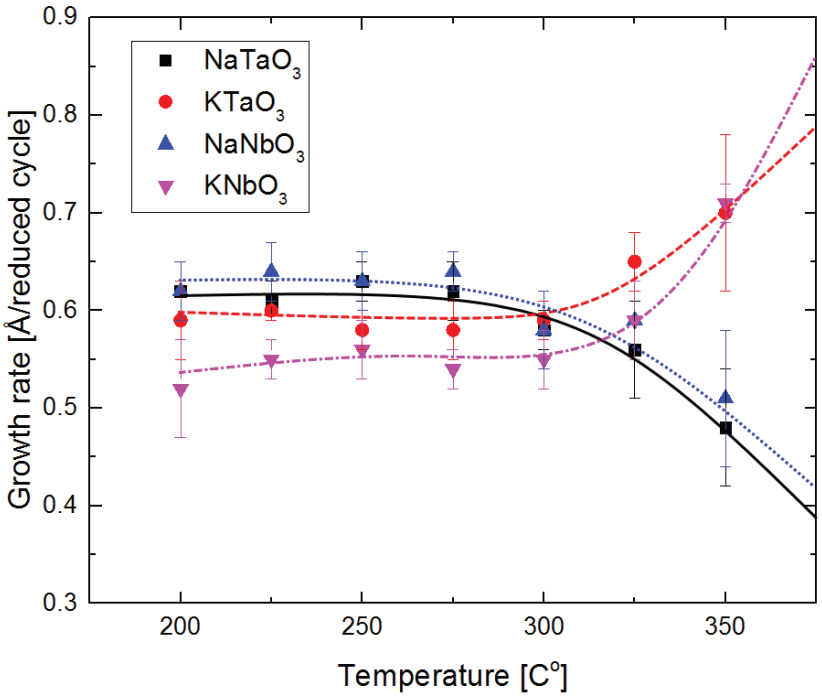

Figure 29: Growth rates for the $NaNbO_3$, $NaTaO_3$, $KNbO_3$ and $KTaO_3$ thin films as a function of reactor temperature. All films were deposited using a 1:3 alkali vs group V metal pulsing ratio.

With growth control of the ternary systems in place, combining them to form quaternary systems was the natural next step. This was carried out without problems, a result of the large similarities between the

ternary systems. Four solid solutions were investigated, and all showed remarkable mixability (Figure 30). This is an expected result, as these solid solutions are found to exist over the whole compositional regime in bulk systems. The ions that are substituted are also of very similar sizes, facilitating the possibility of full mixing.

Only very slight deviations from a linear response were found, most likely due to the slightly faster growth of tantalates *vs.* niobates, and potassium *vs*. sodium compounds. The technologically interesting $K_{0.5}Na_{0.5}NbO_3$ ratio was for example found for a K:Na pulsed ratio of 48:52. As a proof-of-concept for the versatility of this deposition system the quinary $K_{0.5}Na_{0.5}Nb_{0.5}Ta_{0.5}O_3$ was also deposited, with pulsed ratios K:Na = 48:52 and Nb:Ta = 51:49.

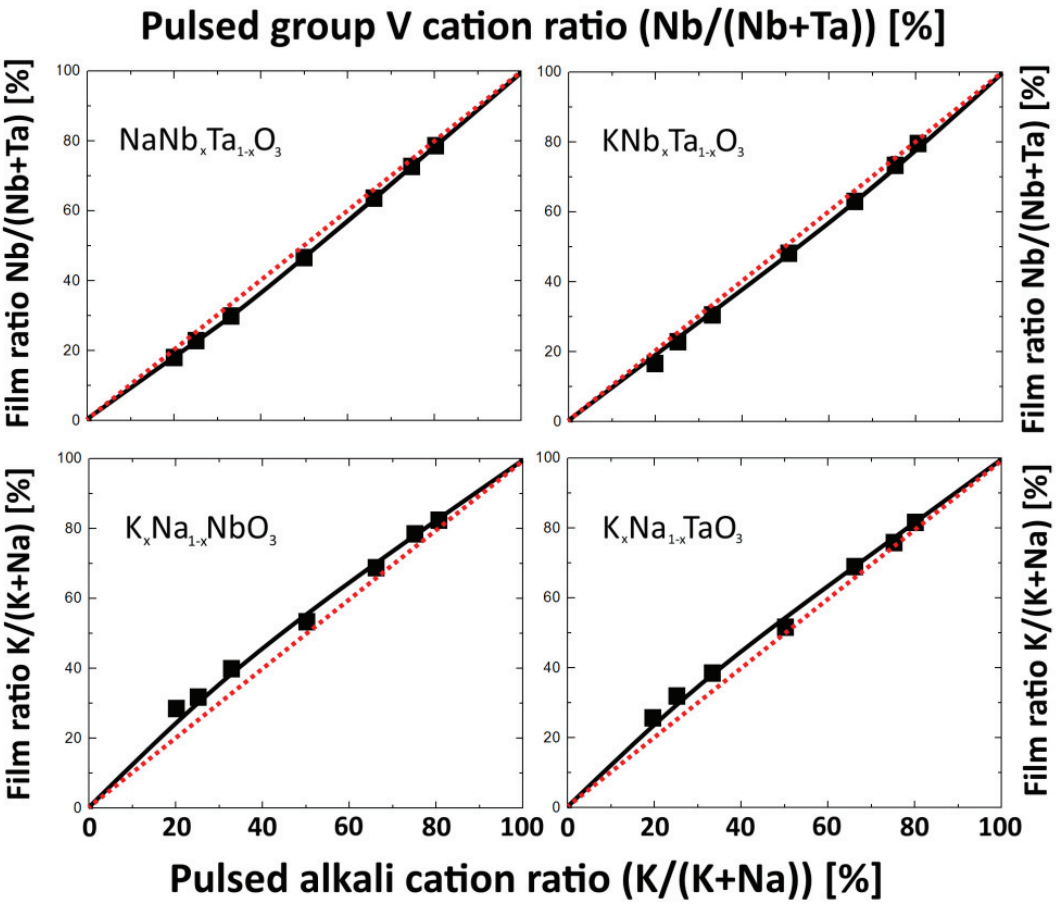

Figure 30: Intermixing on the cation and anion site for the four end member systems to form quaternary compounds. The dotted red line indicates a 1:1 linear intermixing; uncertainties within the size of symbols.

If these solid solutions, especially KNN and KTN, are to be used in technological applications, a coarse mixability is not sufficient. The compositions must be tunable around the morphotropic phase boundaries that facilitate large variation in physical properties. The most interesting boundary for ferroelectric applications is the $K_{0.475}Na_{0.525}NbO_3$ composition, where the piezoresponse has a maximum.[125] To investigate this tunability in the ALD-system, 11 films with very slight differences in pulsed ratio between the alkali metal precursors was deposited (Figure 31). A near linear (slightly banana shaped) correlation is seen, just as for the full range. It is definitely possible to tune the composition around the MPB, but it is difficult to determine if small-scale tuning at a fraction of a percent is possible. A proper investigation of this would have to be carried out with characterisation equipment with lower margin of error.

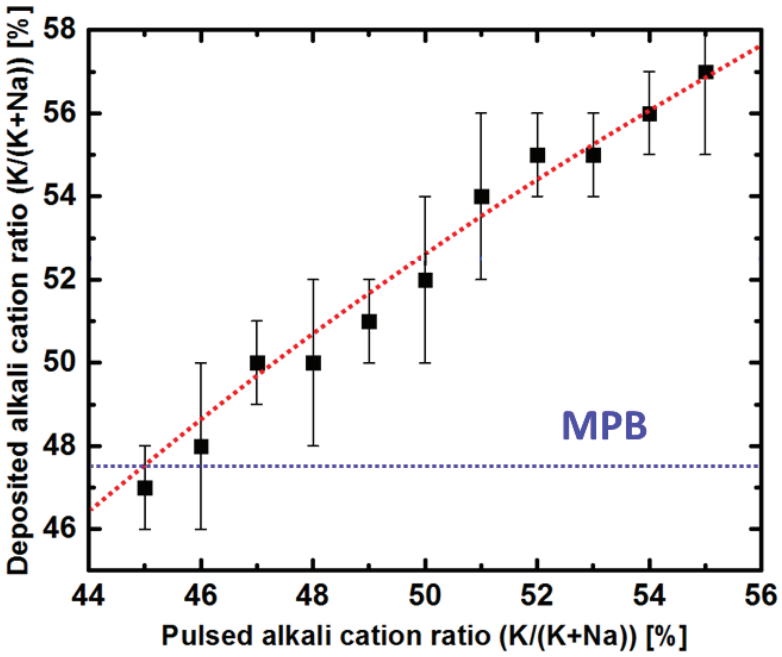

Figure 31: K:Na compositional ratio as a function of pulsed alkali cation ratio close to the 1:1 composition, including compositions near the morphotropic phase boundary (dotted blue).

The important question to ask now is: Is the compositional control in this ALD system good *enough*? There is more than one possible answer to this question, as requirements will vary with application. However, looking at variations in parameters such as the piezoelectric coefficient, d_{33}; the physical properties do not vary much with compositional changes of a few percent, (Figure 32).[126] This means that at least for some applications, the achieved control in the ALD system should be more than sufficient.

Just as important as the fine tuning is the reproducibility of the system. This is a challenge for many complex oxide ALD systems, especially those involving alkali metals. A common issue is that the first few depositions deviate from the general case. This is also seen for the alkali niobates and tantalates, where the two first depositions have an off stoichiometry of 2-5 %. The subsequent depositions vary less, but if these films are to be used in applications, the variation must not be detrimental to physical properties.

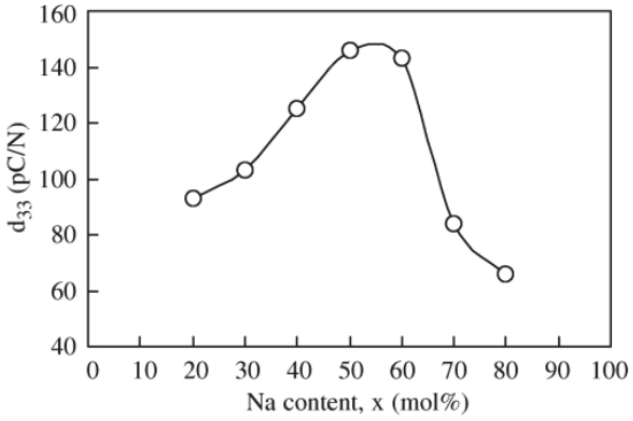

Figure 32: Piezoelectric coefficient as a function of sodium content in $KNbO_3$:$NaNbO_3$ solid solution. Reused with permission from John Wiley and Sons.[126]

To investigate the reproducibility, 10 depositions with exactly the same parameters were performed (Figure 33). All these films were deposited using a 1:1 pulsing ratio between potassium- and sodium *t*-butoxide. The first two data points are not shown in the figure, as these are off by ~5 and ~3 % respectively. Films 3-10 vary only slightly, and are all inside an average compositional distribution of less than 1 %. The x-axis distribution in the red dotted box in Figure 33 shows what would be the result of changing 1 out of 100 Na/K-pulses in the experiment, showing that the reproducibility is really on the limit of what is achievable by ALD. In conclusion, it is clear that not only can the composition be tuned, but the reproducibility is also very high.

Depositing films with the right composition is crucial, but just as important is the structural properties. As previously mentioned, all films are x-ray amorphous as deposited. Crystallization of the films was studied *in situ*. The films were placed on a goniometer under a carbon dome that allows for variation of the temperature from ambient to 1100 °C, while continuously performing diffraction experiments. All the different systems exhibit very similar characteristics when heated, and this is exemplified by the $NaNbO_3$-system in Figure 34.

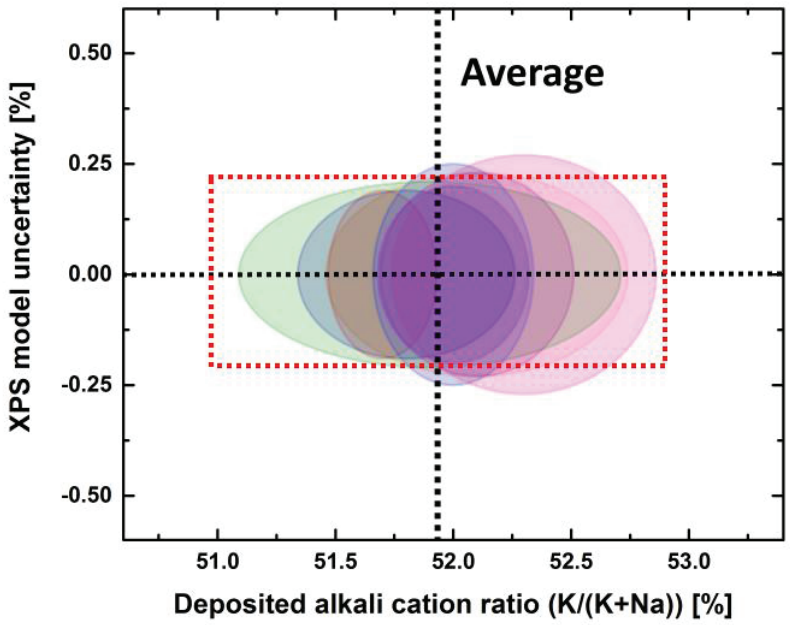

Figure 33: Uncertainty in the composition of 8 films deposited with exactly the same parameters. The x-axis shows compositional distribution in the flow direction on 2 cm long substrates as measured by XPS. The y-axis shows the uncertainty in the composition as a result of the XPS fitting model that is utilized. The red box shows how changing a single pulse out of 100 will theoretically affect the composition.

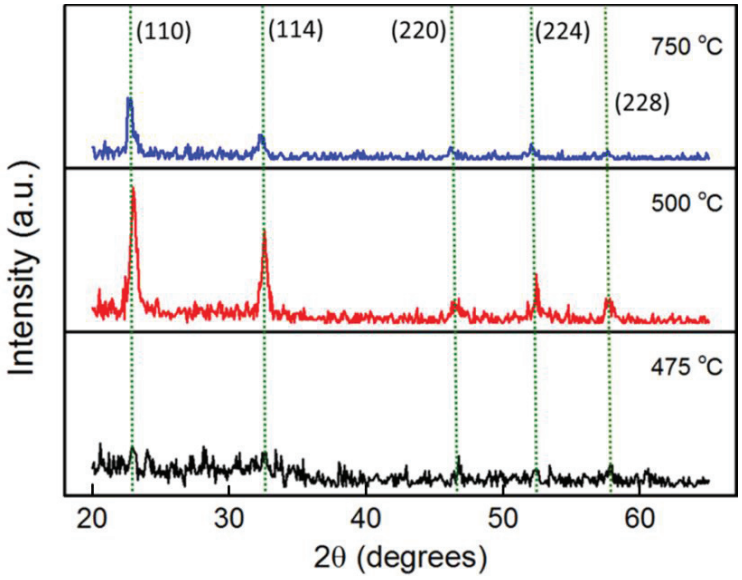

Figure 34: Crystallization upon heating for the $NaNbO_3$ on Si (100) thin film system. The films are amorphous as deposited, and start to crystallize at 500 °C. Heating to more than 700 °C is detrimental.

At temperatures below 500 °C the films remain amorphous, but at 500 °C they rapidly snap into a perovskite-like structure without any apparent ordering (on Si(100)-substrates). This structure is kept up to about 750 °C, where the intensity of the reflection rapidly drops. The composition of the films after heat treatment is unchanged for films that have been kept under 700 °C, but for higher temperatures the alkali metal content decreases. Thin films heated to more than 750 °C exhibit detrimental loss of alkali metal. This loss is attributed to vaporization of alkali metal oxide, which is found to be common in thin films of alkali metal complex oxides. This leads to an irreversible structural change that is accompanied by total loss of functional properties. In conclusion, it is important to limit the temperature for the post-deposition annealing step to avoid loss of alkali metal.

Selected $NaNbO_3$ films were also deposited on single crystal substrates of $LaAlO_3$ and $SrTiO_3$ to facilitate a preferred orientation in the crystalline films. As for $LiNbO_3$, $LaAlO_3$-substrates give a preferred epitaxial relationship, with a strong (110)-ordering of the films on $LaAlO_3$ (012)-substrates (Figure 35). Asymmetric reflections were studied to confirm in-plane orientation, the (11.12) $NaNbO_3$-reflection is shown in Figure 36. The in-plane broadening is quite significant, indicating that in-plane orientation is not as stringent as the out-of-plane orientation. This broadening can also be a result of the relatively small crystallite size. It was, however, found that a $NaNbO_3|NaNbO_3[110]||LaAlO_3(012)|LaAlO_3[012]$ epitaxial relationship is present. The three other corner-systems showed similar ordering of the perovskite units on $LaAlO_3$-substrates.

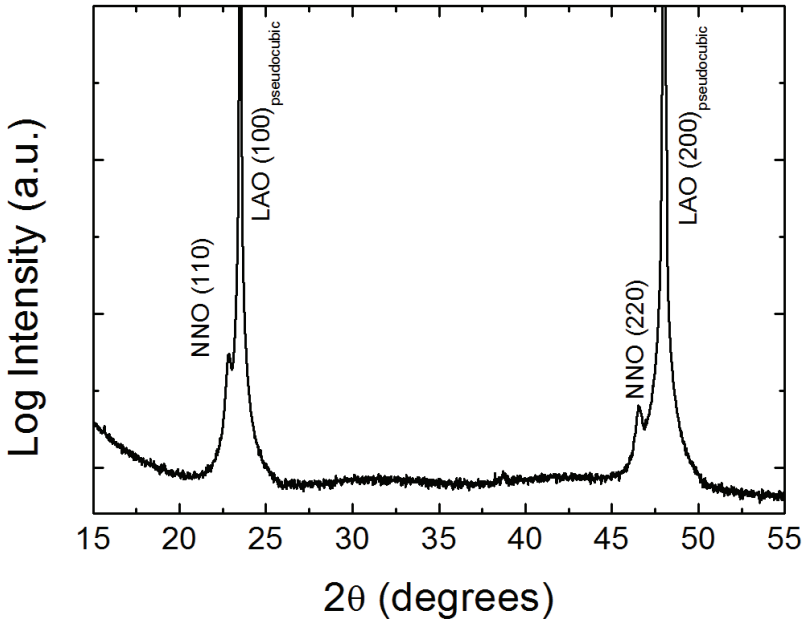

Figure 35: Symmetrical θ-2θ XRD showing the out-of-plane peaks for the thin film and the substrate. LAO-indices are given for a pseudocubic cell.

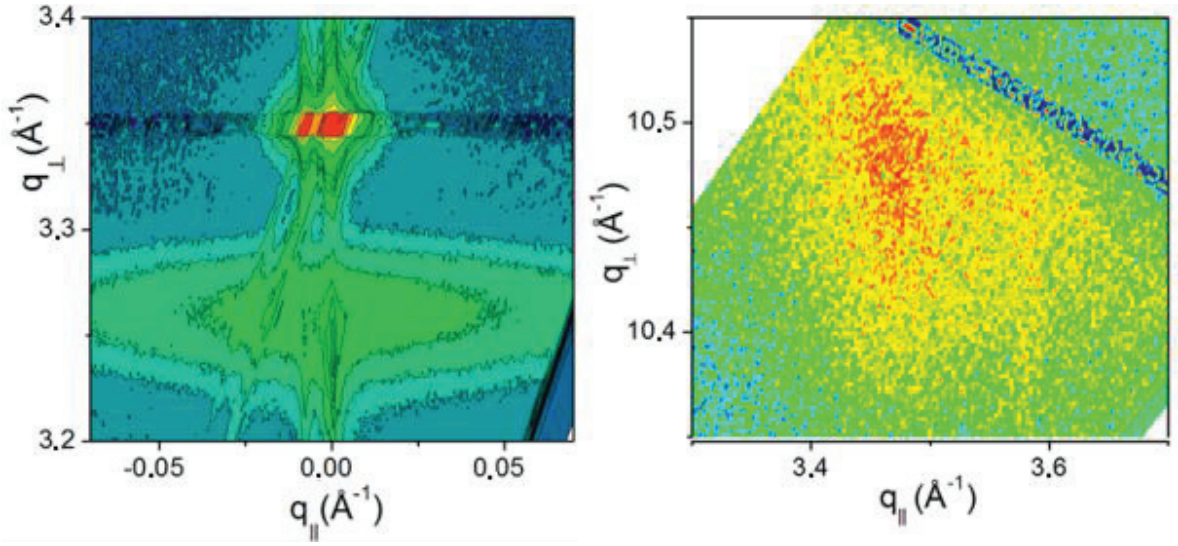

Figure 36, left: Reciprocal space map of the $NaNbO_3$ (110) reflection below the (100) reflection of $LaAlO_3$. Note the split $LaAlO_3$ reflection due to annealing. Right: Reciprocal space map of the $NaNbO_3$ (11.12) reflection.

To study the piezoelectric activity of the films, a film with 1:1 K:Na-ratio was deposited on platinum coated silicon and heat treated at 500 °C for 10 minutes. This film was subsequently tested for piezoresponse using PFM. PFM mapping clearly shows piezoactive domains with complex shape (Figure 37), with some inclusions of small inactive domains that are believed to be Nb_2O_5.

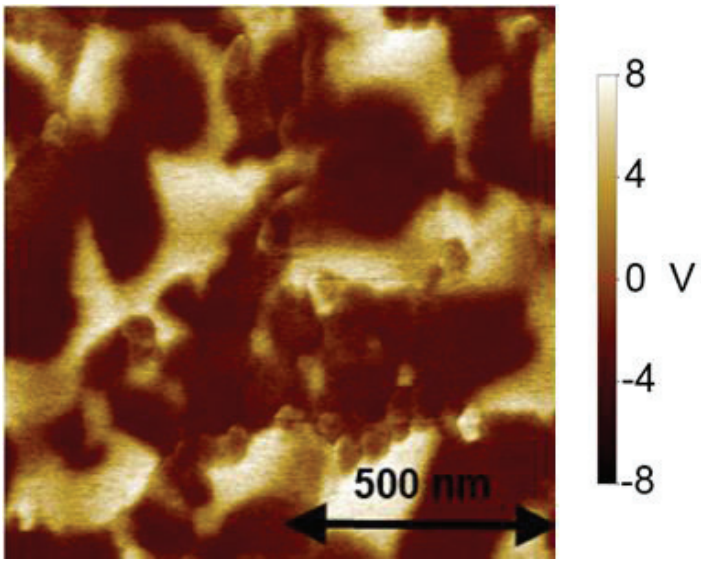

Figure 37: PFM map showing piezoresponse in complex domains in a $K_{0.5}Na_{0.5}NbO_3$ thin film sample on Pt-Si.

The response in the active areas show domains with parallel response. Electric characterization was performed to measure any hysteresis, but this did not bear fruits. This can most probably be attributed to domain wall pinning, which is probably very strong in a system with incommensurate domain borders such as these. There is no doubt piezoelectric response in these films, but the current data is inconclusive whether the films are, indeed, ferroelectric.

The next natural step here would be to deposit a narrow range of compositions around the MPB's and try to measure changes in electric activity. This does, however, require a feasible way of measuring subtle changes in the electric characteristics. It also requires control of domain shape and interface morphology towards the Pt(111)-surface. This would be a very comprehensive study that would form an interesting research project on its own, and has not been included in this work.

In conclusion, this work provides proof that epitaxial thin films of complex oxides containing alkali metals, with strong compositional control can be deposited by ALD. Proof-of-concept of deposition of the important $K_xNa_{1-x}NbO_3$ and $KTa_xNb_{1-x}O_3$ is provided, as well as deposition of the congruent corner-systems.

6. Conclusion and Future Outlook

One of the "rules" of modern science is that a research project often leads to more questions than answers. This is true for the work leading to this thesis as well, and in this final text I will try to contemplate on what has been achieved, and where to go from here.

The deposition of $LiNbO_3$ is the closest to a finalized work we have come in this work. Uniform films with a high degree of compositional, morphological and orientational control have been achieved, and the electric properties match those of previous reports on films deposited by other techniques. $LiNbO_3$ thin films are already in use in a variety of applications, most importantly in devices utilizing surface acoustic waves. One of the challenges with the traditional techniques has been to uniformly deposit $LiNbO_3$ on patterned substrates with high aspect ratio. This is an intrinsic advantage of the ALD technique (beautifully shown for example in growth of $Ge_2Sb_2Te_5$ by Pore *et al.* [127]), and with this report of a $LiNbO_3$ ALD route, this challenge can been overcome.

There is still a way to go, however, before ALD $LiNbO_3$ can find a place in mass production. The domains of the films reported here have a complex shape, and to obtain a uniform electric response the films must be *poled*. This process involves heating the material above the Curie temperature and cooling it down under perturbation of a strong electric field, effectively achieving uniform alignment of the polar domains. This has not been attempted in the current project, and is one of the issues that must be addressed. In addition, $LiNbO_3$ thin films should ideally be deposited on more relevant substrates. These should be conductive substrates still facilitating epitaxial and oriented growth. A possible candidate is platinum (111), which is highly conductive and has a close lattice match (approximately 3.5 % mismatch). Furthermore, the films must be implemented on a *working device*. Industry will not be interested in using a relatively slow and expensive technique before a significant gain in functionality is achieved on a working prototype. Should this be successful, history has shown that mass-production of thin films is completely feasible, in particular due to the possibility of depositing on a large amount of devices simultaneously. Implementation of ALD HfO_2 on Intel's smallest transistor technology is one of the success stories showing that this is possible.

Deposition of $LiNbO_3$ by ALD has also lead to more indirect progress in the world of ALD and thin films in general. It is the first report of deposition of an epitaxial complex oxide containing an alkali metal. This paved the way for the continuation of the work leading to this thesis, but it also showed that ALD can be used to obtain conformal coatings of materials that have been previously unexplored. Another interesting lithium complex oxide, $LiTaO_3$, was for example reported shortly after publication of the $LiNbO_3$ process.

Doping of $LiNbO_3$ should also be straightforward. This opens up the possibility to deposit films of technologically interesting electrooptical variants such as Fe:$LiNbO_3$ and (Ce,Cu):$LiNbO_3$ which are highly anticipated for use in non-volatile holographic devices.[128, 129] Lithium complex oxides by ALD are also finding their way into future high performance batteries.[130]

The success of $LiNbO_3$ deposition had us venture into complex oxides with other alkali metals. The reported route for deposition of sodium and potassium containing materials have no direct implications other than expanding the possibilities of ALD, but was a directed step towards deposition of anticipated functional complex oxides. A very important feature is the very low carbon contamination, which is often a challenge in chemical deposition routes.

There is still work needed to better understand the mechanisms involved in deposition of sodium and potassium by ALD. The monovalency of the precursors does not hinder ALD growth, and exploring the basic chemistry and kinetics behind this is a pressing issue. It would be interesting to study the mechanism by *in situ* characterization, for example by using a quartz crystal microbalance, mass spectrometry or optical techniques such as FT-IR or *quasi in-situ* using reflection high energy electron diffraction. In combination with theoretical calculations and modelling, one might come closer to understanding the driving force behind the self-limiting growth.

Sodium and potassium deposition is also still limited to *one* type of precursor, which might raise a compatibility issue when combined with other metals than what is done in this project. Work should be continued to investigate other precursors, as this will increase the amount of system to which sodium and potassium can be introduced.

For this project, however, fundamental understanding of the deposition mechanism was not necessary to continue with obtaining functional complex oxides. Although the mechanism is still somewhat of a black-box, it is obvious that we have provided a route for implementation of sodium and potassium in ALD thin films.

The ultimate goal of this work was to show that thin films of functional complex oxide solid solutions such as $K_xNa_{1-x}NbO_3$ and $KTa_xNb_{1-x}O_3$ can be achieved by ALD, and that they exhibit functionality that can be used to replace environmentally hazardous materials. Combining the work on with $LiNbO_3$-deposition and Na/K-precursors paved the way for this, and as a first attempt the four corner-systems $NaNbO_3$, $NaTaO_3$, $KNbO_3$ and $KTaO_3$ was successfully deposited. While this was primarily a step towards obtaining the important mixed phases, it also has some intrinsic value.

All these four systems are technologically interesting, either in their congruent composition or doped with various metals to facilitate functional electrical, optical or chemical properties. This is furthermore the first complex oxides containing sodium or potassium that have been reported by ALD, and it goes to show that epitaxial films of alkali complex oxide compounds can be achieved. I can see many ways forward that would possibly lead to interesting materials systems. Lanthanide doped $NaNbO_3$ on textured surfaces for high output water-splitting is one, electrooptical devices based on $KNbO_3$ or doped versions of it is another.[47, 61, 63]

In addition to the direct applications, a new field of functional engineering on interfaces has emerged over the last 10 years. The I-V-perovskites are theoretically predicted to facilitate exotic effects in interfaces with III-III- and II-IV-perovskites such as $LaAlO_3$ or $SrTiO_3$. In this thesis, we have provided proof that epitaxial integration of I-V-perovskites is definitely possible by ALD. With the thickness and conformality control the technique offers, ALD should find its place among the go-to deposition techniques when these systems are to be studied. The relatively low deposition temperature is also an advantage, avoiding alkali metal loss and cracking of substrates.

$K_xNa_{1-x}NbO_3$ was deposited as a proof-of-concept that quaternary complex oxides with functional properties can be obtained by ALD. In contrast to $LiNbO_3$ there is still a long way to go before this can be considered an ultimate success. It is obvious that the composition can be fine-tuned, and that the reproducibility of the system is high. Piezoelectric response has been shown by PFM mapping, but more work needs to be done to quantitatively determine the quality of the functionality. Ferroelectricity has not been confirmed, and there is doubt towards what quenches this effect. Domain wall pinning has been mentioned, but it could just as well be an effect of the orientation or the way the electric response is probed. Tuning the composition around the morphotropic phase boundary and examining the variation of electric properties as a function of the composition is one very interesting way forward. When all this is sorted out, the system must, just as for $LiNbO_3$, be tested in a device to see if its use is viable in mass-production.

Finally, proof-of-concept of deposition of the technologically important electrooptical $KTa_xNb_{1-x}O_3$ is presented. The non-linear electrooptical coefficient of KTN is very high close to the Curie temperature of the ferroelectric to paraelectric phase transition (~300 K). The T_c can furthermore be tuned by varying the Ta:Nb-ratio, thus also tuning the temperature for the high electrooptical activity. This makes it a viable material for use in spatial light modulators or second-harmonic generation devices. Electrooptics were not in the core focus of this work, and KTN was not explored further in terms of electrooptical properties.

However, a facile route for depositing epitaxial thin films of KTN is highly anticipated, as bulk crystals are inherently difficult to synthesize, and come at a very high cost.

It has nonetheless become clear that ALD definitely can be used to obtain the wanted phases, which was really what we set out to prove (Figure 38).

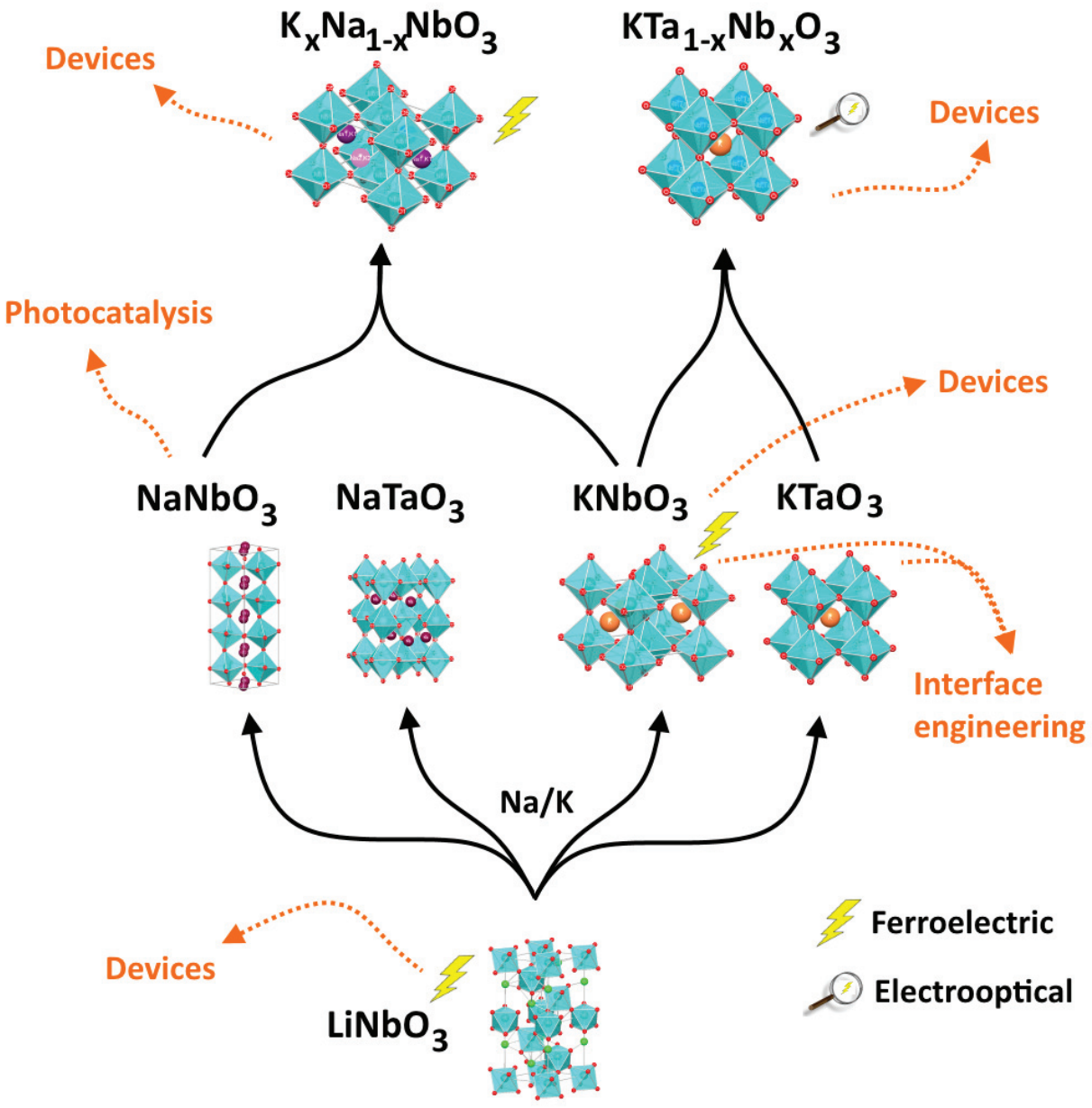

Figure 38: A cartoon showing what has been achieved in this work, from $LiNbO_3$ all the way to the important $K_xNa_{1-x}NbO_3$ and $KTa_{1-x}Nb_xO_3$. Orange arrows point to future research and engineering.

References

[1] H.D. Megaw, *Crystal Structure of Barium Titanate, Nature*, **1945**, *155*, 484-485.

[2] J. Wang, J.B. Neaton, H. Zheng, V. Nagarajan, S.B. Ogale, B. Liu, D. Viehland, V. Vaithyanathan, D.G. Schlom, U.V. Waghmare, N.A. Spaldin, K.M. Rabe, M. Wuttig, and R. Ramesh, *Epitaxial $BiFeO_3$ Multiferroic Thin Film Heterostructures, Science*, **2003**, *299*, 5613, 1719-1722.

[3] D. Lebeugle, D. Colson, A. Forget, and M. Viret, *Very large spontaneous electric polarization in $BiFeO_3$ single crystals at room temperature and its evolution under cycling fields, Appl. Phys. Lett.*, **2007**, *91*, 2, 022907.

[4] J.M.D. Coey, M. Viret, and S. von Molnár, *Mixed-valence manganites, Adv. Phys.*, **1999**, *48*, 2, 167-293.

[5] Y. Tokura and Y. Tomioka, *Colossal magnetoresistive manganites, J. Magn. Magn. Mater.*, **1999**, *200*, 1-3, 1-23.

[6] J.H. Haeni, P. Irvin, W. Chang, R. Uecker, P. Reiche, Y.L. Li, S. Choudhury, W. Tian, M.E. Hawley, B. Craigo, A.K. Tagantsev, X.Q. Pan, S.K. Streiffer, L.Q. Chen, S.W. Kirchoefer, J. Levy, and D.G. Schlom, *Room-temperature ferroelectricity in strained $SrTiO_3$, Nature*, **2004**, *430*, 7001, 758-761.

[7] W. Chen, X. Yao, and X. Wei, *Tunability and ferroelectric relaxor properties of bismuth strontium titanate ceramics, Appl. Phys. Lett.*, **2007**, *90*, 18, 182902.

[8] A. Ohtomo and H.Y. Hwang, *A high-mobility electron gas at the $LaAlO_3/SrTiO_3$ heterointerface, Nature*, **2004**, *427*, 6973, 423-426.

[9] S. Gariglio, N. Reyren, A.D. Caviglia, and J.M. Triscone, *Superconductivity at the $LaAlO_3/SrTiO_3$ interface, J. Phys-Condens. Matt.*, **2009**, *21*, 16, 164213.

[10] H.A. Jahn and E. Teller, *Stability of Polyatomic Molecules in Degenerate Electronic States. I. Orbital Degeneracy, P Roy. Soc. Lond. A Mat.*, **1937**, *161*, 905, 220-235.

[11] A. Glazer, *The classification of tilted octahedra in perovskites, Acta Crystallogr. B*, **1972**, *28*, 11, 3384-3392.

[12] V.M. Goldschmidt, *Die Gesetze der Krystallochemie, Naturwissenschaften*, **1926**, *14*, 21, 477-485.

[13] D.M. Helen, *Crystal structure of double oxides of the perovskite type, P. Phys. Soc.*, **1946**, *58*, 2, 133.

[14] G. Shirane, H. Danner, A. Pavlovic, and R. Pepinsky, *Phase Transitions in Ferroelectric $KNbO_3$, Phys. Rev.*, **1954**, *93*, 4, 672-673.

[15] J.B. Goodenough, *An interpretation of the magnetic properties of the perovskite-type mixed crystals $La_{1-x}Sr_xCoO_{3-\lambda}$, J. Phys. Chem. Solids*, **1958**, *6*, 2, 287-297.

[16] J. Kanamori, *Superexchange interaction and symmetry properties of electron orbitals, J. Phys. Chem. Solids*, **1959**, *10*, 2, 87-98.

[17] J. Kanamori, *Crystal Distortion in Magnetic Compounds, J. Appl. Phys.*, **1960**, *31*, 5, S14-S23.

[18] J.B. Goodenough, *Theory of the Role of Covalence in the Perovskite-Type Manganites [La,M(II)]MnO_3, Physical Review*, **1955**, *100*, 2, 564-573.

[19] M. Kim and B.I. Min, *Nature of itinerant ferromagnetism of $SrRuO_3$: A DFT+DMFT study, Phys. Rev. B*, **2015**, *91*, 20, 205116.

[20] H.H. Sønsteby, O. Nilsen, and H. Fjellvåg, *Functional Perosvskites by Atomic Layer Deposition - an Overview, Adv. Mater. Interfac.*, **2016**, *DOI: 10.1002/admi.201600903*,

[21] H.F. Kay and P. Vousden, *XCV. Symmetry changes in barium titanate at low temperatures and their relation to its ferroelectric properties, Lond. Edinb. Dubl. Phil. Mag.*, **1949**, *40*, 309, 1019-1040.

[22] G. Shirane and S. Hoshino, *On the Phase Transition in Lead Titanate, J. Phys. Soc. Jpn.*, **1951**, *6*, 4, 265-270.

[23] G. Shirane and K. Suzuki, *Crystal Structure of $Pb(Zr\text{-}Ti)O_3$, J. Phys. Soc. Jpn.*, **1952**, *7*, 3, 333-333.

[24] B. Jaffe, R.S. Roth, and S. Marzullo, *Piezoelectric Properties of Lead Zirconate‐Lead Titanate Solid‐Solution Ceramics, J. Appl. Phys.*, **1954**, *25*, 6, 809-810.

[25] H. Jaffe and D.A. Berlincourt, *Piezoelectric transducer materials, P. IEEE*, **1965**, *53*, 10, 1372-1386.

[26] V.A. Isupov, *Phases in the PZT Ceramics, Ferroelectrics*, **2002**, *266*, 1, 427-438.

[27] I. Inbar and R.E. Cohen, *Origin of ferroelectricity in $LiNbO_3$ and $LiTaO_3$, Ferroelectrics*, **1997**, *194*, 1, 83-95.

[28] I. Inbar and R.E. Cohen, *Origin of ferroelectricity in $LiTaO_3$ and $LiNbO_3$; LAPW total energy calculations, Ferroelectrics*, **1995**, *164*, 1, 45-55.

[29] X. Wang, J. Wu, D. Xiao, J. Zhu, X. Cheng, T. Zheng, B. Zhang, X. Lou, and X. Wang, *Giant Piezoelectricity in Potassium–Sodium Niobate Lead-Free Ceramics, J. Am. Chem. Soc.*, **2014**, *136*, 7, 2905-2910.

[30] N. Setter, D. Damjanovic, L. Eng, G. Fox, S. Gevorgian, S. Hong, A. Kingon, H. Kohlstedt, N.Y. Park, G.B. Stephenson, I. Stolitchnov, A.K. Taganstev, D.V. Taylor, T. Yamada, and S. Streiffer, *Ferroelectric thin films: Review of materials, properties, and applications, J. Appl. Phys.*, **2006**, *100*, 5, 051606.

[31] B.T. Matthias and J.P. Remeika, *Ferroelectricity in the Ilmenite Structure, Phys. Rev.*, **1949**, *76*, 12, 1886-1887.

[32] R.S. Weis and T.K. Gaylord, *Lithium niobate: Summary of physical properties and crystal structure, Appl. Phys. A*, **1985**, *37*, 4, 191-203.

[33] K. Nassau, H.J. Levinstein, and G.M. Loiacono, *Ferroelectric lithium niobate. 1. Growth, domain structure, dislocations and etching, J. Phys. Chem. Solids*, **1966**, *27*, 6–7, 983-988.

[34] X. Chen, M.A. Mohammad, J. Conway, B. Liu, Y. Yang, and T.-L. Ren, *High performance lithium niobate surface acoustic wave transducers in the 4–12 GHz super high frequency range, J. Vac. Sci. Technol. B*, **2015**, *33*, 6, 06F401.

[35] A. Riefer, S. Sanna, A.V. Gavrilenko, and W.G. Schmidt, *Linear and nonlinear optical response of $LiNbO_3$ calculated from first principles, IEEE T. Ultrason. Ferr.*, **2012**, *59*, 9, 1929-1933.

[36] T.A. Rost, H. Lin, and T.A. Rabson, *Ferroelectric switching of a field‐effect transistor with a lithium niobate gate insulator, Appl. Phys. Lett.*, **1991**, *59*, 27, 3654-3656.

[37] H. Guenther, R. Macfarlane, Y. Furukawa, K. Kitamura, and R. Neurgaonkar, *Two-color holography in reduced near-stoichiometric lithium niobate, Appl. Optics*, **1998**, *37*, 32, 7611-7623.

[38] S. Yoshihiko, K. Kiyoshi, A. Kageyasu, K. Masaki, K. Tomoji, and K. Shichio, *Epitaxial Growth of $LiNbO_3$ Films on Sapphire Substrates by Excimer Laser Ablation Method and Their Surface Acoustic Wave Properties, Jpn. J. Appl. Phys.*, **1993**, *32*, 5B, L745.

[39] S.B. Ogale, R. Nawathey‐Dikshit, S.J. Dikshit, and S.M. Kanetkar, *Pulsed laser deposition of stoichiometric $LiNbO_3$ thin films by using O_2 and Ar gas mixtures as ambients, J. Appl. Phys.*, **1992**, *71*, 11, 5718-5720.

[40] R.A. Betts and C.W. Pitt, *Growth of thin-film lithium niobate by molecular beam epitaxy, Electron. Lett.*, **1985**, *21*, 21, 960-962.

[41] J.A. Agostinelli, G.H. Braunstein, and T.N. Blanton, *Epitaxial $LiTaO_3$ thin films by pulsed laser deposition, Appl. Phys. Lett.*, **1993**, *63*, 2, 123-125.

[42] Z. Sitar, F. Gitmans, W. Liu, and P. Günter. *Homo and Heteroepitaxial Growth of $LiTaO_3$ and $LiNbO_3$ by MBE*. in *MRS Proceedings*. 1995. Cambridge Univ Press.

[43] M. Kadota and H. Tochishita, *Characteristic of $LiTaO_3$ Film Growth by Chemical Vapor Deposition, IEEJ Trans. Comm.*, **2011**, *131*, 1188-1189.

[44] S. Youssef, R. Al Asmar, J. Podlecki, F. Pascal Delannoy, Y. Zaatar, and A. Foucaran, *Characterization of $LiTaO_3$ thin films fabricated by sol–gel technique, Microelctr. J.*, **2007**, *38*, 1, 63-66.

[45] H.D. Megaw, *The seven phases of sodium niobate, Ferroelectrics*, **1974**, *7*, 1, 87-89.

[46] M. Tyunina, A. Dejneka, D. Rytz, I. Gregora, F. Borodavka, M. Vondracek, and J. Honolka, *Ferroelectricity in antiferroelectric $NaNbO_3$ crystal, J. Phys.-Condens. Mat.*, **2014**, *26*, 12, 125901.

[47] J. Sellmann, J. Schwarzkopf, A. Kwasniewski, M. Schmidbauer, D. Braun, and A. Duk, *Strained ferroelectric $NaNbO_3$ thin films: Impact of pulsed laser deposition growth conditions on structural properties, Thin Solid Films*, **2014**, *570A*, 107-113.

[48] M.D. Aguas and I.P. Parkin, *Combined combustion sol-gel synthesis of $LiNbO_3$, $LiTaO_3$, $NaNbO_3$ and $NaTaO_3$, J. Mater. Sci. Lett.*, **2001**, *20*, 1, 57-58.

[49] V. Lingwal, A.S. Kandari, and N.S. Panwar, *Optical properties of sodium niobate thin films, Nanosys. Phys. Chem. Math.*, **2016**, *7*, 4, 583-591.

[50] S.B. Anooz, P. Petrik, M. Schmidbauer, T. Remmele, and J. Schwarzkopf, *Refractive index and interband transitions in strain modified $NaNbO_3$ thin films grown by MOCVD, J. Phys. D*, **2015**, *48*, 38, 385303.

[51] G. Li, T. Kako, D. Wang, Z. Zou, and J. Ye, *Synthesis and enhanced photocatalytic activity of $NaNbO_3$ prepared by hydrothermal and polymerized complex methods, J. Phys. Chem. Solids*, **2008**, *69*, 10, 2487-2491.

[52] J. Schwarzkopf, D. Braun, M. Schmidbauer, A. Duk, and R. Wördenweber, *Ferroelectric domain structure of anisotropically strained $NaNbO_3$ epitaxial thin films, J. Appl. Phys.*, **2014**, *115*, 20, 204105.

[53] S. Kamba, V. Goian, V. Bovtun, D. Nuzhnyy, M. Kempa, M. Spreitzer, J. König, and D. Suvorov, *Incipient Ferroelectric Properties of $NaTaO_3$, Ferroelectrics*, **2012**, *426*, 1, 206-214.

[54] H. Kato, K. Asakura, and A. Kudo, *Highly Efficient Water Splitting into H_2 and O_2 over Lanthanum-Doped $NaTaO_3$ Photocatalysts with High Crystallinity and Surface Nanostructure, J. Am. Chem. Soc.*, **2003**, *125*, 10, 3082-3089.

[55] C. Reitz, K. Brezesinski, J. Haetge, J. Perlich, and T. Brezesinski, *Nanocrystalline $NaTaO_3$ thin film materials with ordered 3D mesoporous and nanopillar-like structures through PIB-b-PEO polymer templating: towards high-performance UV-light photocatalysts, RSC Adv.*, **2012**, *2*, 12, 5130-5133.

[56] L. Polak, T.P.N. Veeken, J. Houtkamp, M.J. Slaman, S.M. Kars, J.H. Rector, and R.J. Wijngaarden, *Two-step sputter-hydrothermal synthesis of $NaTaO_3$ thin films, Thin Solid Films*, **2016**, *603*, 413-417.

[57] A.M. Huerta-Flores, J. Chen, A. Ito, L.M. Torres-Martínez, E. Moctezuma, and T. Goto, *High-speed deposition of oriented orthorhombic $NaTaO_3$ films using laser chemical vapor deposition, Mater. Lett.*, **2016**, *184*, 257-260.

[58] F.S. Chen, J.E. Geusic, S.K. Kurtz, J.G. Skinner, and S.H. Wemple, *Light Modulation and Beam Deflection with Potassium Tantalate - Niobate Crystals, J. Appl. Phys.*, **1966**, *37*, 1, 388-398.

[59] F. Tsuguo and U. Yutaka, *Preparation of $KNbO_3$ Single Crystal for Optical Applications, Jpn. J. Appl. Phys.*, **1972**, *11*, 2, 163.

[60] M.V. Romanov, I.E. Korsakov, A.R. Kaul, S.Y. Stefanovich, I.A. Bolshakov, and G. Wahl, *MOCVD of $KNbO_3$ ferroelectric films and their characterization, Chem. Vapor Depos.*, **2004**, *10*, 6, 318-324.

[61] S.S. Thöny, H. Lehmann, and P. Günter, *Sputter deposition of epitaxial waveguiding $KNbO_3$ thin films, Appl. Phys. Lett.*, **1992**, *61*, 4, 373-375.

[62] C. Zaldo, D. Gill, R. Eason, J. Mendiola, and P. Chandler, *Growth of $KNbO_3$ thin films on MgO by pulsed laser deposition, Appl. Phys. Lett.*, **1994**, *65*, 4, 502-504.

[63] T.M. Graettinger, S.H. Rou, M.S. Ameen, O. Auciello, and A.I. Kingon, *Electro‐optic characterization of ion beam sputter‐deposited $KNbO_3$ thin films, Appl. Phys. Lett.*, **1991**, *58*, 18, 1964-1966.

[64] G.K.L. Goh, C.G. Levi, J. Hwan Choi, and F.F. Lange, *Hydrothermal epitaxy of $KNbO_3$ thin films and nanostructures, J. Cryst. Growth*, **2006**, *286*, 2, 457-464.

[65] J. Narkilahti and M. Tyunina, *The structure of strained perovskite $KTaO_3$ thin films prepared by pulsed laser deposition, J. Phys-Condens. Mat.*, **2012**, *24*, 32, 325901.

[66] V. Skoromets, S. Glinšek, V. Bovtun, M. Kempa, J. Petzelt, S. Kamba, B. Malič, M. Kosec, and P. Kužel, *Ferroelectric phase transition in polycrystalline $KTaO_3$ thin film revealed by terahertz spectroscopy, Appl. Phys. Lett.*, **2011**, *99*, 5, 052908.

[67] G.K.L. Goh, C.G. Levi, and F.F. Lange, *Hydrothermal epitaxy of $KTaO_3$ thin films, J. Mater. Res.*, **2002**, *17*, 11, 2852-2858.

[68] L. Egerton and D.M. Dillon, *Piezoelectric and Dielectric Properties of Ceramics in the System Potassium—Sodium Niobate, J. Am. Ceram. Soc.*, **1959**, *42*, 9, 438-442.

[69] S. Kenji, O. Fumihito, O. Akio, M. Tomoyoshi, and K. Isaku, *Piezoelectric Properties of $(K,Na)NbO_3$ Films Deposited by RF Magnetron Sputtering, Appl. Phys. Express*, **2008**, *1*, 1, 011501.

[70] S. Kenji, O. Fumihito, N. Akira, M. Tomoyoshi, and K. Isaku, *Crystalline Structure of Highly Piezoelectric $(K,Na)NbO_3$ Films Deposited by RF Magnetron Sputtering, Jpn. J. Appl. Phys.*, **2008**, *47*, 12R, 8909.

[71] H. Scott and M. Paul, *Pulsed laser deposition of KNN-based ferroelectric thin films on platinised Si substrates, IOP C. Ser. Mater. Sci. Eng.*, **2010**, *8*, 1, 012004.

[72] A. Fernandez Solarte, N. Pellegri, O. de Sanctis, and M.G. Stachiotti, *Simple and Rapid Fabrication of Thin Films by a Chelate Route, J. Ceram.*, **2013**, *2013*, 850751, 1-7.

[73] S. Wiegand, S. Flege, O. Baake, and W. Ensinger, *Effect of different calcination temperatures and post annealing on the properties of 1,3-propanediol based Sol–Gel $(Na_{0.5}K_{0.5})NbO_3$ (NKN) thin films, J. Alloy Compd.*, **2013**, *548*, 38-45.

[74] Q. Yu, J.-F. Li, W. Sun, Z. Zhou, Y. Xu, Z.-K. Xie, F.-P. Lai, and Q.-M. Wang, *Electrical properties of $K_{0.5}Na_{0.5}NbO_3$ thin films grown on $Nb:SrTiO_3$ single-crystalline substrates with different crystallographic orientations, J. Appl. Phys.*, **2013**, *113*, 2, 024101.

[75] S. Yilmaz, R. Gerhard-Multhaupt, W.A. Bonner, D.M. Hwang, A. Inam, J.A. Martinez, T.S. Ravi, T. Sands, B.J. Wilkens, X.D. Wu, and T. Venkatesan, *Electro-optic potassium-tantalate-niobate films prepared by pulsed laser deposition from segmented pellets, J. Mater. Res.*, **1994**, *9*, 5, 1272-1279.

[76] J. Li, Y. Li, Z. Zhou, A. Bhalla, and R. Guo, *Linear electrooptic coefficient r51 of tetragonal potassium lithium tantalate niobate $K_{0.95}Li_{0.05}Ta_{0.40}Nb_{0.60}O_3$ single crystal, Opt. Mater. Express*, **2013**, *3*, 12, 2063-2071.

[77] K. Fujiura and K. Nakamura. *KTN optical waveguide devices with an extremely large electro-optic effect*. in *Proc. SPIE 5623*. 2005.

[78] S. Yilmaz, T. Venkatesan, and R. Gerhard‐Multhaupt, *Pulsed laser deposition of stoichiometric potassium‐tantalate‐niobate films from segmented evaporation targets, App. Phys. Lett.*, **1991**, *58*, 22, 2479-2481.

[79] S.-i. Hirano, T. Yogo, K.-i. Kikuta, T. Morishita, and Y. Ito, *Preparation of Potassium Tantalate Niobate by Sol–Gel Method, J. Am. Ceram. Soc.*, **1992**, *75*, 6, 1701-1704.

[80] H.H. Sønsteby, E. Østreng, H. Fjellvåg, and O. Nilsen, *Deposition and x-ray characterization of epitaxial thin films of $LaAlO_3$, Thin Solid Films*, **2014**, *550*, 90-94.

[81] F. Bi, M. Huang, S. Ryu, H. Lee, C.-W. Bark, C.-B. Eom, P. Irvin, and J. Levy, *Room-temperature electronically-controlled ferromagnetism at the $LaAlO_3/SrTiO_3$ interface, Nat. Commun.*, **2014**, *5*, 5019, 1-7.

[82] B. Kalisky, J.A. Bert, B.B. Klopfer, C. Bell, H.K. Sato, M. Hosoda, Y. Hikita, H.Y. Hwang, and K.A. Moler, *Critical thickness for ferromagnetism in $LaAlO_3/SrTiO_3$ heterostructures, Nat. Commun.*, **2012**, *3*, 922.

[83] M. Sepliarsky, S. Phillpot, D. Wolf, M. Stachiotti, and R. Migoni, *Ferroelectric properties of $KNbO_3/KTaO_3$ superlattices by atomic-level simulation, J. Appl. Phys.*, **2001**, *90*, 9, 4509-4519.

[84] K. Zou, S. Ismail-Beigi, K. Kisslinger, X. Shen, D. Su, F.J. Walker, and C.H. Ahn, *$LaTiO_3/KTaO_3$ interfaces: A new two-dimensional electron gas system, APL Mater.*, **2015**, *3*, 3, 036104.

[85] X. Fan, W. Zheng, X. Chen, and D.J. Singh, *2DEGs at Perovskite Interfaces between $KTaO_3$ or $KNbO_3$ and Stannates, PLoS ONE*, **2014**, *9*, 3, e91423.

[86] Y. Yang, C.-S. Lin, J.-F. Chen, L. Hu, and W.-D. Cheng, *Ferromagnetic-nonmagnetic and metal-insulator phase transitions at the interfaces of $KTaO_3$ and $PbTiO_3$, J. Appl. Phys.*, **2014**, *116*, 15, 153709.

[87] T. Suntola and J. Antson, *Method for producing compound thin films*, 1977: US Patent 4058430A.

[88] R.L. Puurunen, *A Short History of Atomic Layer Deposition: Tuomo Suntola's Atomic Layer Epitaxy, Chem. Vapor Depos.*, **2014**, *20*, 10-11-12, 332-344.

[89] R.L. Puurunen, *Surface chemistry of atomic layer deposition: A case study for the trimethylaluminum/water process, J. Appl. Phys.*, **2005**, *97*, 12, 121301.

[90] S.M. George, *Atomic Layer Deposition: An Overview, Chem. Rev.*, **2010**, *110*, 1, 111-131.

[91] R.W. Johnson, A. Hultqvist, and S.F. Bent, *A brief review of atomic layer deposition: from fundamentals to applications, Mater. Today*, **2014**, *17*, 5, 236-246.

[92] I. Vee, *M.Sc. Thesis: Fluorholdige hybridmaterialer med atomlagsavsetting: Syntese og karakterisering (Translation: Fluorine-containing Hybrid Materials with ALD: Synthesis and Characterization)*, 2012, University of Oslo, Norway.

[93] H.B. Profijt, S.E. Potts, M.C.M. van de Sanden, and W.M.M. Kessels, *Plasma-Assisted Atomic Layer Deposition: Basics, Opportunities, and Challenges, J. Vac. Sci. Technol. A*, **2011**, *29*, 5, 050801.

[94] A. Niskanen, K. Arstila, M. Leskelä, and M. Ritala, *Radical Enhanced Atomic Layer Deposition of Titanium Dioxide, Chem. Vapor Depos.*, **2007**, *13*, 4, 152-157.

[95] J.-C. Kwak, Y.-H. Lee, and B.-H. Choi, *Preparation of tantalum oxide thin films by photo-assisted atomic layer deposition, Appl. Surf. Sci.*, **2004**, *230*, 1–4, 249-253.

[96] H. Seim, H. Molsa, M. Nieminen, H. Fjellvåg, and L. Niinistö, *Deposition of $LaNiO_3$ thin films in an atomic layer epitaxy reactor, J. Mater. Chem.*, **1997**, *7*, 3, 449-454.

[97] O. Nilsen, M. Peussa, H. Fjellvåg, L. Niinistö, and A. Kjekshus, *Thin film deposition of lanthanum manganite perovskite by the ALE process, J. Mater. Chem.*, **1999**, *9*, 8, 1781-1784.

[98] H.H. Sønsteby, E. Østreng, H. Fjellvåg, and O. Nilsen, *Atomic Layer Deposition of $LaPO_4$ and $Ca:LaPO_4$, Chem. Vapor Depos.*, **2014**, *20*, 7-8-9, 269-273.

[99] O. Nilsen, E. Rauwel, H. Fjellvåg, and A. Kjekshus, *Growth of $La_{1-x}CaxMnO_3$ thin films by atomic layer deposition, J. Mater. Chem.*, **2007**, *17*, 15, 1466-1475.

[100] J.W. Elam and S.M. George, *Growth of $ZnO/Al2O_3$ Alloy Films Using Atomic Layer Deposition Techniques, Chem. Mater.*, **2003**, *15*, 4, 1020-1028.

[101] M. Lie, O. Nilsen, H. Fjellvag, and A. Kjekshus, *Growth of $La1-xSrxFeO_3$ thin films by atomic layer deposition, Dalton T.*, **2009**, 3, 481-489.

[102] V. Miikkulainen, M. Leskelä, M. Ritala, and R.L. Puurunen, *Crystallinity of inorganic films grown by atomic layer deposition: Overview and general trends, J. Appl. Phys.*, **2013**, *113*, 2, 021301.

[103] A.R. Akbashev, G. Chen, and J.E. Spanier, *A Facile Route for Producing Single-Crystalline Epitaxial Perovskite Oxide Thin Films, Nano Lett.*, **2014**, *14*, 1, 44-49.

[104] M. Putkonen, T. Aaltonen, M. Alnes, T. Sajavaara, O. Nilsen, and H. Fjellvåg, *Atomic layer deposition of lithium containing thin films, J. Mater. Chem.*, **2009**, *19*, 46, 8767-8771.

[105] O. Nilsen, V. Miikkulainen, K.B. Gandrud, E. Østreng, A. Ruud, and H. Fjellvåg, *Atomic layer deposition of functional films for Li-ion microbatteries, Phys. Status Solidi A*, **2014**, *211*, 2, 357-367.

[106] E. Østreng, *Atomic layer deposition of thin films containing alkali metals*, 2013, Department of Chemistry, University of Oslo: Oslo.

[107] W.C. Röntgen, *Ueber eine neue Art von Strahlen, Annalen der Physik*, **1898**, *300*, 1, 1-11.

[108] D.D. Fong, J.A. Eastman, S.K. Kim, T.T. Fister, M.J. Highland, P.M. Baldo, and P.H. Fuoss, *In situ synchrotron x-ray characterization of ZnO atomic layer deposition, Appl. Phys. Lett.*, **2010**, *97*, 19, 191904.

[109] H.H. Sønsteby, D. Chernyshov, M. Getz, O. Nilsen, and H. Fjellvåg, *On the application of a single-crystal κ-diffractometer and a CCD area detector for studies of thin films, J. Synchrotron Radiat.*, **2013**, *20*, 4, 644-647.

[110] G. Binnig, C.F. Quate, and C. Gerber, *Atomic Force Microscope, Phys. Rev. Lett.*, **1986**, *56*, 9, 930-933.

[111] P. Güthner and K. Dransfeld, *Local poling of ferroelectric polymers by scanning force microscopy, Appl. Phys. Lett.*, **1992**, *61*, 9, 1137-1139.

[112] a. J B Theeten and D.E. Aspnes, *Ellipsometry in Thin Film Analysis, Annu. Rev. Mater. Sci.*, **1981**, *11*, 1, 97-122.

[113] W. Assmann, H. Huber, C. Steinhausen, M. Dobler, H. Glückler, and A. Weidinger, *Elastic recoil detection analysis with heavy ions, Nucl. Instrum. Meth. B*, **1994**, *89*, 1, 131-139.

[114] A.W. Coats and J.P. Redfern, *Thermogravimetric analysis. A review, Analyst*, **1963**, *88*, 1053, 906-924.

[115] P. Grosse, *Analysis of thin solid films and surfaces by infrared spectroscopy, Microchim. Acta*, **1991**, *104*, 1, 309-323.

[116] A.K. Petford-Long and A.N. Chiaramonti, *Transmission Electron Microscopy of Multilayer Thin Films, Ann. Rev. Mater. Res.*, **2008**, *38*, 1, 559-584.

[117] T. Aaltonen, M. Alnes, O. Nilsen, L. Costelle, and H. Fjellvag, *Lanthanum titanate and lithium lanthanum titanate thin films grown by atomic layer deposition, J. Mater. Chem.*, **2010**, *20*, 14, 2877-2881.

[118] V. Miikkulainen, A. Ruud, E. Østreng, O. Nilsen, M. Laitinen, T. Sajavaara, and H. Fjellvåg, *Atomic Layer Deposition of Spinel Lithium Manganese Oxide by Film-Body-Controlled Lithium Incorporation for Thin-Film Lithium-Ion Batteries, J. Phys. Chem. C*, **2014**, *118*, 2, 1258-1268.

[119] J. Liu, M.N. Banis, X. Li, A. Lushington, M. Cai, R. Li, T.-K. Sham, and X. Sun, *Atomic Layer Deposition of Lithium Tantalate Solid-State Electrolytes, J. Phys. Chem. C*, **2013**, *117*, 39, 20260-20267.

[120] V. Miikkulainen, O. Nilsen, H. Li, S.W. King, M. Laitinen, T. Sajavaara, and H. Fjellvåg, *Atomic layer deposited lithium aluminum oxide: (In)dependency of film properties from pulsing sequence, J. Vac. Sci. Technol. A*, **2015**, *33*, 1, 01A101.

[121] K. Kukli, M. Ritala, M. Leskelä, and R. Lappalainen, *Niobium Oxide Thin Films Grown by Atomic Layer Epitaxy, Chem. Vapor Depos.*, **1998**, *4*, 1, 29-34.

[122] J. Hämäläinen, F. Munnik, T. Hatanpää, J. Holopainen, M. Ritala, and M. Leskelä, *Study of amorphous lithium silicate thin films grown by atomic layer deposition, J. Vac. Sci. Technol. A*, **2012**, *30*, 1, 01A106.

[123] V. Gopalan, T.E. Mitchell, Y. Furukawa, and K. Kitamura, *The role of nonstoichiometry in 180° domain switching of $LiNbO_3$ crystals, Appl. Phys. Lett.*, **1998**, *72*, 16, 1981-1983.

[124] K. Kukli, M. Ritala, and M. Leskelä, *Atomic Layer Epitaxy Growth of Tantalum Oxide Thin Films from $Ta(OC_2H_5)_5$ and H_2O J. Electrochem. Soc.*, **1995**, *142*, 5, 1670-1675.

[125] X. Pang, J. Qiu, and K. Zhu, *Morphotropic Phase Boundary of Sodium–Potassium Niobate Lead-Free Piezoelectric Ceramics, J. Amer. Ceram. Soc.*, **2011**, *94*, 3, 796-801.

[126] B.-P. Zhang, J.-F. Li, K. Wang, and H. Zhang, *Compositional Dependence of Piezoelectric Properties in $Na_xK_{1-x}NbO_3$ Lead-Free Ceramics Prepared by Spark Plasma Sintering, J. Am. Ceram. Soc.*, **2006**, *89*, 5, 1605-1609.

[127] V. Pore, T. Hatanpää, M. Ritala, and M. Leskelä, *Atomic Layer Deposition of Metal Tellurides and Selenides Using Alkylsilyl Compounds of Tellurium and Selenium, J. Am. Chem. Soc.*, **2009**, *131*, 3478, 3478-3480.

[128] K. Buse, A. Adibi, and D. Psaltis, *Non-volatile holographic storage in doubly doped lithium niobate crystals, Nature*, **1998**, *393*, 6686, 665-668.

[129] Y. Liu, L. Liu, C. Zhou, and L. Xu, *Nonvolatile photorefractive holograms in $LiNbO_3$:CuCe crystals, Opt. Lett.*, **2000**, *25*, 12, 908-10.

[130] L. Ma, R.B. Nuwayhid, T. Wu, Y. Lei, K. Amine, and J. Lu, *Atomic Layer Deposition for Lithium-Based Batteries, Adv. Mater. Interfac.*, **2016**, *3*, 21, 1600564-1600578.